

QUASI-TRANSIENT CALCULATION OF SURFACE TEMPERATURES ON A REUSABLE  
BOOSTER SYSTEM WITH HIGH ANGLES OF ATTACK

Thesis

Submitted to

The School of Engineering of the  
UNIVERSITY OF DAYTON

In Partial Fulfillment of the Requirements for  
The Degree of  
Master of Science in Aerospace Engineering

By

Seth Henderson Morris

Dayton, OH

December, 2011



Report Documentation Page			Form Approved OMB No. 0704-0188		
Public reporting burden for the collection of information is estimated to average 1 hour per response, including the time for reviewing instructions, searching existing data sources, gathering and maintaining the data needed, and completing and reviewing the collection of information. Send comments regarding this burden estimate or any other aspect of this collection of information, including suggestions for reducing this burden, to Washington Headquarters Services, Directorate for Information Operations and Reports, 1215 Jefferson Davis Highway, Suite 1204, Arlington VA 22202-4302. Respondents should be aware that notwithstanding any other provision of law, no person shall be subject to a penalty for failing to comply with a collection of information if it does not display a currently valid OMB control number.					
1. REPORT DATE <b>DEC 2011</b>		2. REPORT TYPE		3. DATES COVERED <b>00-00-2011 to 00-00-2011</b>	
4. TITLE AND SUBTITLE <b>Quasi-Transient Calculation of Surface Temperatures on a Reusable Booster System with High Angles of Attack</b>			5a. CONTRACT NUMBER		
			5b. GRANT NUMBER		
			5c. PROGRAM ELEMENT NUMBER		
6. AUTHOR(S)			5d. PROJECT NUMBER		
			5e. TASK NUMBER		
			5f. WORK UNIT NUMBER		
7. PERFORMING ORGANIZATION NAME(S) AND ADDRESS(ES) <b>University of Dayton,300 College Park,Dayton,OH,45469</b>			8. PERFORMING ORGANIZATION REPORT NUMBER		
9. SPONSORING/MONITORING AGENCY NAME(S) AND ADDRESS(ES)			10. SPONSOR/MONITOR'S ACRONYM(S)		
			11. SPONSOR/MONITOR'S REPORT NUMBER(S)		
12. DISTRIBUTION/AVAILABILITY STATEMENT <b>Approved for public release; distribution unlimited</b>					
13. SUPPLEMENTARY NOTES					
14. ABSTRACT <b>The calculation of a recovery temperature based heat transfer coefficient proves to be sufficiently independent of wall temperature to use in a three dimensional, transient temperature model of a thermal protection system of a reusable booster concept. After a derivation of recovery temperature from the 1st law of thermodynamics, the weak dependence of the recovery temperature based heat transfer coefficient is investigated by 72 Computational Fluid Dynamics (CFD) models at angles of attack ranging from 0° to 90° over a range of Mach numbers, from Mach 2 to 5, and a variety of thermal boundary conditions at the wall, from isothermal to a conductive wall. Then, the heat transfer coefficient is calculated at many steady state CFD solutions for a reusable booster system concept on a given trajectory and applied to a transient Finite Element Analysis (FEA) model of a thermal protection system. Results are presented graphically.</b>					
15. SUBJECT TERMS					
16. SECURITY CLASSIFICATION OF:			17. LIMITATION OF ABSTRACT <b>Same as Report (SAR)</b>	18. NUMBER OF PAGES <b>110</b>	19a. NAME OF RESPONSIBLE PERSON
a. REPORT <b>unclassified</b>	b. ABSTRACT <b>unclassified</b>	c. THIS PAGE <b>unclassified</b>			

QUASI-TRANSIENT CALCULATION OF SURFACE TEMPERATURES ON A REUSABLE  
BOOSTER SYSTEM WITH HIGH ANGLES OF ATTACK

Name: Morris, Seth Henderson

APPROVED BY:

---

Timothy John Fry, Ph.D.  
Advisory Committee Chairman  
Group Leader  
Experimental and Applied Mechanics Group,  
University of Dayton Research Institute

---

José A. Camberos, Ph.D., P.E.  
Committee Member  
Professor  
Department of Mechanical and Aerospace  
Engineering

---

John Doty, Ph.D.  
Committee Member  
Professor  
Department of Engineering Management  
and Systems

---

John G. Weber, Ph.D.  
Associate Dean  
School of Engineering

---

Tony E. Saliba, Ph.D.  
Dean, School of Engineering  
& Wilke Distinguished Professor

## ABSTRACT

### QUASI-TRANSIENT CALCULATION OF SURFACE TEMPERATURES ON A REUSABLE BOOSTER SYSTEM WITH HIGH ANGLES OF ATTACK

Name: Morris, Seth Henderson  
University of Dayton

Advisor: Dr. Timothy J. Fry

The calculation of a recovery temperature based heat transfer coefficient proves to be sufficiently independent of wall temperature to use in a three dimensional, transient temperature model of a thermal protection system of a reusable booster concept. After a derivation of recovery temperature from the 1<sup>st</sup> law of thermodynamics, the weak dependence of the recovery temperature based heat transfer coefficient is investigated by 72 Computational Fluid Dynamics (CFD) models at angles of attack ranging from 0° to 90° over a range of Mach numbers, from Mach 2 to 5, and a variety of thermal boundary conditions at the wall, from isothermal to a conductive wall. Then, the heat transfer coefficient is calculated at many steady state CFD solutions for a reusable booster system concept on a given trajectory and applied to a transient Finite Element Analysis (FEA) model of a thermal protection system. Results are presented graphically.

## ACKNOWLEDGEMENTS

There are several people I would like to acknowledge for their support in my endeavors for the last two years. Their names are listed in alphabetical order by last name.

1. Mom and Pop, for their continuing support of me through the years, through the good times and the bad.
2. Trina Bornejko, Air Force Research Labs, for providing funding for the topic.
3. Dr. Jose Camberos, Air Force Research Labs and University of Dayton, for teaching me the theory of computational fluid dynamics and challenging me to think and work harder.
4. Dr. John Doty, University of Dayton, for serving on my thesis committee.
5. Michael Frede, for supplying the trajectory.
6. Dr. Timothy Fry, University of Dayton Research Institute, for serving as the chair to my thesis committee and for his generous support of my efforts, providing the necessary training, software, and networking me with skilled people to carry out my research efforts.
7. Herbert Stumph, University of Dayton Research Institute, for his support in teaching me how to code, script, and use FEA software.
8. Michael Swindeman, University of Dayton Research Institute, for his strong knowledge in heat transfer and help with the direction of the research.

9. Dr. Jeffery Zweber, Air Force Research Labs, for providing funding and the applied problem.

---

This research was sponsored by University of Dayton Research Institute and funded by a contract through the United States Air Force. Much appreciation goes to both entities for their support of this research. This thesis paper has been cleared for public release (Case Number 88ABW-2011-5837).

## TABLE OF CONTENTS

ABSTRACT	iii
ACKNOWLEDGEMENTS	iv
LIST OF ILLUSTRATIONS	viii
LIST OF TABLES	xiv
LIST OF SYMBOLS	xv
CHAPTER 1 – INTRODUCTION AND PROBLEM DESCRIPTION	1
CHAPTER 2 – THE DERIVATION OF RECOVERY TEMPERATURE BASED HEAT TRANSFER COEFFICIENT FROM THE FIRST LAW OF THERMODYNAMICS	6
The First Law of Thermodynamics	6
Enthalpy, Internal Energy, and Specific Heat	10
The Speed of Sound	16
Recovery Temperature	18
CHAPTER 3 – LOWER ORDER METHODS TO CALCULATE WALL TEMPERATURE	23
Recovery Temperature	23
Aeroheating and Thermal Analysis Code	24
Steady-State Navier-Stokes Computational Fluid Dynamics	29
CHAPTER 4 – QUANTIFYING THE DEPENDENCY OF THE HEAT TRANSFER COEFFICIENT WITH RESPECT TO WALL TEMPERATURE	34
Weakly Dependent Heat Transfer Coefficient	34
The Wing Model	34

Grid Convergence Study	42
Quantifying the Wall Temperature Dependency in the Heat Transfer Coefficient	45
CHAPTER 5 – THE APPLIED PROBLEM	59
A Rocket-back Trajectory	60
Geometry	61
The Universal Mesh	62
Problem Set-up and Solution Procedure	66
Computational Resources	66
Energy Balance	67
FEA TPS Model	68
Results	70
CHAPTER 6 – CONCLUSIONS AND RECOMMENDATIONS	76
Conclusions	76
Further Research	77
BIBLIOGRAPHY	81
APPENDIX A – HEAT TRANSFER COEFFICIENT VARIABILITY PLOTS AND WALL TEMPERATURE PLOTS	83
APPENDIX B – WEAK DEPENDENCE QUANTIFICATION STUDY JOB CODE AND BOUNDARY CONDITION LIST	87
APPENDIX C – SUMMARY OF STEADY STATE 3-D CFD RUNS AND FLIGHT CONDITIONS	90



## LIST OF ILLUSTRATIONS

Figure 1-1 – Geometry of NACA 23012 airfoil.	3
Figure 1-2 – Geometry of a reusable booster system concept.	4
Figure 1-3 – The trajectory used for a reusable booster system concept.	5
Figure 2-1 – A fully reversible thermodynamic process.	7
Figure 2-2 – Equilibrium composition of air at $p = 10^{-2} \text{ atm}$ as a function of the temperature.	15
Figure 2-3 – Flow through a disturbance.	16
Figure 2-4 – Mach number contours for an airfoil flying at Mach 5 and $45^\circ$ angle of attack.	22
Figure 2-5 – Temperature contours for an airfoil flying at Mach 5 and $45^\circ$ angle of attack.	22
Figure 3-1 – ATAC symmetric surface grid of the reusable booster concept.	25
Figure 4-1 – Grid of the NACA 23012 airfoil used in the two-dimensional wall temperature dependency analysis.	35
Figure 4-2 – Enlarged view of high aspect ratio region.	36
Figure 4-3 – Graphic of $\theta_{max}$ and $\theta_{min}$ .	36
Figure 4-4 – Enlarged view of the region with the highest skewness.	37
Figure 4-5 – Sensitivity of the Wilcox $k - \omega$ turbulence model to the free-stream turbulence levels for the Mach 8 sharp cone.	40
Figure 4-6 – Example of residuals versus iteration number. “Intermit” and “retheta” are turbulence parameters for turbulence intermittency and $Re_\theta$ .	42

Figure 4-7 – Wall temperature as a function of path length for each grid, zoomed on the leading edge.	44
Figure 4-8 – Wall temperature as a function of path length for each grid for the entire surface of the airfoil.	44
Figure 4-9 – Enlarged view of the results near the trailing edge of the airfoil, depicting the recirculation zone.	45
Figure 4-10 – Comparison of $Q/Q_{max}$ vs. variation in $h_r$ for each isothermal boundary condition.	48
Figure 4-11 – Comparison of $Q/Q_{max}$ vs. variation in $h_r$ for each isothermal boundary condition and one REWT boundary condition.	49
Figure 4-12 – Comparison of % variation in recovery temperature based heat transfer coefficient as a function of path length along the surface of the wing for each 9 variations in wall boundary conditions at Mach 2 and $\alpha = 0^\circ$ .	50
Figure 4-13 – Comparison of % variation in recovery temperature based heat transfer coefficient as a function of path length along the surface of the wing for each 9 variations in wall boundary conditions at Mach 5 and $\alpha = 0^\circ$ .	50
Figure 4-14 – Comparison of % variation in recovery temperature based heat transfer coefficient as a function of path length along the surface of the wing for each 9 variations in wall boundary conditions at Mach 5 and $\alpha = 15^\circ$ .	51
Figure 4-15– Comparison of % variation in recovery temperature based heat transfer coefficient as a function of path length along the surface of the wing for each 9 variations in wall boundary conditions at Mach 5 and $\alpha = 45^\circ$ .	51
Figure 4-16 – Comparison of % variation in recovery temperature based heat transfer coefficient as a function of path length along the surface of the wing for each 9 variations in wall boundary conditions at Mach 5 and $\alpha = 90^\circ$ .	52
Figure 4-17 –Comparison of $Q/Q_{max}$ as a function of % variation in recovery temperature based heat transfer coefficient at Mach 2 and $\alpha = 0^\circ$ .	52
Figure 4-18 – Comparison of $Q/Q_{max}$ as a function of % variation in recovery temperature based heat transfer coefficient at Mach 5 and $\alpha = 0^\circ$ .	52
Figure 4-19 – $Q/Q_{max}$ as a function of % variation in recovery temperature based heat transfer coefficient at Mach 5 and $\alpha = 45^\circ$ .	53

Figure 4-20 – $Q/Q_{max}$ as a function of % variation in recovery temperature based heat transfer coefficient at Mach 5 and $\alpha = 90^\circ$ .	53
Figure 4-21 – Separated flow behind the airfoil at Mach 5 and $\alpha = 45^\circ$ .	54
Figure 4-22 – Separated flow behind the airfoil at Mach 5 and $\alpha = 90^\circ$ .	54
Figure 4-23 – Wall temperature as a function of path length for Mach 2 and $\alpha = 0^\circ$ .	55
Figure 4-24 – Wall temperature as a function of path length for Mach 5 and $\alpha = 0^\circ$ .	55
Figure 4-25 – Wall temperature as a function of path length for Mach 5 and $\alpha = 90^\circ$ .	56
Figure 4-26 – Illustration of the separation and recirculation around the rear of the vehicle. The streamlines are plotted on the center plane. 30% translucency is applied to the center plane.	57
Figure 5-1 – Schematic of the solution process used in the applied problem.	59
Figure 5-2 – Angle of attack and geodetic altitude of the given trajectory. The rocket-back maneuver starts at 153 seconds and ends at 193 seconds	60
Figure 5-3 – Mach number and dynamic pressure of the given trajectory.	60
Figure 5-4 – Angle of attack of the coarsened trajectory used in the applied problem.	61
Figure 5-5 – Mach number and dynamic pressure of the coarsened trajectory used in the applied problem.	61
Figure 5-6 – Outer mold line of the reusable booster system concept.	62
Figure 5-7 – Rear shot of the outer mold line of the reusable booster system. No engines are modeled.	62
Figure 5-8 – The computational grid near the wall of the reusable booster system concept.	63
Figure 5-9 – Detail of the inflation layer.	64
Figure 5-10 – Estimate of the boundary layer thickness using Prandtl's boundary-layer equation.	64

Figure 5-11 – Vector plot of the boundary layer thickness at Mach 5.6, altitude of 188,000 <i>ft</i> and, 5 <i>ft</i> distance from the leading edge of the nose.	65
Figure 5-12 – Cross sectional view of the computational domain showing the dynamic zone (green spherical region) and the stationary zone (beige region).	65
Figure 5-13 – Three-dimensional sectioned view of the dynamic zone inside the stationary zone.	65
Figure 5-14 – Non conformal interface.	65
Figure 5-15 – Wall clock time and CPU time as a function of number of cores in the scalability study.	67
Figure 5-16 – Wall clock $\frac{t_{max}}{t}$ and CPU $\frac{t_{max}}{t}$ as a function of number of cores in the scalability study.	67
Figure 5-17 – CFD results from the radiation equilibrium wall temperature boundary condition.	68
Figure 5-18 – Temperature field based on the balance of the energy equation, Equation (5-2).	68
Figure 5-19 – FEA grid used in the transient heat transfer analysis, which has 11,912 shell elements.	69
Figure 5-20 – CFD grid at the wall boundary, which has 469,396 faces at the wall.	69
Figure 5-21 – Temperature profile comparison of steady state CFD and transient TPS analysis for $M = 4$ , $\alpha = 4.87^\circ$ , and $z = 130,000$ <i>ft</i> at the symmetry plane $y = 0$ <i>ft</i> .	71
Figure 5-22 – Temperature profile comparison of steady state CFD and transient TPS analysis for $M = 6.32$ , $\alpha = 82.1^\circ$ , and $z = 209,000$ <i>ft</i> at the symmetry plane $y = 0$ <i>ft</i> .	72
Figure 5-23 – Temperature profile comparison of steady state CFD and transient TPS analysis for $M = 3.28$ , $\alpha = 151.3^\circ$ , and $z = 285,000$ <i>ft</i> at the symmetry plane $y = 0$ <i>ft</i> .	73
Figure 5-24 – Steady state temperature contour for $M = 4$ , $\alpha = 4.87^\circ$ , and $z = 130,000$ <i>ft</i> .	74
Figure 5-25 – Transient temperature contour for $M = 4$ , $\alpha = 4.87^\circ$ , and $z = 130,000$ <i>ft</i> .	74

Figure 5-26 – Steady state temperature contour for $M = 6.32$ , $\alpha = 82.1^\circ$ , and $z = 209,000 \text{ ft}$ .	74
Figure 5-27 – Transient temperature contour for $M = 6.32$ , $\alpha = 82.1^\circ$ , and $z = 209,000 \text{ ft}$ .	74
Figure 5-28 – Steady state temperature contour for $M = 3.28$ , $\alpha = 151.3^\circ$ , and $z = 285,000 \text{ ft}$ .	75
Figure 5-29 – Transient temperature contour for $M = 3.28$ , $\alpha = 151.3^\circ$ , and $z = 285,000 \text{ ft}$ .	75
Figure 6-1 – Turbulent recirculation zone behind an airfoil at a $90^\circ$ angle of attack.	79
Figure A-1 – Comparison of % variation in recovery temperature based heat transfer coefficient as a function of path length along the surface of the wing for each 9 variations in wall boundary conditions at Mach 2 and $\alpha = 15^\circ$ .	83
Figure A-2 – Comparison of % variation in recovery temperature based heat transfer coefficient as a function of path length along the surface of the wing for each 9 variations in wall boundary conditions at Mach 2 and $\alpha = 45^\circ$ .	83
Figure A-3 – Comparison of % variation in recovery temperature based heat transfer coefficient as a function of path length along the surface of the wing for each 9 variations in wall boundary conditions at Mach 2 and $\alpha = 90^\circ$ .	84
Figure A-4 – $Q/Q_{max}$ as a function of % variation in recovery temperature based heat transfer coefficient at Mach 2 and $\alpha = 15^\circ$ .	84
Figure A-5 – $Q/Q_{max}$ as a function of % variation in recovery temperature based heat transfer coefficient at Mach 5 and $\alpha = 15^\circ$ .	84
Figure A-6 – $Q/Q_{max}$ as a function of % variation in recovery temperature based heat transfer coefficient at Mach 2 and $\alpha = 45^\circ$ .	84
Figure A-7 – $Q/Q_{max}$ as a function of % variation in recovery temperature based heat transfer coefficient at Mach 2 and $\alpha = 90^\circ$ .	85
Figure A-8 – Wall temperature as a function of path length for Mach 2 and $\alpha = 15^\circ$ .	85
Figure A-9 – Wall temperature as a function of path length for Mach 5 and $\alpha = 15^\circ$ .	85
Figure A-10 – Wall temperature as a function of path length for Mach 2 and $\alpha = 45^\circ$ .	85

Figure A-11 – Wall temperature as a function of path length for Mach 5 and  $\theta = 45^\circ$ . 86

Figure A-12– Wall temperature as a function of path length for Mach 2 and  $\theta = 90^\circ$ . 86

## LIST OF TABLES

Table 4-1 – Ranges and coefficient values for the piecewise polynomial model of specific heat $C_p$ .	38
Table 4-2 – Boundary conditions for CFD jobs used in Study A of quantifying the variation in the weak dependence assumption.	39
Table 4-3 – Summary of the cases studied in Figure 4-5, showing the variations in free-stream turbulent viscosity ratio and turbulence intensity.	41
Table 4-4 – Summary of the grids used in the grid convergence study.	43
Table 5-1 – Material thickness for the thermal protection system model.	70
Table 5-2 – Material thermal properties for the thermal protection system model.	70
Table B-1 – Job code for the weak dependence assumption quantification study and the corresponding boundary conditions.	87
Table C-1 – Job name, mission time, integrated total surface heat flux, Mach number, dynamic pressure, and angle of attack for each CFD analysis performed in the applied problem.	90

## LIST OF SYMBOLS

$\alpha$	=	Angle of attack, degrees.
$\beta$	=	Total path length.
$\gamma$	=	Ratio of specific heats.
$\delta^*$	=	Boundary layer displacement thickness, displacement thickness based on edge properties.
$\delta$	=	Boundary layer thickness.
$\varepsilon$	=	Variation, emissivity.
$\eta$	=	Angle between the wind vector and the outward surface normal.
$\Theta$	=	Boundary layer momentum thickness.
$\theta$	=	Cell edge angle, angle of the node with respect to the positive horizontal.
$\theta_D$	=	Characteristic temperature of a gas.
$\mu$	=	Dynamic viscosity.
$\mu_t$	=	Turbulent dynamic viscosity.
$\rho$	=	Mass density.
$\sigma$	=	Stefan-Boltzmann constant.
$\tau_w$	=	Wall shear.
$\bar{\bar{\tau}}$	=	Stress tensor.



$(\tau_{ij})_{\text{eff}}$	=	Deviatoric stress tensor.
$\Phi$	=	Boundary layer energy thickness.
$\omega$	=	Dissipation per unit turbulence kinetic energy.
$\mathbf{a}$	=	Acceleration (vector quantity).
$a$	=	Speed of sound.
$c$	=	Constant.
$\frac{C_f}{2}$	=	Friction factor.
$C_h$	=	Stanton number.
$C_p$	=	Coefficient of pressure in the stream-wise direction.
$C_p^*$	=	Coefficient of pressure in the direction of the wind.
$c_p$	=	Specific heat capacity at constant pressure.
$c_v$	=	Specific heat capacity at constant volume.
$da$	=	Differential speed of sound.
$dE$	=	Differential energy.
$d(KE)$	=	Differential kinetic energy.
$dp, dP$	=	Differential pressure.
$\partial p, \partial P$	=	Partial differential pressure.
$d(PE)$	=	Differential potential energy.
$d\mathbf{r}$	=	Differential position vector of some point on the body (vector quantity).
$\partial\mathbf{r}$	=	Partial differential position vector of some point on the body (vector quantity).
$d\rho$	=	Differential mass density.

$\partial\rho$	=	Partial differential density.
$ds$	=	Differential curve length.
$\delta T$	=	Inexact differential of temperature.
$dt$	=	Differential time.
$\partial t$	=	Partial differential time.
$du$	=	Differential $u$ – velocity.
$\partial u$	=	Partial differential $x$ – velocity.
$dV$	=	Differential volume.
$d\mathbf{v}$	=	Differential velocity (vector quantity).
$\partial w$	=	Partial differential $z$ – velocity.
$dw$	=	Differential $z$ – velocity.
$dx$	=	Differential $x$ – position.
$\mathbf{F}$	=	Force, external body force (vector quantity).
$F$	=	Entrainment shape factor.
$\mathbf{g}$	=	Gravity (vector quantity).
$H$	=	Enthalpy.
$H$	=	Shape factor.
$h$	=	Specific enthalpy, free-stream based heat transfer coefficient.
$h_r$	=	Recovery temperature based heat transfer coefficient, specific recovery enthalpy.
$H_s, H_t$	=	Stagnation (total) enthalpy.
$h_s, h_t$	=	Specific stagnation enthalpy.

$h_w$	=	Wall enthalpy.
$I$	=	Unit tensor.
$k$	=	Thermal conductivity, kinetic energy per unit mass of the turbulent fluctuations.
$KE$	=	Kinetic energy.
$ke$	=	Kinetic energy per unit mass.
$M$	=	Mach number.
$m$	=	Mass.
$\nabla$	=	Vector differential operator, del operator (vector quantity).
$P, p$	=	Pressure.
$P_\infty$	=	Far-field pressure.
$PE$	=	Potential energy.
$Pr$	=	Prandtl number.
$Q, q$	=	Heat flux per unit area.
$\dot{q}_w$	=	Wall heat flux.
$R$	=	Gas constant.
$r$	=	Recovery factor.
$r_l$	=	Laminar recovery factor.
$r_t$	=	Turbulent recovery factor.
$Re_\theta$	=	Momentum thickness Reynolds number.
$s$	=	Entropy, constant entropy, distance along path.
$S_h$	=	Source term.

$S_m$	=	Source mass.
$T$	=	Temperature.
$T_\infty$	=	Far-field temperature.
$T_r$	=	Recovery temperature.
$T_s$	=	Stagnation temperature.
$T_w$	=	Wall temperature.
$\mathbf{t}$	=	Streamline trace (vector quantity).
$U$	=	Internal energy.
$u$	=	Specific internal energy, $x$ – velocity.
$u_0$	=	Free-stream velocity.
$V$	=	Volume.
$\mathbf{v}$	=	Velocity (vector quantity).
$v$	=	Specific volume.
$x$	=	$x$ – coordinate of the node along the wall.
$x_{loc}$	=	$x$ – location of the geometric center.
$y$	=	$y$ – coordinate of the node along the wall.
$\bar{y}$	=	Shock radial location through which the boundary layer edge streamline has passed.
$y_{loc}$	=	$y$ – location of the geometric center.
$z$	=	Altitude.

## CHAPTER 1

### INTRODUCTION AND PROBLEM DESCRIPTION

The calculation of external surface temperatures due to aerodynamic heating often presents technical difficulties for thermal protection system (TPS) engineers. The transient surface temperatures of a high speed vehicle are difficult to calculate due to numerous factors. Examples of these difficulties are transient flow-field effects, material properties of the TPS, and accuracy of the solver or the solution process. The complexities involved in the calculation of the transient temperatures present a need for research of improved methods of analysis. In the past, TPS temperature calculation methods relied on highly simplified models. With modern computing power, these models have the potential to be more realistic; thus, the research for these alternate methods of calculation tends towards higher fidelity. This thesis investigates a process for calculating transient surface temperatures on a hypersonic vehicle that, at some points in a given flight trajectory, flies at high angles of attack. The improved analysis method described in this thesis utilizes Navier-Stokes Computational Fluid Dynamics (CFD) while decoupling the aerothermal heating from the transient temperature profile of the TPS.

Past methods of calculation of temperature profiles used in sizing the TPS include recovery temperature calculations for peak heating at the leading edges, lower fidelity, engineering level codes such as Aeroheating and Thermal Analysis Code (ATAC) and Hypersonic Engineering Aerothermodynamic Trajectory Tool Kit (HEAT-TK), and steady state CFD. The ultimate model of heat transfer is a transient, conjugate, coupled heat

transfer model where the internal structure, heat sources and sinks, TPS, rocket engines, and plumes are all modeled along with a transient external aerothermal calculation. However, this level of completeness and integration is not yet possible in a rapid design environment as the time-steps required for external, turbulent, separating, hypersonic flow are many orders of magnitude smaller than the length of the flight trajectory. For this reason we seek a method that decouples the external aerothermal calculation from the transient TPS temperature calculation.

The decoupled method performed here uses steady state CFD solutions at specific points in the trajectory to generate a field of heat transfer coefficients based on the recovery temperature:

$$h_r = \frac{q}{T_w - T_r} \quad (1-1)$$

In Equation (1-1)  $q$  is the heat flux per unit area,  $T_w$  is the wall temperature, and  $T_r$  is the recovery temperature. Numerous heat transfer coefficient fields are calculated over the entire vehicle surface based on far field pressure, far field temperature, free stream Mach number, and vehicle angle of attack. This collection of fields covers the full operating range of the vehicle for the trajectories to be analyzed. Next, a particular field from the collection is selected based on the flight conditions of the trajectory time-step under consideration. This particular field is held constant throughout the time-step and a different field is selected for the subsequent time-step. The specific heat transfer coefficient field serves as the convective boundary condition on a TPS transient thermal model. This process is repeated for each time-step in the entire trajectory resulting in a complete calculation of the transient TPS temperature profile.

In order to employ this method, the variation associated with the recovery temperature based heat transfer coefficient with regard to wall temperature must be

investigated. It is well known that a heat transfer coefficient calculated with respect to either free stream or boundary layer edge temperature is highly dependent on wall temperature variations. However, a HTC based on recovery temperature does not exhibit this tendency. For this reason, the recovery temperature based heat transfer coefficient is significantly more useful for solving the TPS temperature problem in a decoupled manner. There is a large amount of work performed in quantifying the wall temperature dependency of the heat transfer coefficients based on the thermal boundary conditions of the wall used in the solution process.

Quantifying the variation of the recovery temperature based heat transfer coefficient with regards to wall temperature follows this process:

1. Generate CFD data with various thermal boundary conditions at the wall.
2. Calculate the recovery temperature at each CFD cell along the wall for each boundary condition.
3. Calculate the heat transfer coefficient based on recovery temperature, Equation (1-1). This is performed for each wall boundary condition.
4. Calculate the mean heat transfer coefficient of all the wall boundary conditions.
5. Calculate the percent difference from the mean.
6. Investigate the results



**Figure 1-1** – Geometry of NACA 23012 airfoil.

In order to rapidly quantify the wall temperature dependency of the heat transfer coefficient based on recovery temperature, a simple geometry is used. The geometry chosen is a NACA 23012 airfoil with a 2.5m chord length, as depicted in Figure 1-1. The CFD data is generated at various flight conditions, such as different angles of attack and Mach numbers.

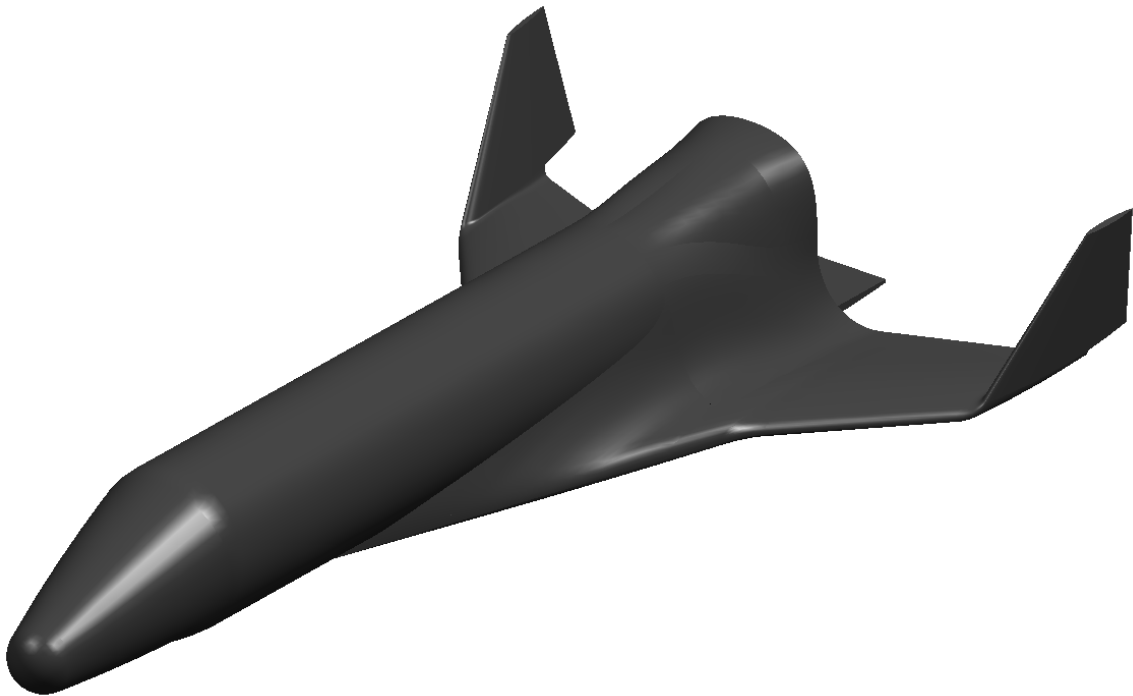


**Figure 1-2** – Geometry of a reusable booster system concept.

Once the variability in the recovery temperature based heat transfer coefficient is quantified, this method is applied to a three-dimensional geometry flying a given trajectory. The geometry used is a reusable booster system concept supplied by the United States Air Force Research Labs, shown in Figure 1-2. The trajectory, internally supplied, shows three stages: ascent, shown in blue, rocket-back, shown in red, and entry, shown in green. The vehicle in this trajectory flies at a maximum speed of just over Mach 6.3, a maximum angle of attack of approximately  $151^\circ$ , and a maximum altitude of just over 300,000 feet.



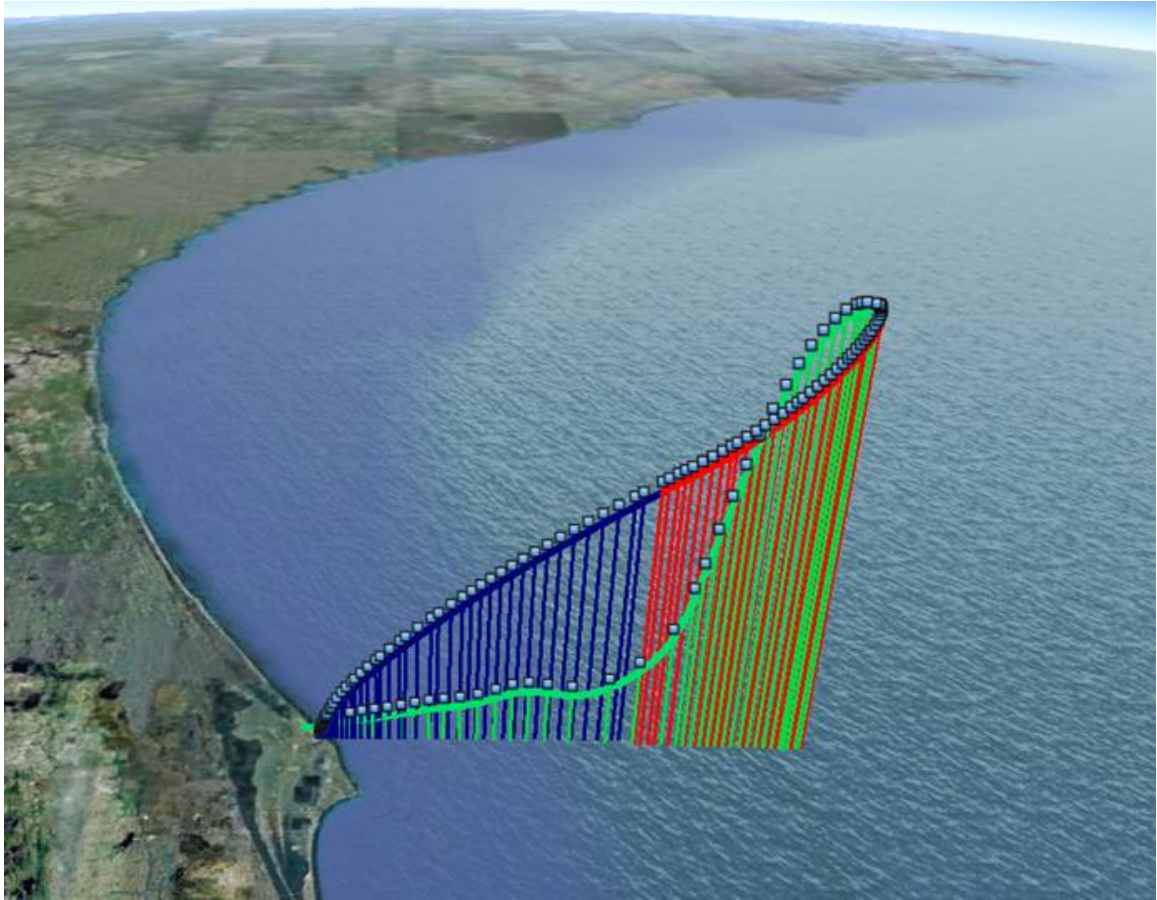


**Figure 1-3** – The trajectory used for a reusable booster system concept.

## CHAPTER 2

### THE DERIVATION OF RECOVERY TEMPERATURE BASED HEAT TRANSFER COEFFICIENT FROM THE FIRST LAW OF THERMODYNAMICS

In this chapter, the concepts are developed in order to calculate temperature rise in a fluid due to a rapid change in velocity. Working in a vehicle-centered coordinate system, the fluid experiences this rapid deceleration when it flows from the far-field domain to the wall of the vehicle, where the fluid reaches zero velocity. Finding an expression for this rise in temperature is best done using thermodynamic processes, starting from the first law of thermodynamics.

We are concerned with high speed, ideal gas flows. Because the kinetic energy is so dominant in this type of flow, the gravity vector can be ignored; thus, potential energy can be ignored.

#### **The First Law of Thermodynamics**

The first law of thermodynamics: “during any cycle a system (control mass) undergoes, the cyclic integral of the heat is proportional to the cyclic integral of the work” (Sonntag, Borgnakke and Van Wylen 116). Mathematically, then, this is represented as the following equation:

$$\oint \delta Q = \oint \delta W \quad (2-1)$$

If we take Equation (2-1) in the context of a cycle that goes from state 1 to state 2, and use energy,  $E$ , we can analyze Equation (2-1). Graphically, we have illustrated this in Figure 2-1.

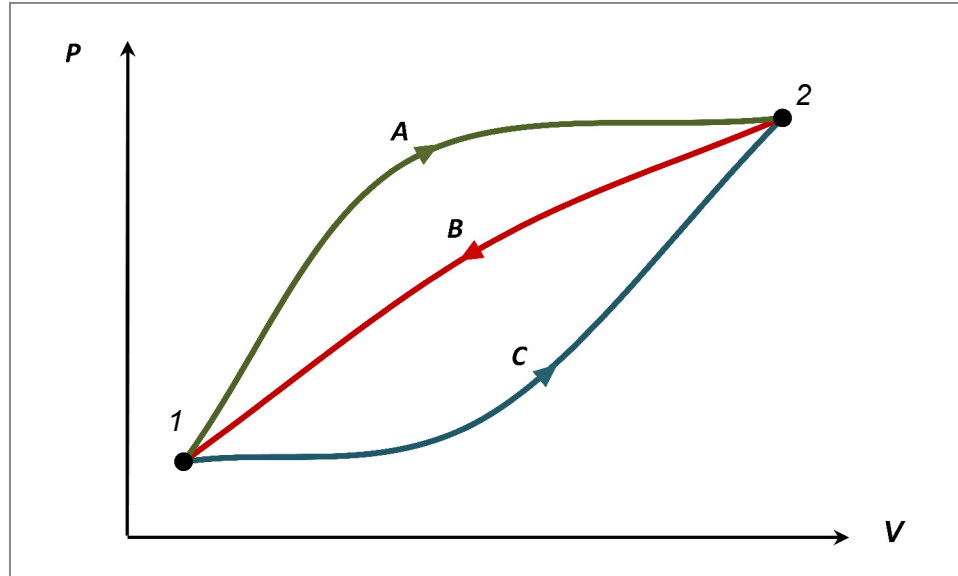


**Figure 2-1** – A fully reversible thermodynamic process.

The mathematical representation of Figure 2-1, for processes  $A$  and  $B$  is as follows:

$$\int_1^2 \delta Q_A + \int_2^1 \delta Q_B = \int_1^2 \delta W_A + \int_2^1 \delta W_B \quad (2-2)$$

Processes  $B$  and  $C$  are as follows:

$$\int_1^2 \delta Q_C + \int_2^1 \delta Q_B = \int_1^2 \delta W_C + \int_2^1 \delta W_B \quad (2-3)$$

Subtracting Equation (2-3) from Equation (2-2), we have:

$$\int_1^2 \delta Q_A - \int_1^2 \delta Q_C = \int_1^2 \delta W_A - \int_1^2 \delta W_C$$

Or,

$$\int_1^2 (\delta Q - \delta W)_A = \int_1^2 (\delta Q - \delta W)_C \quad (2-4)$$

Because  $A$  and  $C$  represent arbitrary processes between states 1 and 2, the quantity  $\delta Q - \delta W$  is the same for all processes between states 1 and 2. Therefore,  $\delta Q - \delta W$  depends only on the initial and final states and not on the path followed between the two states (Sonntag, Borgnakke and Van Wylen 118). Hence, we deduce that the process is really a “point function,” or it can be represented as a differential property of the mass. This differential property is called energy:

$$dE = \delta Q - \delta W \quad (2-5)$$

Integrating Equation (2-5) from point 1 to 2:

$$E_2 - E_1 = {}_1Q_2 - {}_1W_2 \quad (2-6)$$

Where  $E_1$  and  $E_2$  are the initial and final values of the energy in the control mass,  $Q$  is the heat transferred to the control mass during the process from state 1 and 2, and  $W$  is the work done by the control mass during the process. The energy term may be broken down into three basic components:

$$E = U + KE + PE \quad (2-7)$$

Where  $U$  is the internal energy,  $KE$  is the kinetic energy, and  $PE$  is the potential energy.

Equation (2-7) may also be written in differential form:

$$dE = dU + d(KE) + d(PE) \quad (2-8)$$

Combining Equations (2-8) and (2-5), we have:

$$dU + d(KE) + d(PE) = \delta Q - \delta W \quad (2-9)$$

In order to find the kinetic energy, we assume no heat transfer or change in internal energy. Recalling that  $W = \mathbf{F} \cdot \mathbf{x}$ , Equation (2-9) simplifies to:

$$\delta W = -\mathbf{F} \cdot d\mathbf{x} = -d(KE)$$

$$\mathbf{F} = m\mathbf{a} = m \frac{d\mathbf{v}}{dt} = m \frac{d\mathbf{x}}{dt} (\nabla \cdot \mathbf{v}) = m\mathbf{v}(\nabla \cdot \mathbf{v})$$

Combining the above two equations, we have:

$$d(KE) = \mathbf{F} \cdot d\mathbf{x} = m\mathbf{v} \cdot d\mathbf{v}$$

Integrating the above equation, we get:

$$\int_0^{KE} d(KE) = \int_0^{\mathbf{v}} m\mathbf{v} \cdot d\mathbf{v}$$

$$KE = \frac{1}{2}m\mathbf{v}^2 \quad (2-10)$$

We will define the kinetic energy per unit mass as

$$ke = \frac{1}{2}\mathbf{v}^2 \quad (2-11)$$

Equation (2-11) will become useful later, in our discussion of total enthalpy.

In order to express internal energy, we substitute the differential expression for kinetic energy into Equation (2-8):

$$dE = dU + m\mathbf{v} \cdot d\mathbf{v} \quad (2-12)$$

Integrating the above equation,

$$E_2 - E_1 = U_2 - U_1 + \frac{m\mathbf{v}_2^2}{2} - \frac{m\mathbf{v}_1^2}{2} \quad (2-13)$$

If we take the differential expression for kinetic energy and substitute it into Equation (2-9), we have:

$$dU + \frac{d(m\mathbf{v}^2)}{2} = \delta Q - \delta W \quad (2-14)$$

Substituting Equation (2-13) into (2-6),

$$(U_2 - U_1) + \left( \frac{m\mathbf{v}_2^2}{2} - \frac{m\mathbf{v}_1^2}{2} \right) = {}_1Q_2 - {}_1W_2 \quad (2-15)$$

Equation (2-15) is the form of the energy equation that will be used here.

## Enthalpy, Internal Energy, and Specific Heat

Enthalpy is defined by considering a system that has no change in kinetic energy.

When considering this type of system, Equation (2-15) reduces to:

$$(U_2 - U_1) = {}_1Q_2 - {}_1W_2$$

And the work is simply

$$\int_1^2 P dV = {}_1W_2$$

Because the pressure is held constant in this example, it falls outside the integral, and

$$P(V_2 - V_1) = {}_1W_2$$

And

$$(U_2 + P_2V_2) - (U_1 + P_1V_1) = {}_1Q_2$$

Thus, enthalpy can be defined by the following equation (Sonntag, Borgnakke and Van Wylen 130):

$$H \equiv U + PV$$

And on a per unit mass basis, the specific enthalpy  $h$  is:

$$h \equiv u + Pv \quad (2-16)$$

If we do not neglect kinetic energy, which is necessary high-speed flows, then Equation (2-15) becomes:

$$(U_2 - U_1) + \left( \frac{m\mathbf{v}_2^2}{2} - \frac{m\mathbf{v}_1^2}{2} \right) = {}_1Q_2 - {}_1W_2$$

Which, using the same analysis as above, we have:

$$\left( U_2 + P_2V_2 + \frac{m\mathbf{v}_2^2}{2} \right) - \left( U_1 + P_1V_1 + \frac{m\mathbf{v}_1^2}{2} \right) = {}_1Q_2$$

The above equation can be used to define stagnation enthalpy, which accounts for the kinetic energy of the fluid:

$$H_s \equiv U + PV + \frac{1}{2}m\mathbf{v}^2$$

The above equation in a per-unit mass basis:

$$h_s \equiv u + Pv + \frac{1}{2}\mathbf{v}^2$$

Or simply,

$$h_s \equiv h + \frac{1}{2}\mathbf{v}^2 \quad (2-17)$$

Equation (2-17) is simply the sum of the specific enthalpy, (2-16) and the specific kinetic energy, (2-11).

The constant pressure specific heat,  $c_p$ , is frequently used in thermodynamic calculations. If we start with Equation (2-14), and disregarding the term for kinetic energy, we have:

$$\delta Q = \delta W + dU$$

$$\delta Q = dU + PdV$$

Integrating the above equation:

$$\int_1^2 dQ = \int_1^2 dU + \int_1^2 PdV$$

$P$  is constant in this case, so we have:

$$Q_2 - Q_1 = U_2 - U_1 + P(V_2 - V_1)$$

The resulting  $P(V_2 - V_1)$  term can be associated with the internal energy terms, similarly to enthalpy, which leads to the conclusion that the heat transfer can be expressed in terms of the enthalpy change. This results in:

$$c_p = \frac{1}{m} \left( \frac{\delta Q}{\delta T} \right)_p = \frac{1}{m} \left( \frac{\partial H}{\partial T} \right)_p = \left( \frac{\partial h}{\partial T} \right)_p \quad (2-18)$$

At constant volume, the work term  $PdV$  is zero. This results in:

$$c_v = \frac{1}{m} \left( \frac{\delta Q}{\delta T} \right)_v = \frac{1}{m} \left( \frac{\partial U}{\partial T} \right)_v = \left( \frac{\partial u}{\partial T} \right)_v \quad (2-19)$$

Although the derivations of specific heat were found by a specific process that neglected certain thermodynamic aspects such as kinetic energy, the resulting definition of specific heat is path independent:

Note that in each of these special cases, the resulting expression, [Equations (2-18) and (2-19)], contains only thermodynamic properties, from which we conclude that the constant volume and constant pressure specific heats must themselves be thermodynamic properties. This means that, although we began this discussion by considering the amount of heat transfer required to cause a unit temperature change and then proceeded through a very specific development leading to [Equations (2-18) and (2-19)], the result ultimately expresses a relation among a set of thermodynamic properties and therefore constitutes a definition that is independent of the particular process leading to it (in the same sense that the definition of enthalpy is independent of the process used to illustrate one situation in which the property is useful in a thermodynamic analysis). (Sonntag, Borgnakke and Van Wylen 134)

Recalling the ideal gas equation,

$$Pv = RT \quad (2-20)$$

And the definition for specific enthalpy, Equation (2-16):

$$h = u + Pv$$

Combining Equations (2-20) and (2-16), we have:

$$h = u + RT$$

If the internal energy is a function of temperature only,  $u = f(T)$ , then the enthalpy is a function of temperature only,  $h = f(T)$ . Thus, the partial derivatives in Equations (2-18) and (2-19) are actually ordinary derivatives for ideal gasses:

$$c_p = \left( \frac{dh}{dT} \right)_p \quad (2-21)$$

And



$$c_v = \left( \frac{du}{dT} \right)_v \quad (2-22)$$

Because  $h = u + pv = u + RT$ , then

$$\frac{dh}{dT} = \frac{dv}{dT} + R \frac{dT}{dT}$$

And

$$dh = dv + RdT \quad (2-23)$$

Solving for  $dh$  in Equation (2-21) and  $du$  in (2-22), and substituting these terms into Equation (2-23):

$$c_p dT = c_v dT + R dT$$

Collecting terms, and integrating with respect to temperature,

$$0 = \int_{T_1}^{T_2} (c_v + R - c_p) dT$$

$$0 = (c_v + R - c_p)(T_2 - T_1)$$

Thus,

$$c_v + R = c_p \quad (2-24)$$

We can also define the ratio of specific heats,  $\gamma = \frac{c_p}{c_v}$  in an alternate fashion, using Equation

(2-24):

$$\gamma = 1 + \frac{R}{c_v}$$

Or

$$1 + \frac{R}{c_p - R} = \gamma$$

$$c_p - R + R = \gamma(c_p - R)$$

$$c_p = \gamma c_p - R\gamma$$

$$\gamma c_p - c_p = R\gamma$$

$$c_p(\gamma - 1) = R\gamma$$

$$c_p = \frac{R\gamma}{\gamma - 1} \quad (2-25)$$

Equation (2-25) will become useful later.

Note that in our discussion leading to Equations (2-21) and (2-22), we assume an ideal gas, which, at the molecular level, assumes a limited number of degrees of freedom. For example, a diatomic molecule, such as air, can be modeled “as a rigid dumbbell, with [number of degrees of freedom] of 5” (Liepmann and Roshko 36). The specific heat of these diatomic gasses follow their ideal gas assumption over a wide range of temperatures, but at high temperatures,  $c_p$  falls away from this assumption “because the atoms in a diatomic molecule are not rigidly bound but can vibrate,” which classically adds two degrees of freedom (Liepmann and Roshko 36).

Real gasses are hard to model exactly, but many experiments have drawn empirical relations which can closely approximate a real gas’s behavior. According to Liepmann and Roshko, “the specific heat for a diatomic gas in the range of temperatures between dissociation and the region of van der Waals’ effects is closely approximated by:

$$\frac{c_p}{R} = \frac{7}{2} + \left[ \frac{\theta_v/2T}{\sinh(\theta_v/2T)} \right]^2$$

where  $\theta_v$  denotes a characteristic temperature for the vibrational energy” (Liepmann and Roshko 37).

In the CFD analyses in the following chapters, the peak temperatures in the flow-field never reach the temperatures required for dissociation of the molecules that comprise air. Hirschel provides a graph that relates mole percentage of different materials in air versus the temperature, Figure 2-2. These materials are diatomic nitrogen,  $N_2$ ; diatomic oxygen,  $O_2$ ; carbon dioxide,  $CO_2$ ; carbon monoxide,  $CO$ ; carbon,  $C$ ; nitric oxide,  $NO$ ;

monatomic nitrogen,  $N$ ; monatomic oxygen,  $O$ ; Argon,  $Ar$ ; electrons,  $e$ ; ionized monatomic nitrogen,  $N^+$ ; ionized monatomic oxygen,  $O^+$ ; ionized argon,  $Ar^+$ ; and ionized nitric oxide  $NO^+$ .

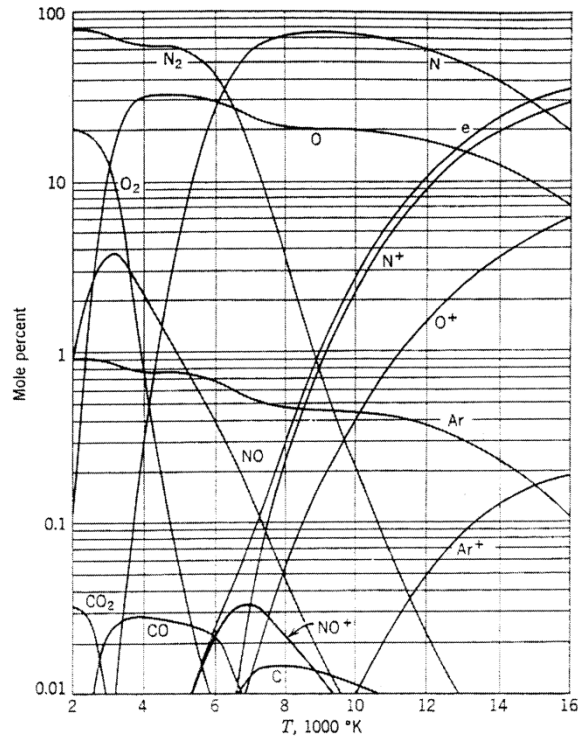


**Figure 2-2** – Equilibrium composition of air at  $p = 10^{-2} \text{ atm}$  as a function of the temperature (Hirschel 22).

We can see that in Figure 2-2, the real gas effects, which come with the ionization and dissociation of the particular molecules that comprise air, do not begin to occur until the temperature reaches  $\sim 3,500 \text{ K}$ , where diatomic nitrogen dissociates to two monatomic nitrogens. The mole percentages of monatomic nitrogen are quite small,  $< 1\%$ , up to  $\sim 4,500 \text{ K}$ . The approximation of an ideal gas for this thesis is therefore valid as the temperatures of the flow-field never go much above  $2,000 \text{ K}$ .

## The Speed of Sound

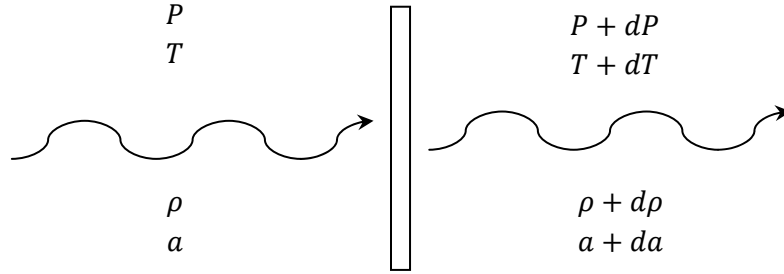


**Figure 2-3** – Flow through a disturbance.

Consider Figure 2-3, where  $P$  is the pressure,  $T$  is the temperature,  $\rho$  is the density, and  $a$  is the speed of sound. From the continuity equation, we have:

$$\rho_1 \mathbf{v}_1 = \rho_2 \mathbf{v}_2 \quad (2-26)$$

Applying Equation (2-26) to Figure 2-3 results in:

$$\rho a = (\rho + d\rho)(a + da)$$

Expanding, and neglecting terms of second-order smallness,

$$\rho a = \rho a + \rho da + a d\rho + \overbrace{d\rho da}^0$$

Reducing, and solving for the speed of sound:

$$a = -\rho \frac{da}{d\rho} \quad (2-27)$$

From the 1-dimensional momentum equation:

$$P_1 + \rho_1 \mathbf{v}_1^2 = P_2 + \rho_2 \mathbf{v}_2^2 \quad (2-28)$$

Applying Equation (2-28) to Figure 2-3, we have:

$$P + \rho a^2 = (P + dP) + (\rho + d\rho)(a + da)^2$$

Again, expanding, and using second-order smallness for the product of differentials,

$$P + \rho a^2 = (P + dP) + (\rho + d\rho) \left( a^2 + 2ada + \overbrace{(da)^2}^0 \right)$$

$$\begin{aligned}
P + \rho a^2 &= P + dP + \rho a^2 + 2\rho a da + a^2 d\rho + \overbrace{2a d\rho da}^0 \\
P + \rho a^2 &= P + dp + \rho a^2 + a^2 d\rho + 2\rho a da \\
0 &= dp + a^2 d\rho + 2\rho a da \\
2\rho a da &= -dp - a^2 d\rho \\
da &= \frac{-dp - a^2 d\rho}{2\rho a} \tag{2-29}
\end{aligned}$$

Solving Equation (2-27) for  $da$  and substituting the resulting term into (2-29),

$$a = -\rho \left( \frac{-dp - a^2 d\rho}{2\rho a d\rho} \right) = \frac{\rho \frac{dp}{d\rho} + a^2}{2a\rho}$$

Solving for  $a$ ,

$$\begin{aligned}
a^2 &= \frac{1}{2} \left( \frac{dp}{d\rho} + a^2 \right) \\
2a^2 - a^2 &= \frac{dp}{d\rho} \\
a^2 &= \frac{dp}{d\rho} \tag{2-30}
\end{aligned}$$

Because flow through a sound wave is isentropic, Equation (2-30) is the rate of change of pressure with respect to density, and the ordinary derivative, which is an isentropic change, can be expressed as a partial derivative. Hence,

$$a = \sqrt{\left( \frac{\partial p}{\partial \rho} \right)_s} \tag{2-31}$$

If we assume an ideal gas, the isentropic relation given by the following Equation holds (Anderson 558):

$$\frac{P_1}{P_2} = \left( \frac{\rho_1}{\rho_2} \right)^\gamma \tag{2-32}$$

From Equation (2-32), we get:

$$\frac{P}{\rho^\gamma} = c \quad (2-33)$$

Where  $c$  is a constant. Solving Equation (2-33) for  $P$  and differentiating with respect to  $\rho$ , we obtain:

$$\left(\frac{\partial P}{\partial \rho}\right)_s = c\gamma\rho^{\gamma-1} \quad (2-34)$$

Substituting the expression for the constant, Equation (2-33), into (2-34):

$$\begin{aligned} \left(\frac{\partial P}{\partial \rho}\right)_s &= \frac{P}{\rho^\gamma} \gamma \rho^{\gamma-1} \\ \frac{\partial P}{\partial \rho} &= \frac{\gamma P}{\rho} \end{aligned} \quad (2-35)$$

Substituting Equation (2-35) into Equation (2-31):

$$a = \sqrt{\frac{\gamma P}{\rho}} \quad (2-36)$$

If we substitute the ideal gas law,  $\frac{P}{\rho} = RT$  into Equation (2-36), we have:

$$a = \sqrt{\gamma RT} \quad (2-37)$$

And

$$a^2 = \gamma RT \quad (2-38)$$

### Recovery Temperature

Using the relationship expressed in Equation (2-38) and taking a ratio of the speed of sound at the stagnation point and the speed of sound at an arbitrary point, we see that:

$$\begin{aligned} \frac{a_s^2}{a^2} &= \frac{\gamma RT_s}{\gamma RT} \\ \frac{a_s^2}{a^2} &= \frac{T_s}{T} \end{aligned} \quad (2-39)$$

Recall the derivative definitions of the specific heats, Equations (2-21) and (2-22). Solving for the differential of enthalpy and internal energy, we have:

$$dh = c_p dT \quad (2-40)$$

$$du = c_v dT \quad (2-41)$$

We can integrate Equation (2-40):

$$h = c_p T \quad (2-42)$$

And recalling the definition for stagnation enthalpy, we can combine Equations (2-17) and (2-42):

$$h_s = c_p T + \frac{1}{2} \mathbf{v}^2$$

Because  $h_s = c_p T_s$ , we have:

$$c_p T_s = c_p T + \frac{1}{2} \mathbf{v}^2$$

Or

$$T_s = T + \frac{\mathbf{v}^2}{2c_p} \quad (2-43)$$

If we take the ratio of the stagnation temperature  $T_s$  and the temperature at some arbitrary point  $T$  in Equation (2-43), we arrive to the following expression:

$$\frac{T_s}{T} = 1 + \frac{\mathbf{v}^2}{2c_p T}$$

From our relationship found in Equation (2-25), we can revise the above expression:

$$\frac{T_s}{T} = 1 + \frac{\mathbf{v}^2(\gamma - 1)}{2\gamma RT}$$

Also, recall Equation (2-38),  $\gamma RT = a^2$ . The above Equation then becomes:

$$\frac{T_s}{T} = 1 + \frac{\mathbf{v}^2(\gamma - 1)}{2a^2}$$

Note the term  $\frac{\mathbf{v}^2}{a^2}$ , which is equal to the square of the Mach number. Hence,

$$\frac{T_s}{T} = 1 + \frac{(\gamma - 1)}{2} M^2$$

At last, we have an equation for stagnation temperature:

$$T_s = T \left[ 1 + \frac{(\gamma - 1)}{2} M^2 \right] \quad (2-44)$$

In high speed flows, a large amount of kinetic energy is carried simply by the motion of the flow. When the flow decelerates as it approaches the wall, the kinetic energy of the flow is converted to a temperature rise in the fluid.

The stagnation temperature is the temperature where all the kinetic energy is converted to thermal energy in the fluid as the fluid is slowed isentropically from its free-stream velocity to zero. However, in reality, there are viscous dissipative effects in the boundary layer and sub-layer; thus, a small amount of mass transport occurs normal to the direction of flow. These dissipative effects cause the actual temperature to be lower than what is predicted by the stagnation temperature; this temperature is referred to as recovery temperature.

We can introduce a recovery factor  $r$  to get the recovery temperature, which takes into account the small amount of mass transport, thereby reducing the temperature slightly below the stagnation temperature. The recovery temperature is:

$$T_r = T \left( 1 + r \frac{\gamma - 1}{2} M^2 \right) \quad (2-45)$$

where we would expect the recovery factor to be less than 1 in order to slightly reduce the temperature below the stagnation temperature. The Prandtl number is equal to the viscous diffusion rate divided by the thermal diffusion rate (White 79):

$$Pr = \frac{\mu c_p}{k} = \frac{\text{viscous diffusion rate}}{\text{thermal diffusion rate}} \quad (2-46)$$

The use of the Prandtl number is intuitive because the recovery temperature accounts for the small amount of mass and thermal diffusion occurring normal to the flow at the



stagnation point. Schlichting shows the experimentally found recovery factor for laminar flow in air (Schlichting 335):

$$r_t = r_{laminar} = \sqrt{Pr} \quad (2-47)$$

Schlichting also cites the recovery factor for turbulent flow in air, with experimental proof (Schlichting 713-714):

$$r_t = r_{turbulent} = \sqrt[3]{Pr} \quad (2-48)$$

In conclusion, we can witness the conversion of kinetic energy in the flow to a temperature rise through some CFD results. Although the flow is not isentropic, this process is somewhat reversible. In Figures 2-3 and 2-4, the incoming flow is Mach 5 and the angle of attack is 45°. The flow decelerates to stagnation, illustrated by the purple region near the front below the airfoil's surface in Figure 2-4, and creates a temperature rise, shown by the red region in Figure 2-5. The flow then moves around the left most tip of the airfoil and accelerates as it reaches the top of the airfoil, shown by the brown region above the airfoil's surface. This acceleration consumes thermal energy, and thus, the flow cools; this is the reversible process. This cool area is the light blue to dark blue region near the center of the airfoil above the airfoil's surface in Figure 2-5.

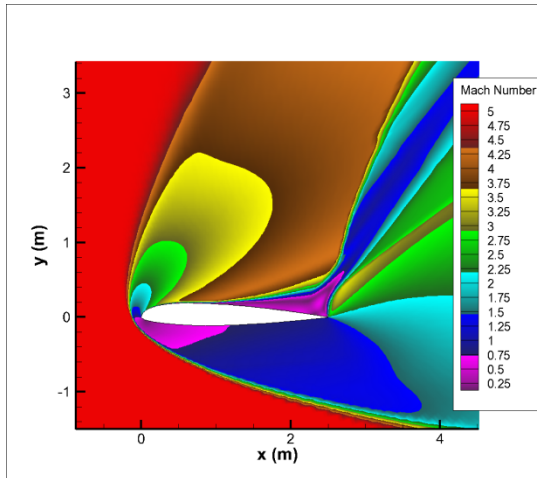


**Figure 2-4** – Mach number contours for an airfoil flying at Mach 5 and 45° angle of attack.

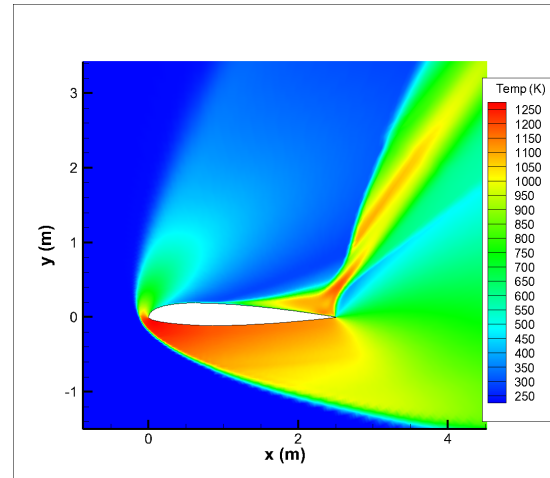


**Figure 2-5** – Temperature contours for an airfoil flying at Mach 5 and 45° angle of attack.

Near the back of the airfoil, flow separation occurs, and a region of recirculation is present. This causes the flow to slow to subsonic speeds, as depicted by the purple region near the rear of the airfoil in Figure 2-4. This then causes the fluid to again gain temperature, and this can be seen as the orange and light red region near the rear of the airfoil above the airfoil's surface.

Later, in Chapter 4, we will see that accounting for the kinetic energy of the flow by using the recovery temperature instead of free stream temperature in the formulation the heat transfer coefficient will reduce the heat transfer coefficient's dependence on wall temperature. Essentially, the recovery temperature based heat transfer coefficient is weakly dependent on wall temperature when compared to a standard formulation of heat transfer coefficient, which uses the free stream temperature.

## CHAPTER 3

### LOWER ORDER METHODS TO CALCULATE WALL TEMPERATURE

#### **Recovery Temperature**

The derivation in Chapter 2 shows how recovery temperature arises from a conversion of the kinetic energy in a fluid to the temperature in a fluid when the fluid decelerates to stagnation from a high speed. As witnessed in the course of this research project, the recovery temperature, using CFD generated Prandtl numbers, agrees very well with steady state CFD results on leading edges. Therefore, if flight conditions allow for steady state, ideal gas assumptions, the recovery temperature can be used as a means to calculate the peak temperature on the leading edges of the vehicle.

Steady state conditions rarely exist in real flights, however. Therefore, the recovery temperature method of calculating peak wall temperature for sizing the thermal protection system can over-predict the real wall temperature encountered in transient conditions. In addition, the recovery temperature only holds true for ideal gas flows, which is not a valid assumption in many re-entry problems, such as the Space Shuttle re-entering the atmosphere at Mach 20. The recovery temperature also fails to predict the heat rise in the fluid that is not caused by kinetic energy conversion.

Over a large portion of the vehicle, such as on the upper and lower surfaces of the wings and along the fuselage, the flow can be thought of as flow over a flat plate. In this case, higher temperatures are a result of viscous effects in the boundary layer, as opposed to the stagnation zone phenomena taking place on the nose and wing leading edges; the

temperature rise in the fluid comes from shearing the fluid. The recovery temperature does not account for the shear, only the kinetic energy, which is signified by the  $M^2$  term in Equation (3-1).

$$T_r = T \left( 1 + r \frac{\gamma - 1}{2} M^2 \right) \quad (3-1)$$

Thus, using the recovery temperature cannot predict the amount of thermal protection needed when the flow is parallel to the surface of the vehicle.

A better method of temperature calculation over the entire surface of the vehicle exists, which uses a surface grid on the geometry and streamlines through the surface grid to recognize when the flow is perpendicular or parallel to the surface of the vehicle. Aeroheating and Thermal Analysis Code (ATAC) is one of these methods.

### **Aeroheating and Thermal Analysis Code**

ATAC is widely used in the aerospace industry as a method to rapidly predict wall temperatures on a hypersonic vehicle geometry. ATAC is higher order than a simple recovery temperature calculation, but lower order than a Navier-Stokes CFD code.

ATAC does not grid the volume of the solution domain, as a Navier-Stokes CFD solver does. It uses a surface grid to generate streamlines, upon which it then performs various calculations. Figure 3-1 is an example of the ATAC surface grid on a reusable booster system concept geometry. As stated in the ATAC manual, the solution procedure consists of an “inviscid solution to provide the boundary layer edge conditions and the surface energy balance computations... provide the wall boundary conditions for the solution of the integral equations” (Strobel, Tillman and King 19). Because the inviscid portion of the flow-field dominates the pressure distribution, it can be used to reflect the state of the boundary layer edge properties. Subsequently, the heat and mass transfer can be calculated.

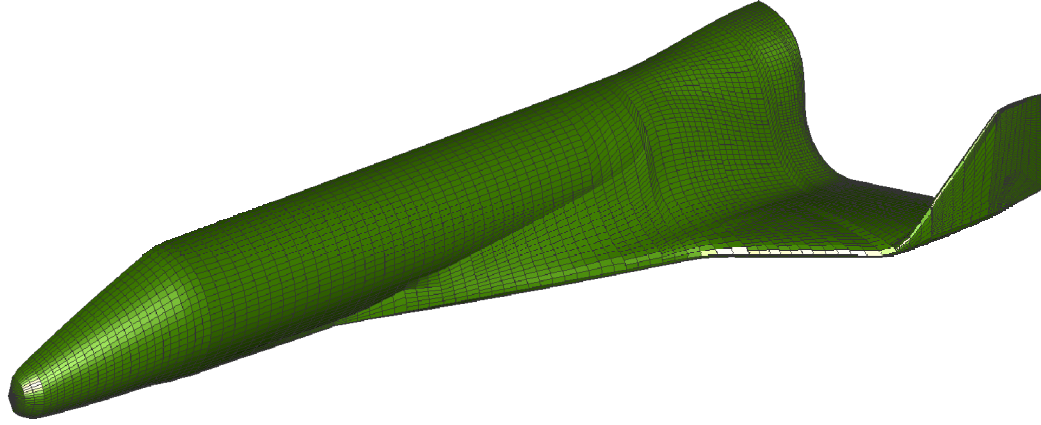


**Figure 3-1** – ATAC symmetric surface grid of the reusable booster concept.

ATAC performs inviscid streamline tracing using the following equation, known as “Newtonian approximation or the method of steepest descent” (Strobel, Tillman and King 9),

$$\mathbf{t} = \frac{d\mathbf{r}}{ds} = \frac{\partial \mathbf{r}}{\partial w} \frac{dw}{ds} + \frac{\partial \mathbf{r}}{\partial u} \frac{du}{ds} \quad (3-2)$$

Where  $\mathbf{t}$  is the streamline trace,  $\mathbf{r}$  is the position vector of some point on the body. These streamlines serve as the basis of all future calculations.

The calculation of pressure distribution along the body can be solved by any of the three choices: Dahm-Love pressure correlations, Newtonian pressure, or modified Newtonian pressure. The Dahm-Love correlations are “an empirical extension and synthesis of the modified Newtonian correlation, valid for spheres, but including a correlation for flat faced cylinders” (Strobel, Tillman and King 11). The Newtonian method for approximating surface pressure is calculated via the following equations:

$$C_p = C_p^* \cos^2 \eta \quad (3-3)$$

where  $\eta$  is the angle between the wind vector and the outward surface normal.  $C_p^*$  is calculated by

$$C_p^* = \frac{\left(\frac{p_{t_2}}{p_\infty}\right) - 1}{\left(\frac{\gamma}{2}\right) M_\infty^2}; \quad M_\infty < 1 \quad (3-4)$$

$$C_p^* = \frac{\left(1 + \frac{\gamma-1}{2} M_\infty^2\right)^{\frac{\gamma}{\gamma-1}} - 1}{\left(\frac{\gamma}{2}\right) M_\infty^2}; \quad M_\infty > 1 \quad (3-5)$$

Likewise, the modified Newtonian pressure is augmented with a function of the angle between the wind vector and the outward surface normal,  $\eta$  and the Mach number,  $M$ .

$$C_p = C_p^* \cos^2 \eta + F(\eta, M) \quad (3-6)$$

where

$$F(\gamma, M) = \left[-0.78 M_\infty^{-2.27} \cos \eta - 0.95 e^{-2.235(M_\infty-1)}\right] \sin \eta \quad (3-7)$$

Equation (3-7) was “modified using the empirical function of Andrews for low supersonic and high subsonic flight” (Strobel, Tillman and King 15). This relationship applies to sharp cone geometries.

The surface temperature and heat flux are calculated using the Momentum/Energy Integral Technique (MEIT). The ATAC manual says the MEIT is “applicable to continuum flows and to non-separated boundary layer conditions” (Strobel, Tillman and King 18). The following three equations are solved simultaneously in the MEIT procedure. The integral momentum equation,

$$\begin{aligned} \frac{1}{r \rho_e u_e (h_{t,e} - h_w)} \frac{d}{ds} (r \rho_e u_e (h_{t,e} - h_w) \Phi) \\ = C_h \frac{h_r - h_w}{h_{t,e} - h_w} + \frac{(\rho v)_w (h_{t,i,w} - h_w)}{\rho_e u_e (h_{t,e} - h_w)} \end{aligned} \quad (3-8)$$

The integral energy equation,

$$\frac{1}{r \rho_e u_e^2} \frac{d}{ds} (r \rho_e u_e^2 \Theta) = \frac{C_f}{2} + \frac{(\rho v)_w u_{i,w}}{\rho_e u_e^2} + \frac{H \Theta}{\rho_e u_e^2} \frac{dp}{ds} \quad (3-9)$$

And the entrainment relation,

$$\rho_{\infty} u_{\infty} \bar{y}^2 = 2rF\mu_e Re_{\theta} - 2 \int_0^{\infty} r(pv)_w ds \quad (3-10)$$

where

$$\Theta = \text{Boundary layer momentum thickness, } \int_0^{\infty} \frac{\rho u}{\rho_e u_e} \left( \frac{u_i - u}{u_e} \right) dy$$

$$\frac{C_f}{2} = \text{Friction factor, } \frac{\tau_w}{\rho_e u_e^2}$$

$$\tau_w = \text{Wall shear}$$

$$H = \text{Shape factor, } \frac{\delta^*}{\theta}$$

$$\delta^* = \text{Boundary layer displacement thickness, } \int_0^{\infty} \left( 1 - \frac{\rho u}{\rho_i u_i} \right) dy$$

$$h_t = \text{Total enthalpy}$$

$$h_w = \text{Wall enthalpy}$$

$$h_r = \text{Recovery enthalpy}$$

$$\Phi = \text{Boundary layer energy thickness, } \int_0^{\infty} \frac{\rho u}{\rho_e u_e} \left( \frac{h_{t,i} - h_t}{h_{t,e} - h_w} \right) dy$$

$$C_h = \text{Stanton number, } \frac{\dot{q}_w}{\rho_e u_e (h_r - h_w)}$$

$$\dot{q}_w = \text{Wall heat flux}$$

$$\bar{y} = \text{Shock radial location through which the boundary layer edge streamline has passed}$$

$$F = \text{Entrainment shape factor, } \frac{\delta - \delta^*}{\theta}$$

$$\delta^* = \text{Displacement thickness based on edge properties}$$

$$\delta = \text{Boundary layer thickness}$$

$$\mu = \text{Viscosity}$$

$$Re_{\Theta} = \text{Momentum thickness Reynolds number, } \frac{\rho_e u_e \Theta}{\mu_e}$$

And the subscripts are:

- $w$  = Wall
- $e$  = Boundary layer edge
- $i, w$  = Properties obtained through an isentropic expansion from the stagnation point to the location pressure

The following excerpt from the ATAC manual describes each equation's purpose towards the solution:

The momentum equation solution dictates the boundary layer parameters upon which the following phenomena are based: transition onset and location, transitional intermittency, surface roughness effects, and turbulent boundary layer shape factors. The energy equation solution dictates the convective heat transfer subject to the four parameters above. The boundary layer parameter, which dictates convective mass transfer, is not evaluated. Rather, mass transfer is determined by analogy to the energy boundary layer solution. The entrainment relation, Equation (3-10), provides a means of determining the boundary layer properties, which are essential boundary conditions for the solution of Equations (3-8) and (3-9). The boundary layer edge thermodynamic state is determined by lookup on pressure and entropy in a real-gas Mollier table. Pressure is known from the inviscid flow solution, and entropy is calculated from consideration of the bow shock shape and boundary layer mass entrainment. (Strobel, Tillman and King 19)

These empirical correlations that compute pressure break down at high angles of attack and large amounts of separation, such as on sharp leeward angles. Due to the rocket-back maneuver and the high angles of attack during re-entry, these empirical relationships become questionable during a large portion of the flight regime. According to the ATAC manual, "since the methodology does not allow for separation or flow across streamlines, the accuracy at these large angles [of attack] are questionable, especially on the leeward side" (Strobel, Tillman and King 9).

A method capable of calculating at high angles of attack is to use a Navier-Stokes based CFD code that has a means of directly modeling eddies and a method of calculating turbulence transition location and intensity. As stated previously, the ultimate method is transient, fully coupled CFD, but this method requires more time than is feasible for any practical problem. Thus, we employ steady state Navier-Stokes CFD.



## **Steady-State Navier-Stokes Computational Fluid Dynamics**

If cost and time were not relevant constraints in an engineering problem then by far, the best way to solve the transient heat transfer problem for a thermal protection system would be using a fully coupled, transient, conjugate heat transfer analysis. Several problems arise with this utopian approach. First, the grid size is extremely large because the internal geometry must now be modeled, including the thickness of all solids as well as the fluid in the internal bays. Secondly, the time-steps must be extremely small, on the order of  $10^{-6}$  seconds, for the stability of the transient Navier-Stokes Equations. Third, the wall clock time required for such small time steps over a seven minute flight is immense. The Department of Defense's (DoD) high performance computing center has a maximum allowable wall clock time of two weeks, which is insufficient for the TPS problem at hand. To get around the DoD wall clock time limitation, an attempt was made to run a sequence of transient analyses by restarting the computation on a test model every two weeks. Restarting the transient problem proved to cause numerical divergence, rendering this "fix" useless. Coupling the above problems, we can see that performing a transient, conjugate heat transfer analysis is not possible with current computer technology. Thus, we seek a set of steady-state solutions generated by a Navier-Stokes CFD code as an effective engineering solution to the real world computational limitations.

Steady state Navier-Stokes CFD, by definition, does not include transient effects in the flow-field. These transient phenomena may include vortex shedding, an undeveloped boundary layer, or movement of the shock layer, and can have an effect on the temperature distribution along the wall of the vehicle. The surface temperatures of the vehicle are dominated by both the conversion of the flow's kinetic energy to a temperature rise at the leading edges and the viscous shearing of the fluid along flow-parallel surfaces, not necessarily by transient effects.

It is quite common in the CFD community to use steady state or quasi-steady state analyses, it is based on the fact that “the flow-field adapts at a very fast rate to changes in the free stream conditions as the vehicle is accelerating. This is in contrast to the solid side temperature profile which gradually changes throughout the flight, never reaching steady state” (Fricker, Mendoza and Catton 4).

Commercial CFD, with readily available computational resources, is capable of carrying out the steady state analysis. Ansys Fluent uses the full set of Navier-Stokes Equations, which are comprised of the Continuity, Momentum, and Energy Equations. The continuity equation is solved in the following form (Ansys, Inc. 27):

$$\frac{\partial \rho}{\partial t} + \nabla \cdot (\rho \mathbf{v}) = S_m \quad (3-11)$$

The source mass  $S_m$  is 0 for this application. The momentum equation is given in general form (Ansys, Inc. 28):

$$\frac{\partial}{\partial t}(\rho \mathbf{v}) + \nabla \cdot (\rho \mathbf{v} \mathbf{v}) = -\nabla p + \nabla \cdot \bar{\bar{\tau}} + \rho \mathbf{g} + \mathbf{F} \quad (3-12)$$

where  $p$  is the static pressure,  $\bar{\bar{\tau}}$  is the stress tensor,  $\rho \mathbf{g}$  is the gravitational body force, and  $\mathbf{F}$  is the external body force. The last two terms in Equation (3-12) are negligible. “The stress tensor is given by:

$$\bar{\bar{\tau}} = \mu \left[ (\nabla \mathbf{v} + \nabla \mathbf{v}^T) - \frac{2}{3} \nabla \cdot \mathbf{v} I \right] \quad (3-13)$$

where  $\mu$  is the viscosity,  $I$  is the unit tensor, and  $\nabla \mathbf{v} + \nabla \mathbf{v}^T$  is the effect of volume dilation” (Ansys, Inc. 28). The energy equation is modeled in Ansys Fluent “using the concept of the Reynolds’ analogy to turbulent momentum transfer. The ‘modeled’ energy equation is as follows” (Ansys, Inc. 111):

$$\frac{\partial}{\partial t}(\rho E) + \frac{\partial}{\partial x_i} [u_i(\rho E + p)] = \frac{\partial}{\partial x_j} \left[ \left( k + \frac{C_p \mu_t}{Pr_t} \right) \frac{\partial T}{\partial x_j} + u_i(\tau_{ij})_{\text{eff}} \right] + S_h \quad (3-14)$$

where  $S_h$  is the source term and the subscript “eff” means effective. The thermal conductivity is  $k$ ,  $E$  is the total energy, and  $(\tau_{ij})_{\text{eff}}$  is the deviatoric stress tensor, given by (Ansys, Inc. 111):

$$(\tau_{ij})_{\text{eff}} = \mu_{\text{eff}} \left( \frac{\partial u_j}{\partial x_i} + \frac{\partial u_i}{\partial x_j} \right) - \frac{2}{3} \mu_{\text{eff}} \frac{\partial u_k}{\partial x_k} \delta_{ij} \quad (3-15)$$

Fluent has a variety of turbulence models, from the one-equation Spalart-Allmaras to the seven-equation Reynold’s Stress model. For this application, the Transition SST model was chosen. Only two transition models are available in Ansys Fluent: Transition SST and Reynolds Stress. The Reynolds Stress model has seven equations, more than what is being solve for the general flow-field. In order to produce more rapid results, the transition model with fewer equations was chosen.

This Transition SST model is “based on the coupling of the SST  $k - \omega$  transport equations with two other transport equations, one for the intermittency and one for the transition onset criteria, in terms of momentum-thickness Reynolds number” (Ansys, Inc. 142). According to White, “there is no fundamental theory of transition, but there are experiments and correlations which try to predict the final onset of fully turbulent flow, such as  $Re_{x,tr}$  or  $Re_{\theta,tr}$ , as a function of the following parameters: pressure gradient, free-stream turbulence, wall roughness, mach number, wall suction or blowing, and wall heating or cooling” (White 378). The model used by Ansys uses an empirical correlation by Langtry and Menter “which covers standard bypass transition as well as flows in low free-stream turbulence environments” (Ansys, Inc. 142).

The solution method employed in this thesis uses steady state CFD solutions to predict heat transfer coefficients that are shown to be only weakly dependent on wall temperature. Thus, transient effects are neglected. Standard calculation of heat transfer coefficients, in the form of the following equation,

$$h_r = \frac{q}{T_w - T} \quad (3-16)$$

require knowledge of the actual wall temperature  $T_w$  in transient flight, as well as data extraction from the edge of the boundary layer for the temperature at that location. Unfortunately, the wall temperature is unknown *a priori*, as we are not performing a transient calculation. In addition, in regions of highly separated, re-circulating flow, such as the back of the vehicle when the vehicle flies at angles of attack up to 90°, there is a question as to where the edge of the boundary layer data should be extracted. An alternate method to predicting standard heat transfer coefficients is to use one based on recovery temperature

The recovery temperature is shown in Chapter 4 to be only weakly dependent on wall temperature. Therefore, a simple steady state analysis can be generated, the recovery temperature calculated, and a heat transfer coefficient then generated for use in subsequent analyses. The workflow follows this sequence:

1. Generate steady state CFD results at each time-step using a re-radiating, adiabatic wall, also known as radiation equilibrium wall temperature (REWT).
2. Export the results in Tecplot format. This format is text based lists the x, y, and z coordinates, then any desired data in the additional columns. The data being exported is:
  - a. Far-field temperature
  - b. Far-field mach number
  - c. Wall temperature
  - d. Heat flux
  - e. Effective Prandtl number. This number includes the turbulence effects and Fluent calculates this number by the effective thermal conductivity and effective viscosity, which also account for the turbulent effects.

3. Use a Matlab code specifically written for this procedure to import the Tecplot results and calculate the recovery temperature at each point. This code uses the heat flux, wall temperature, and Prandtl number at each element on the wall.
4. Export the results in a comma delimited format for use with the ABAQUS FEA heat transfer analysis

Before the applied heat transfer analysis can be performed on the full three-dimensional geometry, the dependency of the heat transfer coefficient with respect to wall temperature needs to be quantified. This dependency needs to be quantified in order to validate the decoupled approach to the solution of the transient TPS temperature profile. For this process of quantification, a simplified, two-dimensional case is chosen for reduced computation time and less complexity in code.

## CHAPTER 4

### QUANTIFYING THE DEPENDENCY OF THE HEAT TRANSFER COEFFICIENT WITH RESPECT TO WALL TEMPERATURE

#### **Weakly Dependent Heat Transfer Coefficient**

The recovery temperature based heat transfer coefficient is only weakly dependent on wall temperature because it accounts for the kinetic energy of the incoming flow. Thus, having calculated the heat transfer coefficient for one case, the wall temperature need not be known for the other cases; furthermore, the heat transfer coefficient can then be applied to a transient heat transfer analysis on a thermal protection system and the transient temperature profile can be produced with a higher degree of confidence. The data presented in this chapter will show that the recovery temperature based heat transfer coefficient is weakly dependent on wall temperature for a wide range of flight conditions.

#### **The Wing Model**

A simple two-dimensional model of a wing provides the geometry for the variability quantification analysis. Figure 1-1 depicts the geometry, which is a NACA 23012 airfoil. The two-dimensional model was chosen in order to simplify any quantification of the variation in heat transfer coefficient with respect to wall temperature and to neglect any three-dimensional flow dissimilarities. Additionally, solution time is massively reduced, as the grid size is cut by several orders of magnitude: the three-dimensional grid used later in this

research has 26,245,437 elements and 6,083,498 nodes while the two-dimensional grid of the wing has only 44,550 elements and 44,880 nodes.

The grid spacing in the direction normal to the surface had to be created small enough near the wall in order to capture the velocity gradient in the boundary layer. The grid spacing is then expanded exponentially to the far-field domain, which is 20 chord-lengths away. The expansion in grid spacing serves as a way to reduce mesh size in areas that steep gradients do not exist, such as beyond the boundary layer. Figure 4-1 shows the mesh near the wall.

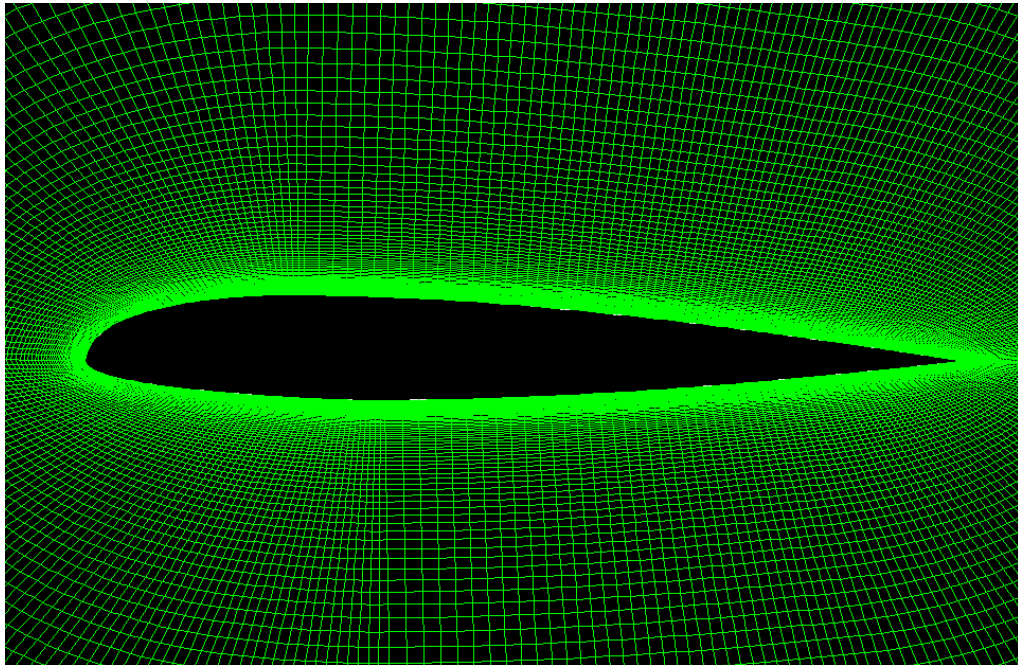


**Figure 4-1** – Grid of the NACA 23012 airfoil used in the two-dimensional wall temperature dependency analysis.

The grid statistics are as follows. The maximum aspect ratio is 161.6, which is high, but the short side of the cell is parallel to the direction of high temperature and velocity gradients in the boundary layer and the gradients along the long side are much less severe. Figure 4-2 shows an enlarged view of the area of high aspect ratio. The high aspect ratio is a result of the expansion layer used to resolve the velocity and temperature profiles in the

boundary layer. In order to reduce the aspect ratio, a large number of divisions in the direction parallel to the surface of the body would be necessary. This would greatly increase the cell count and therefore increase the time-to-solution.

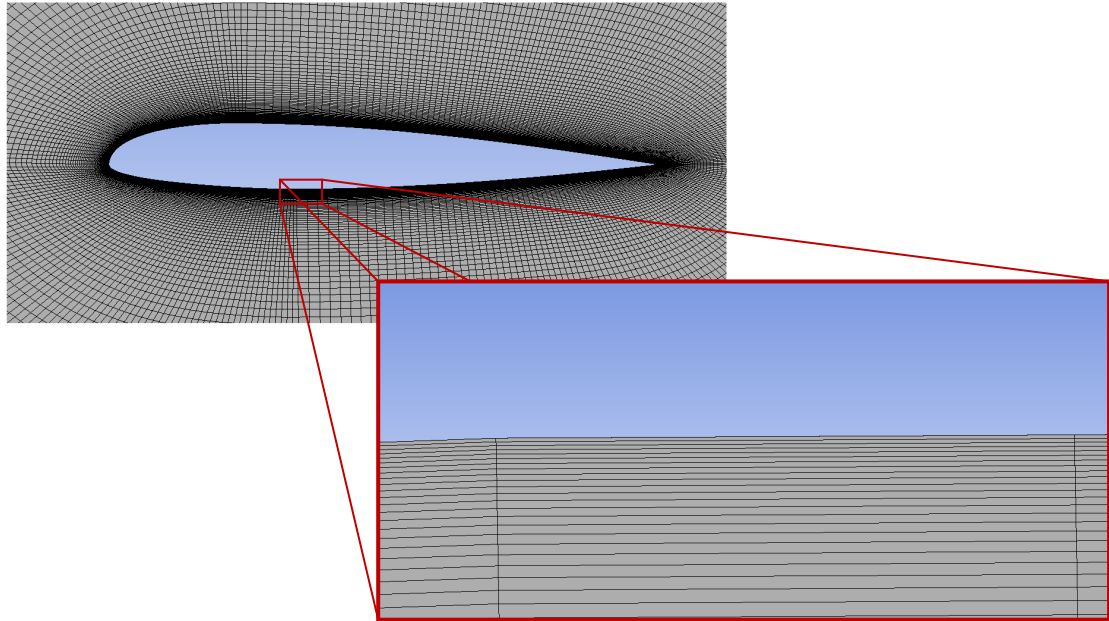


**Figure 4-2** – Enlarged view of high aspect ratio region.

The maximum cell skewness is 85.3%, well within the limit for a double precision solver.

Ansys calculates skewness via the following equation:

$$Skewness = \max\left(\frac{\theta_{max} - \theta_e}{180 - \theta_e}, \frac{\theta_e - \theta_{min}}{\theta_e}\right)$$

where  $\theta_e$  is the equiangular face or cell, which is  $60^\circ$  for tetrahedrons and triangles and  $90^\circ$  for quadrilaterals and hexahedrons. Figure 4-3 depicts  $\theta_{max}$  and  $\theta_{min}$ .

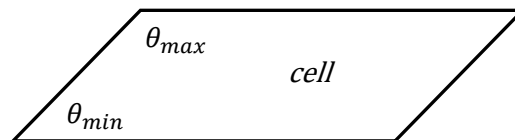


**Figure 4-3** – Graphic of  $\theta_{max}$  and  $\theta_{min}$ .



The maximum skewness occurs near the trailing edge of the airfoil and exists in the boundary layer. Because the grid is structured, the skewness is a result of the steep change in curvature of the trailing edge of the airfoil versus the gradual change in curvature of the opposing boundary.

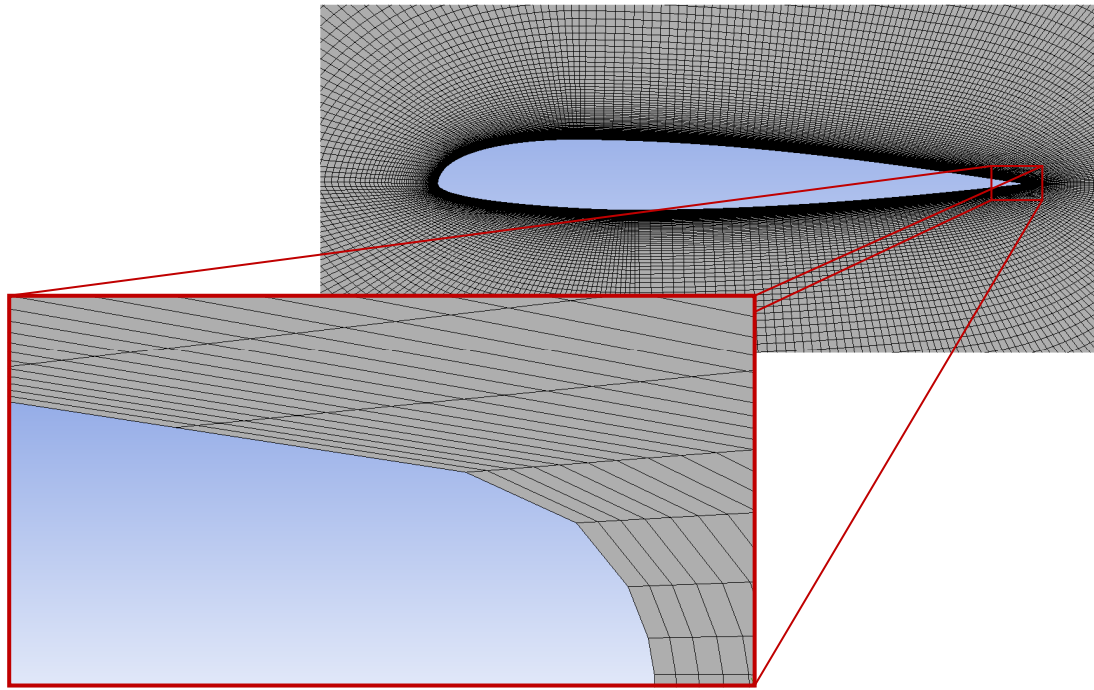


**Figure 4-4** – Enlarged view of the region with the highest skewness.

The full set of Navier-Stokes equations is modeled; these equations appear in the previous chapter as Equations (3-11) through (3-15). The turbulence model, Transition SST, is discussed in Chapter 3. It is a four-equation turbulence model that uses the  $k - \omega$  transport equations and an Ansys proprietary transition model derived from empirical curve fits. Air is modeled as an ideal gas. The specific heat  $c_p$  is described by a piecewise-polynomial with two ranges and eight coefficients, a built-in Fluent model. Table 4-1 summarizes the piecewise-polynomial coefficients for each range. The model for thermal conductivity and viscosity is kinetic theory.

**Table 4-1** – Ranges and coefficient values for the piecewise polynomial model of specific heat  $C_p$ .

Range 1: 100 K < T < 1000 K								
Coefficient #	1	2	3	4	5	6	7	8
Value	1161	-2.369	0.01486	-5.035E-5	9.929E-8	-1.11E-10	6.54E-14	-1.57E-17
Range 2: 1000 K < T < 3000 K								
Coefficient #	1	2	3	4	5	6	7	8
Value	-7070	33.71	-0.058	5.422E-5	-2.337E-8	9.24E-12	-1.57E-15	1.11E-19

There are several boundary conditions that were chosen to bound the weak dependence problem. For Study A, Table 4-2 lists the various boundary conditions. These boundary conditions were chosen to represent the flight trajectory of the applied problem described in Chapter 5. The boundary conditions listed in Table 4-1 compare isothermal walls with walls that have a temperature gradient: the REWT wall, the Ti-6-4 wall, and the Inconel-617 wall. The Ti-6-4 wall is the titanium 6-aluminum 4-vanadium alloy with a wall thickness of 0.125 *in*. Ti-6-4 properties are a density,  $\rho$ , of  $4430 \frac{kg}{m^3}$ , a specific heat capacity,  $C_p$ , of  $526 \frac{J}{kg-K}$ , and a thermal conductivity,  $k$ , of  $6.7 \frac{W}{m-K}$  (Matweb, LLC.). The Inconel-617 wall is the Special Metals® Alloy 617 with a wall thickness of 0.125 *in*. The material properties are a density,  $\rho$ , of  $8360 \frac{kg}{m^3}$ , a specific heat capacity,  $C_p$ , of  $419 \frac{J}{kg-K}$ , and a thermal conductivity,  $k$ , of  $13.6 \frac{W}{m-K}$  (Matweb, LLC.). Both of these metals are typical structural alloys used in high speed aircraft.

**Table 4-2** – Boundary conditions for CFD jobs used in Study A of quantifying the variation in the weak dependence assumption.

BOUNDARY CONDITIONS – STUDY A			
Angle of Attack, $\alpha$ (°)	Wall	Emissivity	Mach Number
0	200 K	0.8	2
15	600 K	0.9	5
45	1000 K		
90	REWT		
	Ti-6-4		
	Inconel-617		

The boundary conditions listed in Table 4-2 are combined to produce 72 unique CFD runs for Study A, after removing duplicate boundary conditions. Table B-1 in Appendix B contains a table of all the various boundary conditions for each job code. In addition to these boundary condition, a constant altitude of 30 *km* is used, which results in  $P_\infty = 1172 \text{ Pa}$  and  $T_\infty = 226.65 \text{ K}$  using the 1976 U.S. Standard Atmosphere.

In addition to Study A, which compares isothermal walls to radiation adiabatic walls, there is a separate study, Study B, which measures the dependency of the heat transfer coefficient with respect to wall temperature, using isothermal wall boundary conditions only. In this case, the boundary conditions are varied only at the wall. There are no changes to Mach number or angle of attack. The same altitude of 30 *km* is used, again resulting in  $P_\infty = 1172 \text{ Pa}$  and  $T_\infty = 226.65 \text{ K}$  using the 1976 U.S. Standard Atmosphere. The Mach number is 5 and the thermal boundary conditions at the wall were varied from 200 K to 1000 K in 100 K increments, resulting in 9 unique analyses.

For all the analyses reported in this technical document, the pressure far-field turbulent intensity is set to 0.01% and the turbulent viscosity ratio is set to 10. Roy and Blottner investigated several turbulence models, including a Wilcox  $k - \omega$  model, which is the basis for the Ansys  $k - \omega$  model (Ansys, Inc. 126). Part of Roy and Blottner’s investigation included a sensitivity analysis of Wilcox’s  $k - \omega$  turbulence model to free-

stream turbulence levels as well as free-stream turbulence viscosity ratios on a Mach 8 sharp cone. Figure 4-5 shows the heat flux as a function of distance along the cone for each case. Table 4-3 summarizes the variations in viscosity ratio and level of intensity in all the different cases.

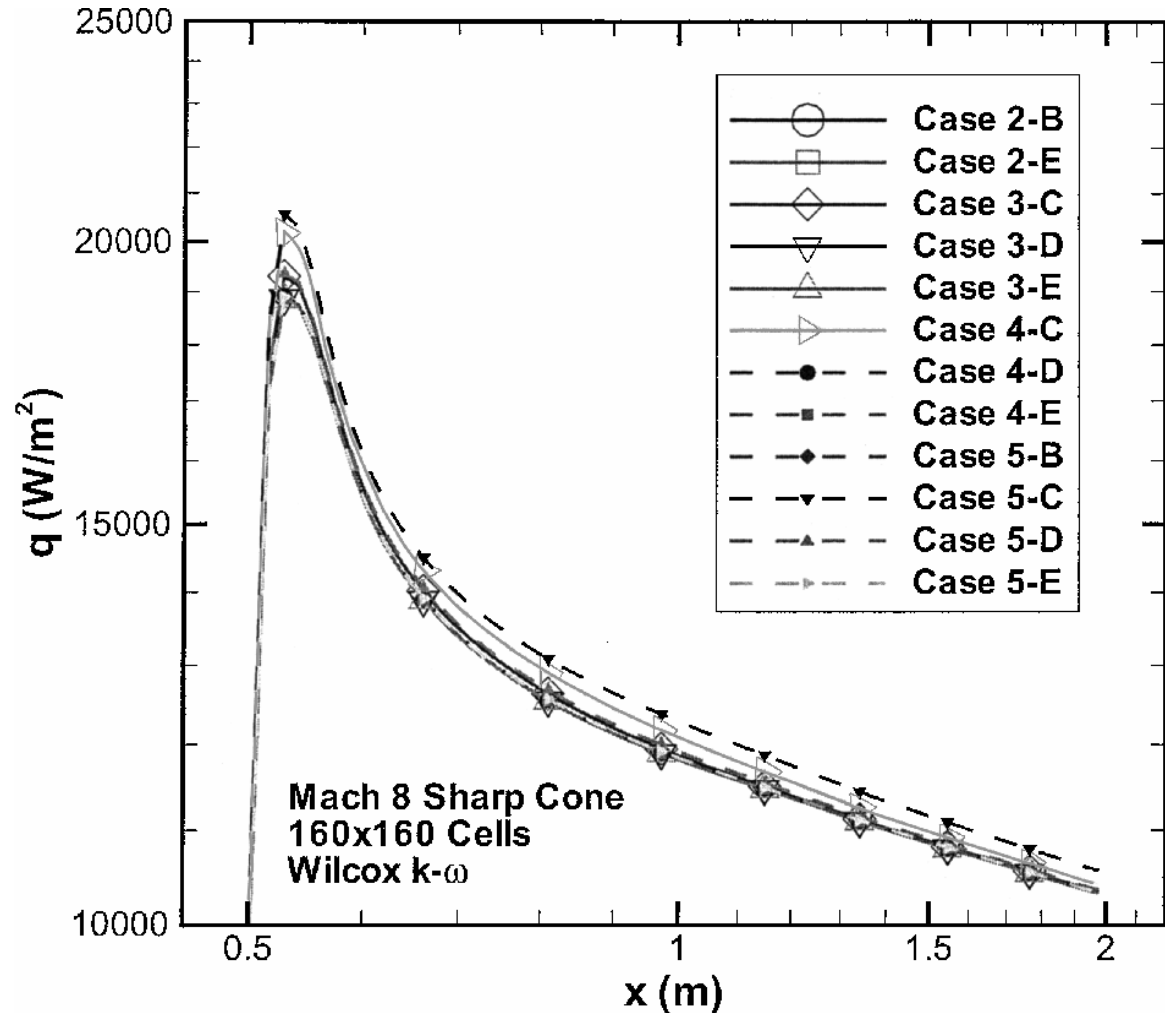


**Figure 4-5** – Sensitivity of the Wilcox  $k - \omega$  turbulence model to the free-stream turbulence levels for the Mach 8 sharp cone (Roy and Blottner 321).

**Table 4-3** – Summary of the cases studied in Figure 4-5, showing the variations in free-stream turbulent viscosity ratio and turbulence intensity. ✓ denotes a case that was run (Roy and Blottner 321).

Case	$\mu_t/\mu$	$T_u, \%$				
		A	B	C	D	E
		0.001	0.01	0.1	1.0	10.0
1	$1 \times 10^{-5}$					
2	0.001		✓			✓
3	0.1			✓	✓	✓
4	1.0			✓	✓	✓
5	10.0		✓	✓	✓	✓

The solution methods are comprised of an implicit formulation and an Advection Upstream Splitting Method (AUSM) flux type. The AUSM flux type is more robust for problems with shock waves: according to Blazek, the “advantage can be seen in only a moderately increased numerical effort but a much better resolution of shocks and boundary layers, as compared to the central scheme with scalar artificial dissipation” (Blazek 101). Blazek also states that “AUSM proved to deliver a crisp resolution of strong shocks and accurate results for boundary layers” (Blazek 105). The other option for flux type is Roe’s Forward Difference Scheme, which has disadvantages with chemically reacting flows (Blazek 110). Although in this study the flow never gets hot enough to chemically react, AUSM was chosen for its greater range.

The method of discretization and evaluation of the gradient is Green-Gauss cell based gradient computation. This is used because it is slightly faster than a least-squares approach: for Green-Gauss cell based gradient calculation “no additional data structures are needed for the reconstruction of gradients” (Blazek 164). The flow discretization is second order upwind, but the turbulent kinetic energy, specific dissipation rate, and intermittency are all discretized by the first order upwind method.

The solutions were judged as converged when the integrated total surface heat rate stopped changing after three significant figures from one iteration to the next. It was

observed that the integrated total heat rate was the last metric to converge; often, mass, momentum, and energy had converged to six significant figures before the heat flux converged to three significant figures. Figure 4-6 provides as a sample graph of the residuals versus iteration number.

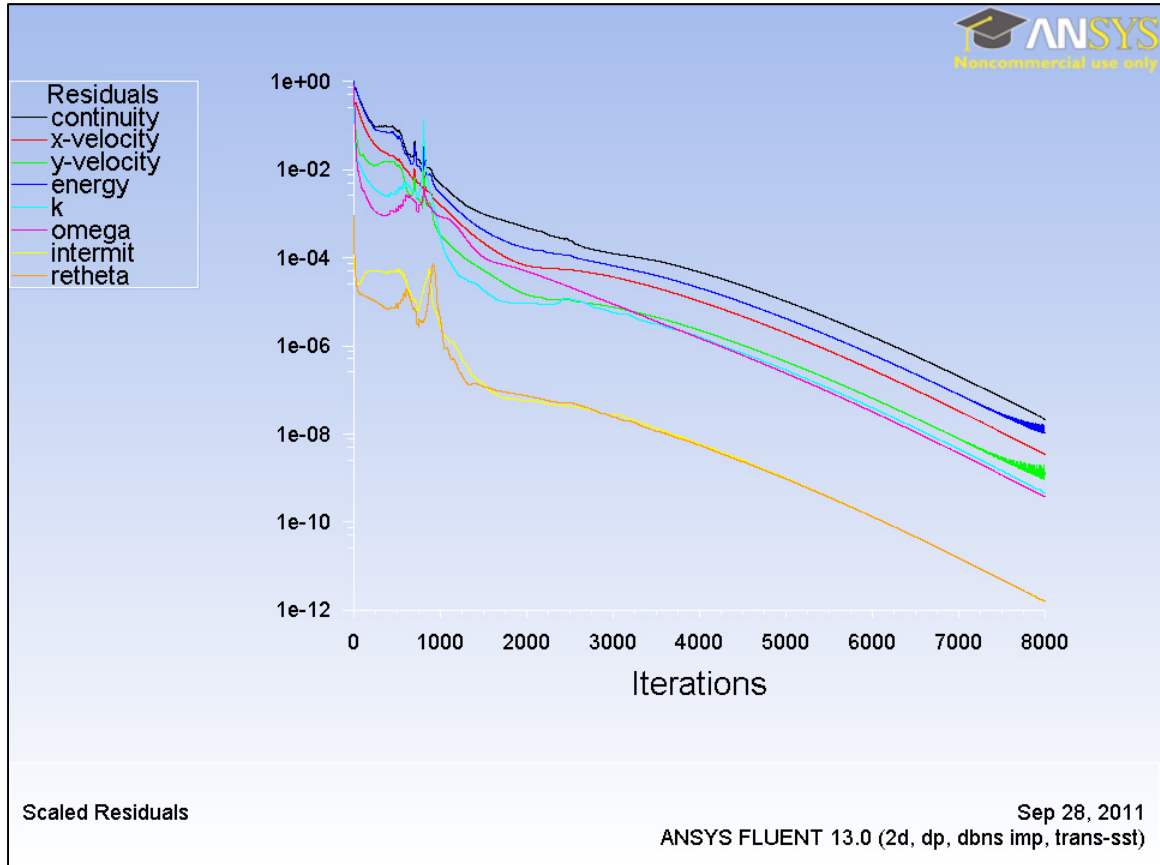


**Figure 4-6** – Example of residuals versus iteration number. “Intermit” and “retheta” are turbulence parameters for turbulence intermittency and  $Re_\theta$ .

### Grid Convergence Study

A grid convergence study is necessary to ensure that the results are independent of the mesh. Examples of parameters that are highly dependent on the mesh are shock location and structure, resolution of the boundary layer, and turbulence intensity. A grid convergence study is conducted on the standard mesh, a once refined mesh, and a twice refined mesh. The once refined mesh cuts each quad of the standard mesh into four quads

and the twice refined mesh cuts each quad on the once refined mesh into 16 quads. Table 4-4 summarizes the meshes and their sizes.

Table 4-4 – Summary of the grids used in the grid convergence study.

<b>Mesh</b>	<b>Nodes</b>	<b>Elements</b>	<b>Nodes Along the Wall</b>
Standard	44,880	44,550	330
Once Refined	178,860	178,200	660
Twice Refined	714,120	712,800	1,320

The standard grid proved to have sufficient resolution; Figure 4-7 shows the wall temperature as a function of path length, which is distance along the surface of the wall, and focuses on the region near the leading edge, where the peak temperature occurs. The leading edge is a region of interest. This graphic shows that the answer changes only a small quantity when the grid is refined by a factor of four. For example, the predicted peak temperature on the coarsest grid is approximately 1.5% lower than the predicted peak temperature of the finest grid. Figure 4-8 shows the temperature profile of the entire wing. In this plot, we observe that all three temperature curves along the wall of the vehicle look nearly identical, except at the trailing edge.

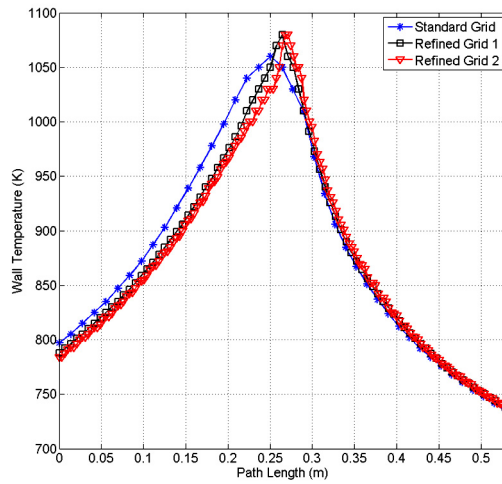


**Figure 4-7** – Wall temperature as a function of path length for each grid, zoomed on the leading edge.

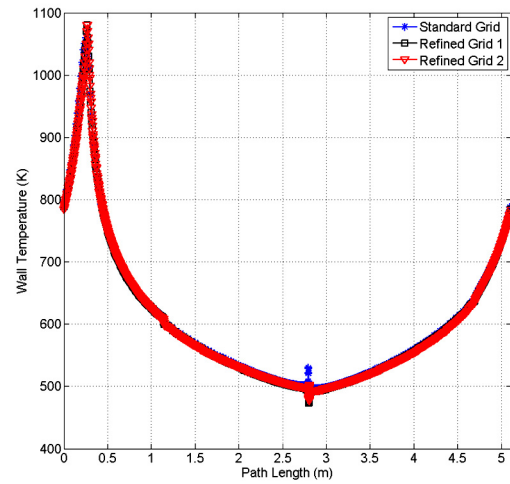


**Figure 4-8** – Wall temperature as a function of path length for each grid for the entire surface of the airfoil.

There is some discrepancy in predicted temperatures at the trailing edge, approximately 2.75m path length. This is due to a small amount of turbulent eddying present, as shown in Figure 4-9, as well as the expansion wave that occurs. Because the heat fluxes on this part of the vehicle are low, the answer in this region is not significant from a TPS or wing design perspective.



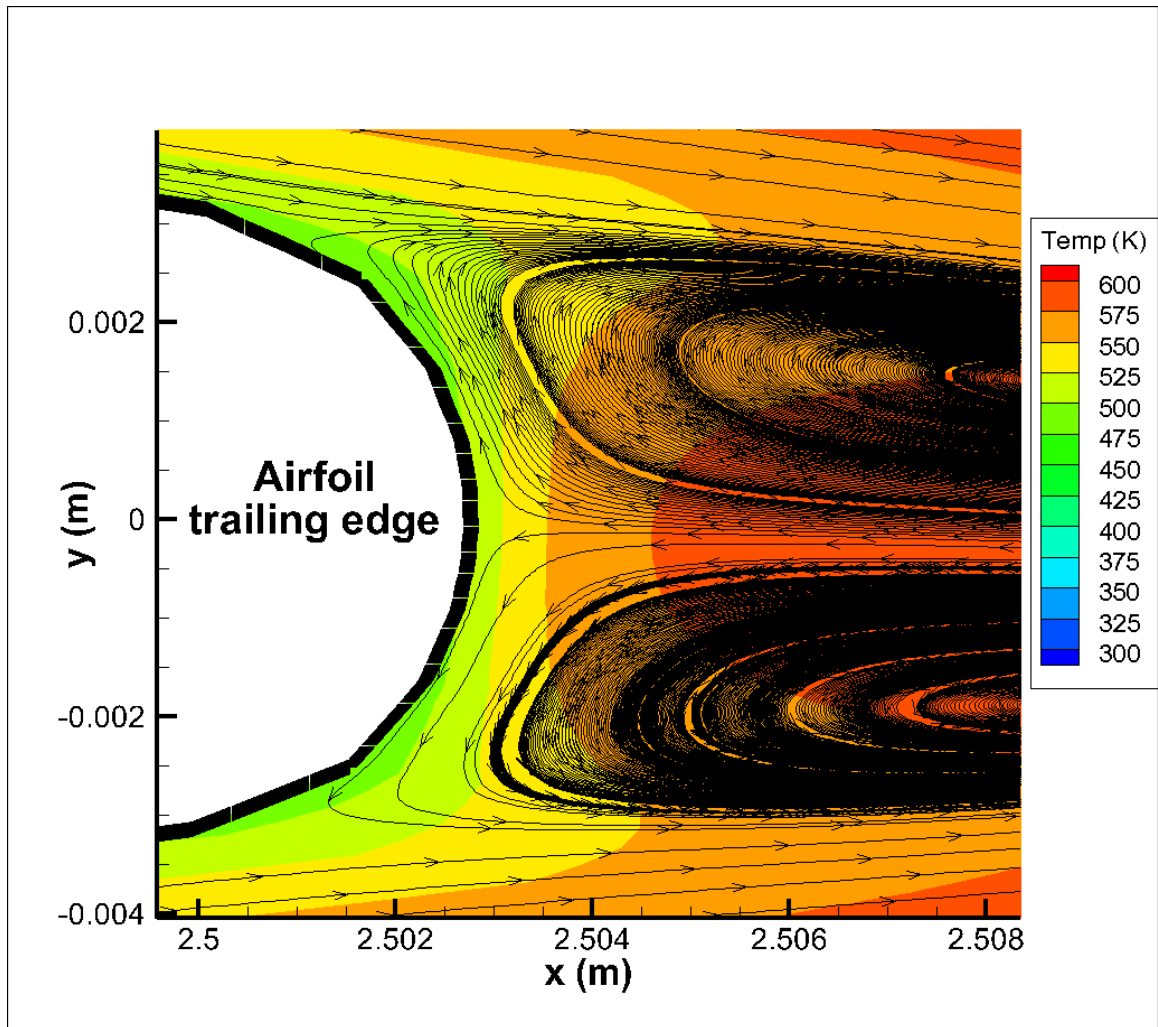


**Figure 4-9** – Enlarged view of the results near the trailing edge of the airfoil, depicting the recirculation zone. Note that the dual vortex pattern is seen only in a steady calculation: a transient calculation would show the vortices alternating and flowing downstream.

#### Quantifying the Wall Temperature Dependency in the Heat Transfer Coefficient

In study B, the nine analyses were created to study the effect of wall temperature on recovery temperature based heat transfer coefficient alone. These nine analyses consisted of isothermal boundary conditions at the wall, starting from 200 *K*, in 100 *K* increments, up to 1000 *K*. The results were exported in a delimited format from Fluent and brought into a simple Excel spreadsheet. Recovery temperature was calculated by Equation (2-45) and the

recovery factor was calculated by Equation (2-48). The Prandtl number used was the effective Prandtl number, which combines both the laminar and turbulent Prandtl numbers.

The data had to be plotted in a useful order. For example, plotting wall temperature versus x-location on the grid is senseless because the plot would reflect the upper surface, then the lower surface, then the upper, or some combination thereof. Essentially, plotting data vs. x-location does not discriminate what surface of the airfoil the data lays (such as the upper or lower surface). The following method was used to prepare the data for plotting:

1. Import the data into an Excel spreadsheet
2. Find the geometric center of the grid by using the following equation:

$$x_{loc} = \frac{\max(x) + \min(x)}{2} \quad (4-1)$$

$$y_{loc} = \frac{\max(y) + \min(y)}{2} \quad (4-2)$$

where  $x$  and  $y$  are the  $x$  and  $y$  coordinates of the nodes along the wall.

3. Calculate the angle of each node with the positive horizontal by the following equation:

$$\theta_i = \text{atan2}(x_i - x_{loc}, y_i - y_{loc}) \quad (4-3)$$

where  $i$  goes from 1 to the number of nodes along the wall and  $\text{atan2}$  is the arctangent of the specific coordinate between  $-\pi$  and  $\pi$ .

4. Sort the data by the angle, from smallest to largest
5. Calculate the distance along path,  $s$ , by this equation:

$$s_i = \sqrt{(x_i - x_{i-1})^2 + (y_i - y_{i-1})^2} \quad (4-4)$$

at  $i = 1, s_1 = 0$ .

6. Calculate the total path  $\beta_i$ :

$$\beta_i = s_i + \beta_{i-1} \quad (4-5)$$

at  $i = 1$ ,  $\beta_1 = 0$ . The total path signifies the path length along the surface of the airfoil.

7. Plot the data versus total path.

For Study B, a metric was chosen to demonstrate the variability of the heat transfer coefficient as a function of wall temperature and nondimensionalized heat flux. At each element along the wall, the heat flux is nondimensionalized by calculating it's heat flux versus the element with the highest heat flux along the wall. This is simply  $\frac{Q_i}{Q_{max}}$  for each element. This result is plotted against variation in the heat transfer coefficient,  $\varepsilon_{h_r}$  from the mean. For this case, the mean is calculated as:

$$\bar{h}_r = \frac{1}{9} \sum_{i=1}^9 h_{r_i} \quad (4-6)$$

The variation is also calculated for each element along the wall. For example, at  $M = 5$  and  $\alpha = 0$ , let us say that the forward most element, the one at the leading edge, has the highest heat flux of all the elements along the wall. This element's  $\frac{Q}{Q_{max}} = 1$  and it is compared to each leading edge element for each wall boundary condition, from  $200\text{ K} \leq T_w \leq 1000\text{ K}$ . Figure 4-10 illustrates the results of Study B.

The results of Study B suggest a promising outlook for the use of a recovery temperature based heat transfer coefficient. We see here that in all cases except for the  $1000\text{ K}$  case, the elements above 5% of the maximum heat flux, or  $0.05 < \frac{Q}{Q_{max}} \leq 1$ , the variation in heat transfer coefficient is between -10% and 10%, or  $-10\% < \varepsilon_{h_r} < 10\%$ . At the highest heat flux element, the band in variation is much tighter:  $-3\% < \varepsilon_{h_r} < 2\%$  for  $\frac{Q}{Q_{max}} = 1$ . This means that for areas of concern to the TPS engineer, where the heat flux is high, the heat transfer coefficient is fairly independent of wall temperature. This result is

significant; without it, the computational method used in this research would be of minimal value to the TPS design engineer.

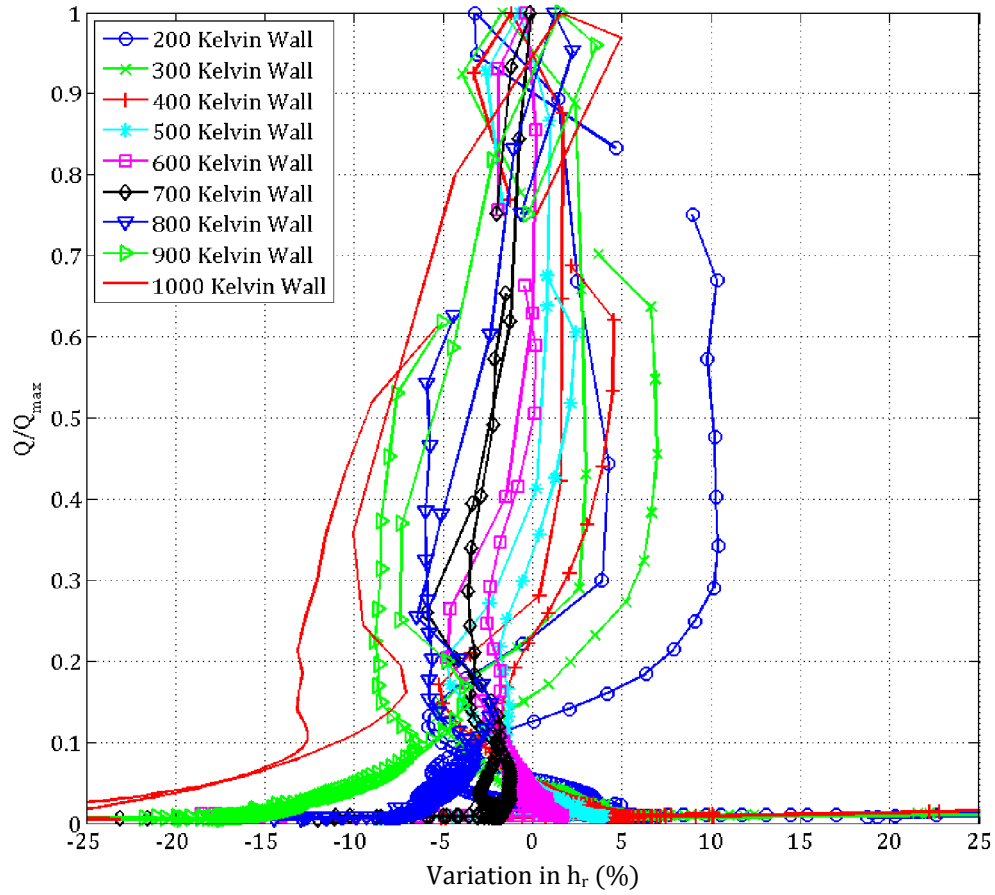


**Figure 4-10** – Comparison of  $\frac{Q}{Q_{max}}$  vs. variation in  $h_r$  for each isothermal boundary condition.

Clearly, the heat transfer coefficient become less trustworthy at the trailing edge of the vehicle, where a band in variation is observed to be  $-60\% < \varepsilon_{h_r} < 120\%$  but this is for  $0.003 < \frac{Q}{Q_{max}} < 0.032$ , elements that contribute almost no heat flux to the wall, which is illustrated in Figure 4-10. This larger difference is a result of the flow above and below the

airfoil coming back together, turbulent effects in the wake, and expansion waves; the flow physics are much more complex in this region.

A much different result in wall temperature dependence of the heat transfer coefficient is observed when a thermal gradient in the wall is introduced. Figure 4-10 is re-plotted to include a Radiation Equilibrium Wall Temperature (REWT) wall. It is profoundly evident that the heat transfer coefficient becomes sensitive to the thermal gradient in the wall, nearly linearly sensitive for  $\frac{Q}{Q_{max}} > 0.3$ , but still a good prediction for  $\frac{Q}{Q_{max}} = 1$ , where the variation in heat transfer coefficient is  $\pm 2\%$ , as seen in Figure 4-11.

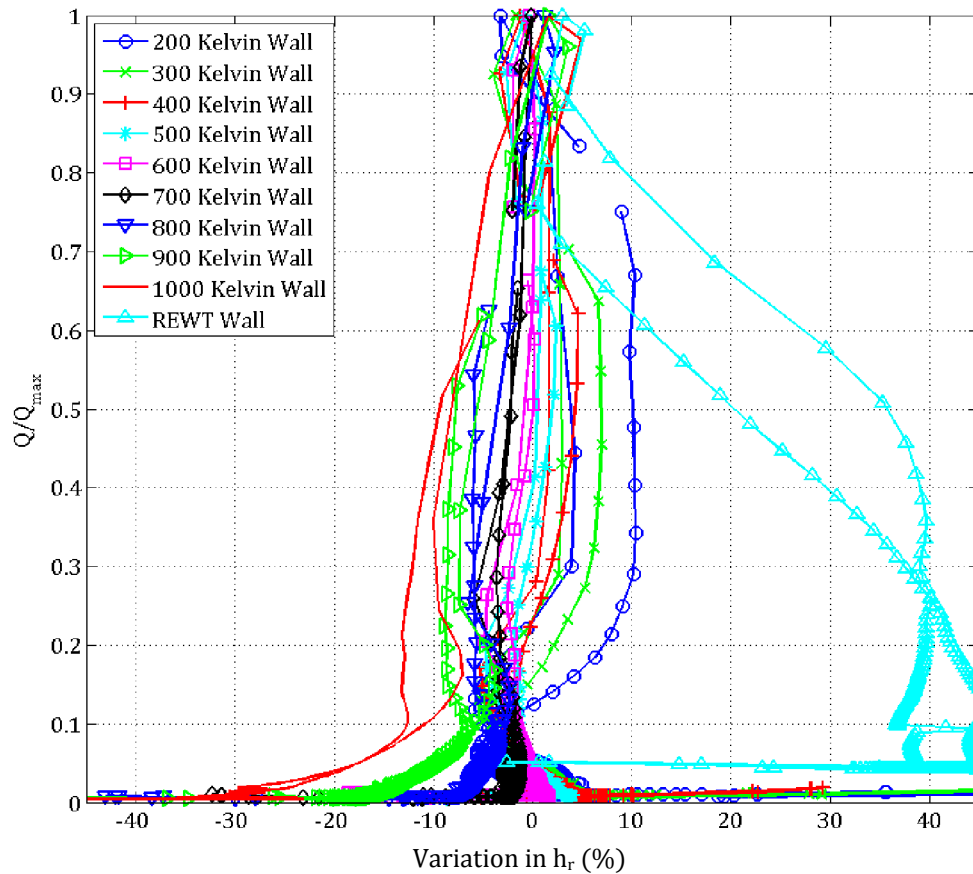


**Figure 4-11** – Comparison of  $\frac{Q}{Q_{max}}$  vs. variation in  $h_r$  for each isothermal boundary condition and one REWT boundary condition.

The 72 steady state analyses in Study A produced similar results to Study B. The walls with finite thickness and a material property, both Inconel-617 and Ti-6-4, appeared to have similar thermal characteristics as the REWT wall. That is, they had similar peak temperatures and thermal gradients. The variation in heat transfer coefficient as a function of path length along the surface of the wing have comparable curves for the similar boundary condition types for the majority of light conditions, except for the 90° case. The following set of figures, Figure 4-12 through Figure 4-16, show the percentage variation in heat transfer coefficient as a function of path length along the wall for some selected cases. They are grouped by Mach number and angle of attack; the remaining sets of plots which investigate the percentage variation in heat transfer coefficient versus path length for Study A are illustrated in Appendix A.

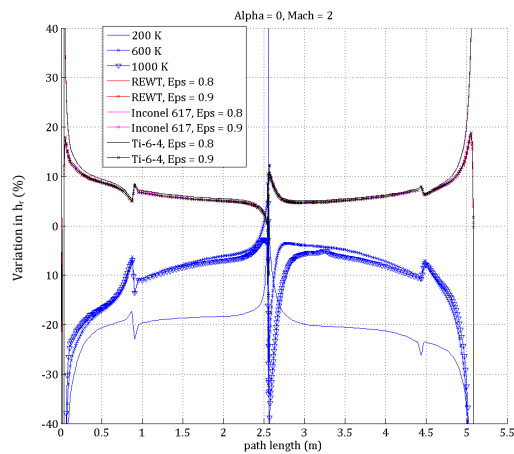


**Figure 4-12** –Comparison of % variation in recovery temperature based heat transfer coefficient as a function of path length along the surface of the wing for each 9 variations in wall boundary conditions at Mach 2 and  $\alpha = 0^\circ$ .

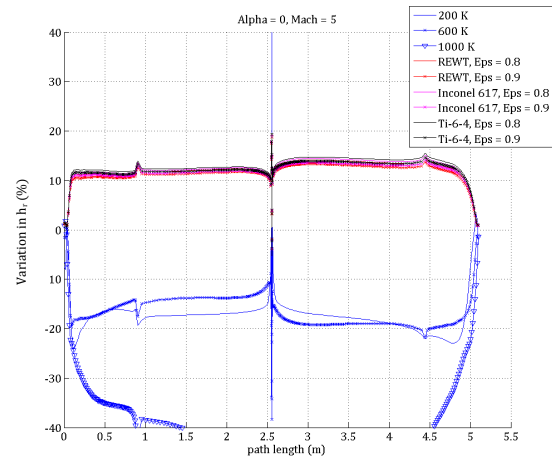


**Figure 4-13** – Comparison of % variation in recovery temperature based heat transfer coefficient as a function of path length along the surface of the wing for each 9 variations in wall boundary conditions at Mach 5 and  $\alpha = 0^\circ$ .

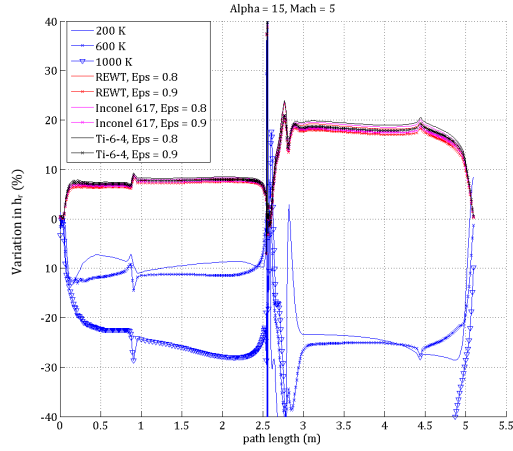


**Figure 4-14** – Comparison of % variation in recovery temperature based heat transfer coefficient as a function of path length along the surface of the wing for each 9 variations in wall boundary conditions at Mach 5 and  $\alpha = 15^\circ$ .

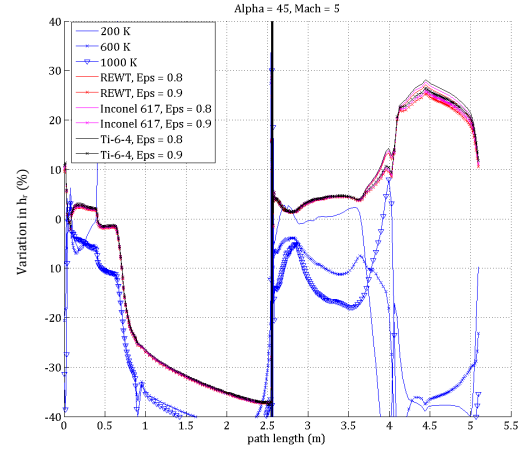


**Figure 4-15**– Comparison of % variation in recovery temperature based heat transfer coefficient as a function of path length along the surface of the wing for each 9 variations in wall boundary conditions at Mach 5 and  $\alpha = 45^\circ$ .

As seen in Figures 4-12 through 4-15, we see that the REWT boundary condition closely approximates the heat transfer coefficient that the conducting walls have. We can also see that, for the Mach 2 cases, the heat transfer coefficient has a large amount of dependence on wall temperature at the leading edge, a path length of 0 m, which is seen in Figure 4-12. This dependence is due to the calculation of the heat transfer coefficient:

$$h_r = \frac{q}{T_w - T_r}$$

where  $T_w \approx T_r$  for the Mach 2 cases. This causes large disparity in  $h_r$  because it is dividing by a number that is nearly equal to zero. This observation is also made in Figure 4-17, where the highest heat flux cells,  $Q/Q_{max} > 0.8$ , have a large discrepancy in heat transfer coefficient.

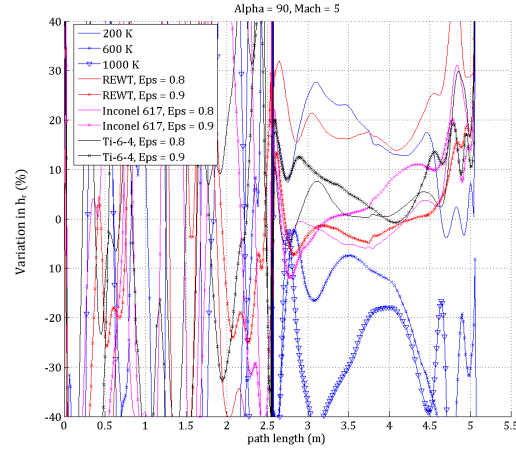


**Figure 4-16** – Comparison of % variation in recovery temperature based heat transfer coefficient as a function of path length along the surface of the wing for each 9 variations in wall boundary conditions at Mach 5 and  $\alpha = 90^\circ$ .

Figure 4-16 shows a break down in predictive capability for a high angle of attack. This could be due to grid dependency or complexity of the flow-field, such as highly turbulent recirculation zones in front of and behind the airfoil.

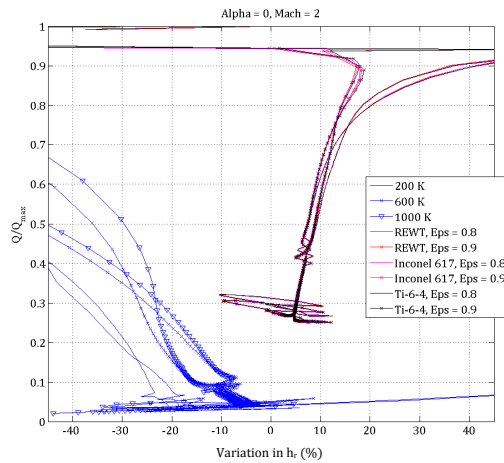


**Figure 4-17** – Comparison of  $Q/Q_{max}$  as a function of % variation in recovery temperature based heat transfer coefficient at Mach 2 and  $\alpha = 0^\circ$ .

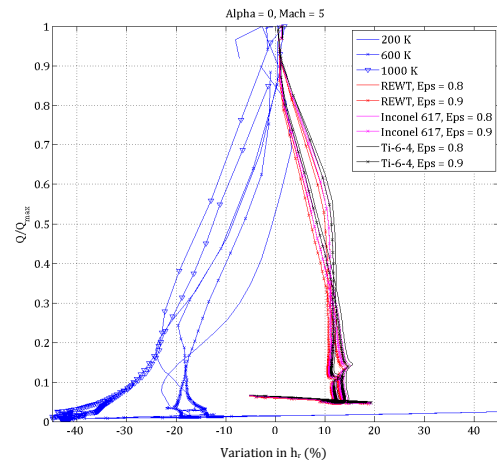


**Figure 4-18** – Comparison of  $Q/Q_{max}$  as a function of % variation in recovery temperature based heat transfer coefficient at Mach 5 and  $\alpha = 0^\circ$ .



The large differences in heat transfer coefficient at the leading edge are not present in the Mach 5 analyses, where the wall temperature is not nearly as close to the recovery temperature. In fact, at  $Q/Q_{max} > 0.3$ , we see a +15% and -20% spread in difference in heat transfer coefficient, illustrated in Figure 4-18.

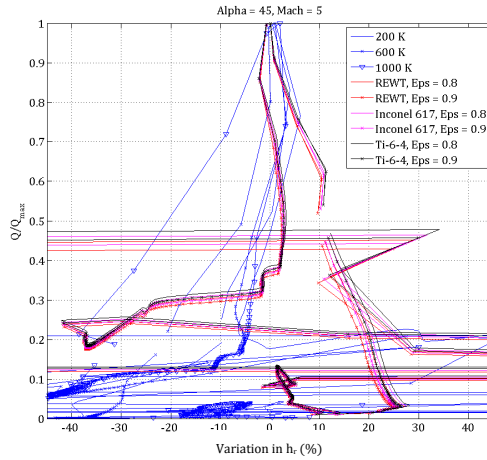


**Figure 4-19** –  $Q/Q_{max}$  as a function of % variation in recovery temperature based heat transfer coefficient at Mach 5 and  $\alpha = 45^\circ$ .

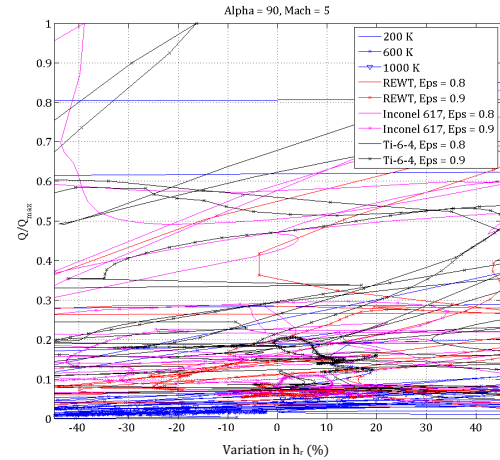


**Figure 4-20** –  $Q/Q_{max}$  as a function of % variation in recovery temperature based heat transfer coefficient at Mach 5 and  $\alpha = 90^\circ$ .

The wall temperature dependency of the heat transfer coefficient begin to look worse as the angle of attack increases to  $45^\circ$ , where the flow-field becomes much more complex, and will likely be driven by transient effects. At  $\alpha = 45^\circ$ , Figure 4-19, the variation in heat transfer coefficient is good for  $Q/Q_{max} = 1$ , where we observe a  $\sim \pm 2\%$  spread in heat transfer coefficient variation. As seen in Figure 4-20, as  $\alpha \rightarrow 90^\circ$ , the difference band becomes atrocious and the heat transfer coefficient cannot be trusted.

As mentioned above, the flow-field becomes very complex at  $\alpha > 45^\circ$  due to large amounts of separation. Figure 4-21 shows the separation occurring behind the airfoil at a  $45^\circ$  angle of attack and Mach 5 flow. Figure 4-22 shows the massive amount of separation behind the airfoil at  $90^\circ$  angle of attack. Here, the wake shows an unphysical flow-field. The

dual recirculation zones are an artifact of the steady state analysis; in steady state, there must be symmetry here to balance the pressure in each eddy. In a real flow, this would be an alternating eddy from one side to the other, which causes a pressure misbalance.

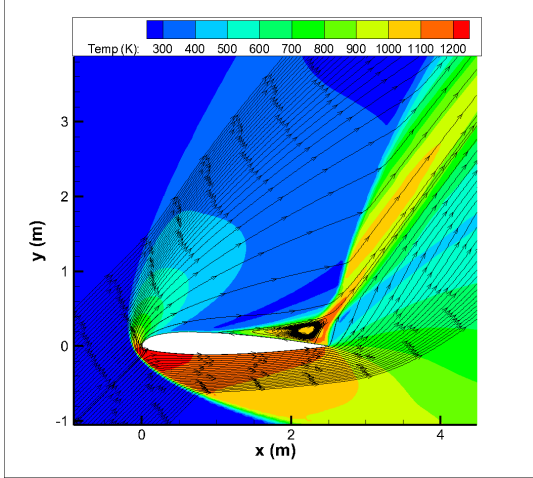


**Figure 4-21** – Separated flow behind the airfoil at Mach 5 and  $\alpha = 45^\circ$ .

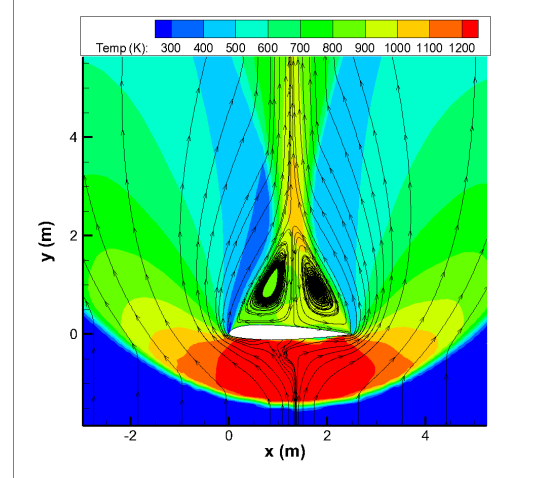


**Figure 4-22** – Separated flow behind the airfoil at Mach 5 and  $\alpha = 90^\circ$ .

The large disparities in heat transfer coefficient on the windward side of the Mach 2 analyses are the result of the wall temperatures being close to the recovery temperature on the windward side. Figures 4-23 and 4-24 show the wall temperatures as a function of path length for two selected flight conditions. The recovery temperatures, using an effective Prandtl number of 0.77, are:

$$T_r = 226.65 \text{ K} \left( 1 + \sqrt[3]{0.77} \frac{1.4 - 1}{2} 2^2 \right)$$

$$T_r = 392.8 \text{ K}|_{M=2}$$

and

$$T_r = 226.65 \text{ K} \left( 1 + \sqrt[3]{0.77} \frac{1.4 - 1}{2} 5^2 \right)$$

$$T_r = 1265.3 \text{ K}|_{M=5}$$

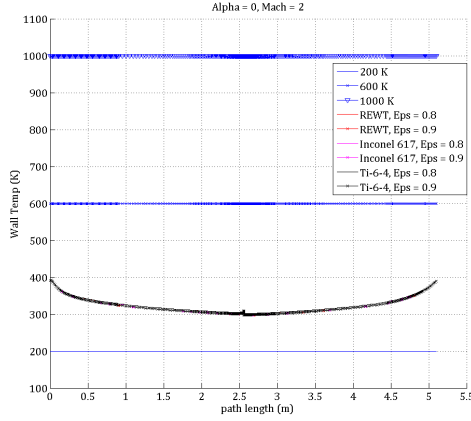


**Figure 4-23** – Wall temperature as a function of path length for Mach 2 and  $\alpha = 0^\circ$ .

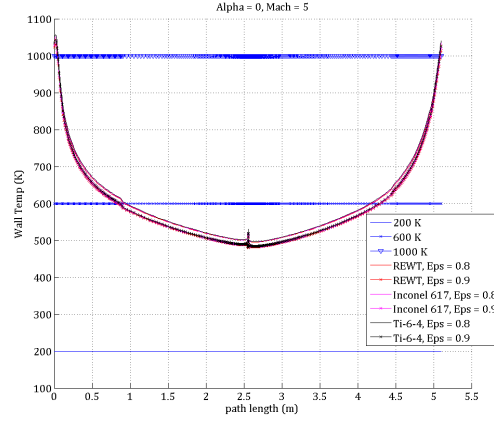


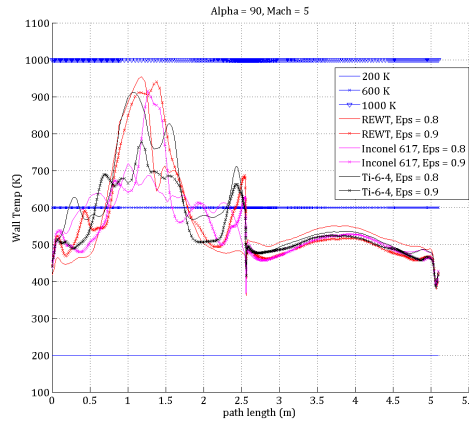
**Figure 4-24** – Wall temperature as a function of path length for Mach 5 and  $\alpha = 0^\circ$ .

The above calculations can be compared to Figures 4-23 and 4-24 to see why the heat transfer coefficients in the Mach 2 cases have large differences at the leading edge, while the Mach 5 cases do not. In Figure 4-23, the wall temperature at a path length of 0 m is nearly identical to the calculated recovery temperature from above; this closeness in wall temperature gives the effect of dividing by zero, and causes large disparity in the calculated heat transfer coefficient. In Figure 4-24, we see that the wall temperature in the same location is nearly 200 K below the recovery temperature.

The reason for the larger difference in wall temperature at the windward side and the recovery temperature for the REWT and conducting walls is that these walls re-radiate heat. From the radiation heat transfer equation, where  $\varepsilon$  is the emissivity,  $\sigma$  is the Stefan-Boltzman constant,

$$q = \varepsilon \sigma A (T_w^4 - T_\infty^4) \quad (4-7)$$

We see that the radiation heat transfer increases with the difference of the fourth power of the temperatures. Thus, the wall temperature drops more significantly the higher the temperature disparity between the free stream and the wall temperature.



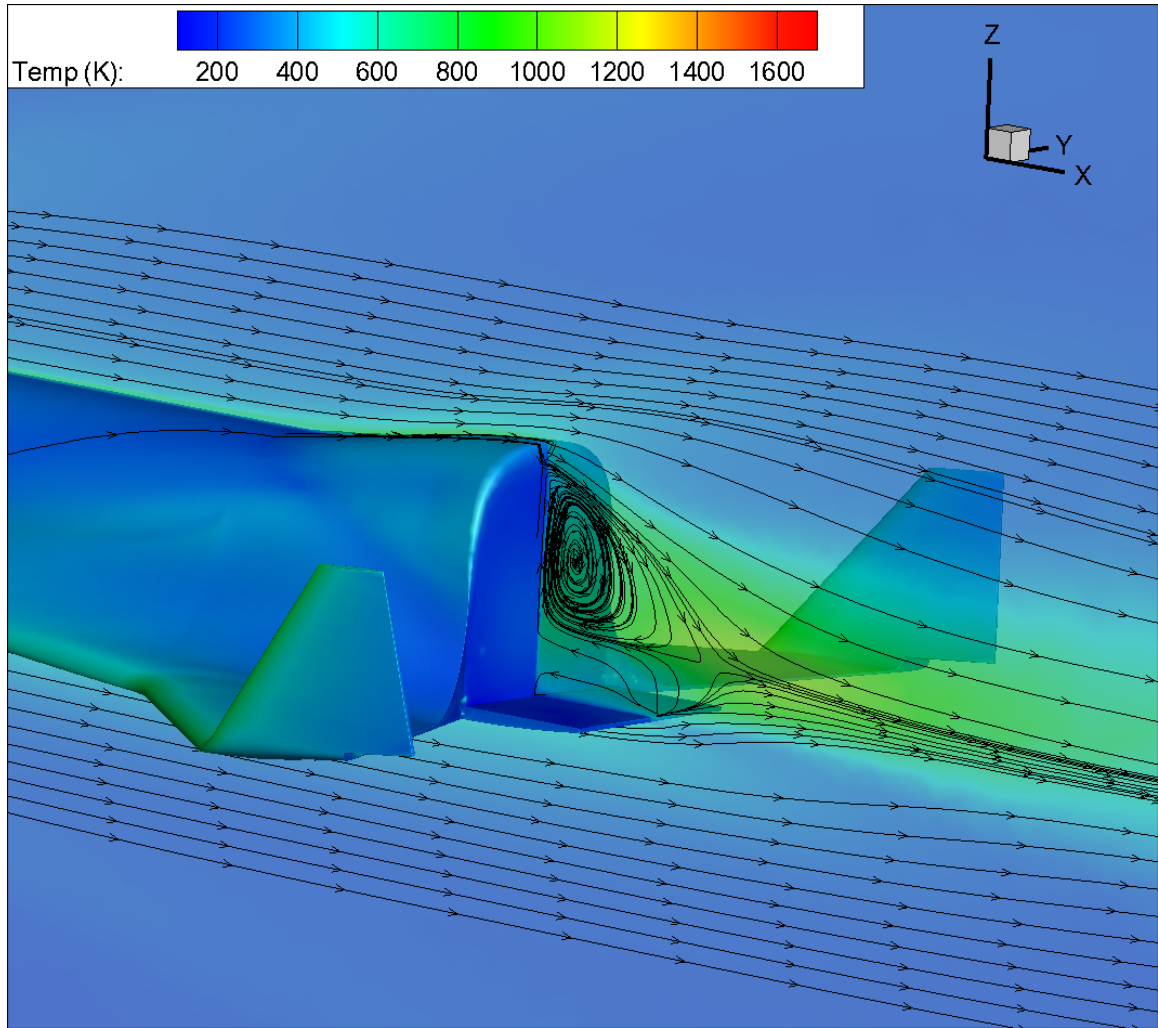
**Figure 4-25** – Wall temperature as a function of path length for Mach 5 and  $\alpha = 90^\circ$ .

Figure 4-25 shows how differently the CFD software is predicting the wall temperatures for the different wall boundary conditions at  $\alpha = 90^\circ$  and Mach 5. These differences in wall temperature illustrate the complexity of the flow-field; as stated previously, this case is probably driven by transient effects. Thus, it is unrealistic to run this case in steady state.

Although large variations in the heat transfer coefficient with respect to wall temperature are observed in zones of recirculation and at high angles of attack, we can use this method with a moderate level of confidence for the trajectory in Chapter 5. For the vast majority of time, the vehicle travels at less than  $45^\circ$  angle of attack. Even during the rocket-back maneuver, the time spent at these high angles of attack is small, so the temperature rise is minimal when a heat transfer coefficient is applied to a material model for a small amount of time.

There are regions of separation, even when the vehicle flies at zero angle of attack, such as in the rear of the vehicle, as seen in Figure 4-26, where there are rocket engines present. Thus, the separation induced variation in the heat transfer coefficient is insignificant in comparison to the plume effect, which is not being modeled in this study. It

is likely that the material selection in this area will be sized by the radiative heating from the plume. The details of this applied problem to a 3-D geometry will be discussed in Chapter 5.



**Figure 4-26** – Illustration of the separation and recirculation around the rear of the vehicle. The streamlines are plotted on the center plane. 30% translucency is applied to the center plane.

The information provided in this chapter allows us to move forward with the transient thermal protection system analysis, covered in Chapter 5. Although there are some large differences in heat transfer coefficient in low heat flux regions, the heat transfer coefficient calculated by the free stream temperature is much larger. For example, the

largest variation in heat transfer coefficient on the 200  $K$  wall from Study B is 108%, but this is in a low heat flux region:  $Q/Q_{max} = 0.03$ . Conversely, for a heat transfer coefficient calculated using free stream temperature instead of recovery temperature on the same wall boundary condition, has a variation of 2,804% at a  $Q/Q_{max} = 1$ . Clearly, we see a large dependency on wall temperature when free stream temperature is used instead of recovery temperature, which accounts for the kinetic energy of the flow.

Because the variations in heat transfer coefficient calculated by free stream temperature are so high when compared to the heat transfer coefficient calculated by recovery temperature, we see the need to use the one generated by the recovery temperature when analyzing the transient temperature profile of a thermal protection system. This process is carried out in Chapter 5.

## CHAPTER 5

### THE APPLIED PROBLEM

The applied problem follows the process flow shown in Figure 5-1. A trajectory and geometry are provided. These parameters are taken into consideration to create a universal grid that will be used in all points solved in the trajectory. This universal grid, along with the trajectory, fed into the external aerothermal analysis, which is comprised of 52 steady state analyses performed in Ansys Fluent. These steady state analyses then are used to calculate recovery temperature based heat transfer coefficients in the manner discussed in Chapters 2 and 4. These heat transfer coefficients, along with a material model of a thermal protection system, are applied to a TPS heat transfer analysis, which is a transient calculation performed in ABAQUS.

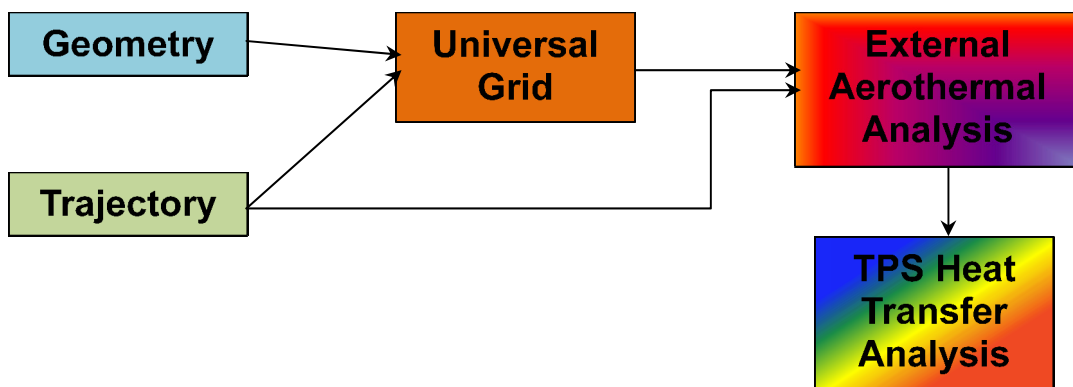


**Figure 5-1** – Schematic of the solution process used in the applied problem.

## A Rocket-back Trajectory

The rocket-back trajectory consists of a rocket-back maneuver, where the vehicle flips its tail into the wind, and uses the main rocket engine to decelerate the booster after second-stage separation. This rocket-back maneuver is apparent in Figure 5-2, which graphically shows the vehicle's altitude and angle of attack over the entire mission. Figure 5-3 shows the Mach number and angle of attack. In this trajectory, the angle of attack peaks just over  $150^\circ$  and the maximum altitude is slightly higher than  $300,000\text{ ft}$ . This trajectory is conceptual and derived for the purpose of the present academic research. It is possible that this trajectory may not be physically realistic.

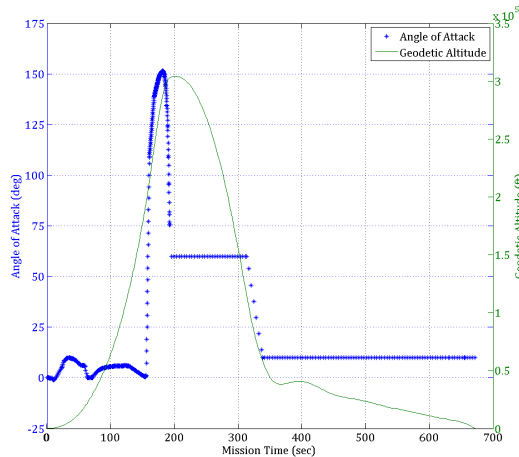


**Figure 5-2** – Angle of attack and geodetic altitude of the given trajectory. The rocket-back maneuver starts at 153 seconds and ends at 193 seconds

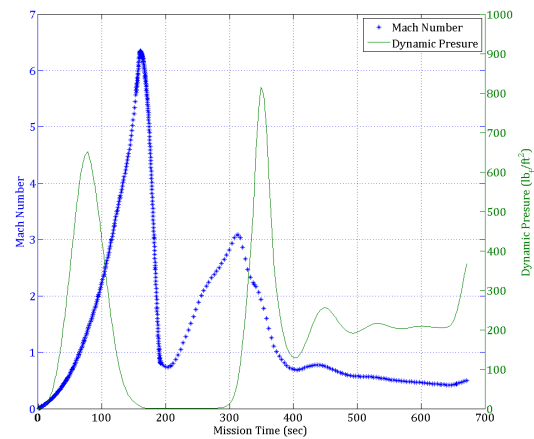


**Figure 5-3** – Mach number and dynamic pressure of the given trajectory.

In order to provide boundary conditions to the CFD code, the 1976 US Standard Atmosphere was used at each trajectory point used in the CFD simulation. More about the implementation of the 1976 US Standard Atmosphere will be discussed in the *Problem Set-up and Solution Procedure* section.

Because the conceptual trajectory is comprised of 472 time steps, the trajectory used for the steady state CFD analyses is coarsened into only 52 points make the problem



tractable. Particular attention is given to the time-region of the rocket-back maneuver, as this is where flight conditions change most rapidly. Figures 5-4 and 5-5 describe the trajectory points used in the CFD analysis.

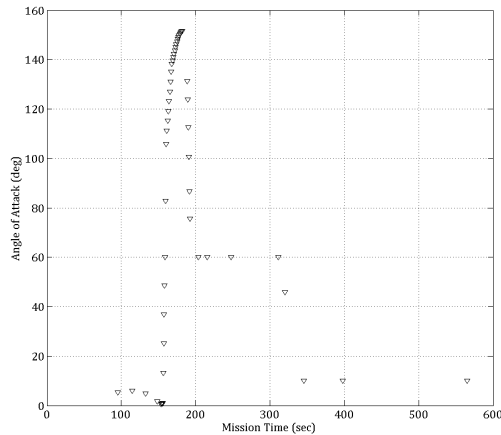


**Figure 5-4** – Angle of attack of the coarsened trajectory used in the applied problem.

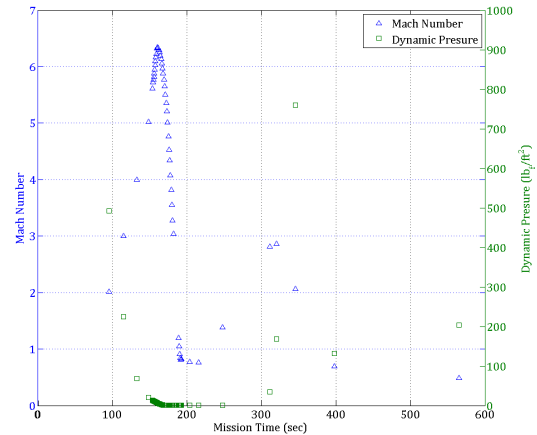


**Figure 5-5** – Mach number and dynamic pressure of the coarsened trajectory used in the applied problem.

## Geometry

The outer mold line of the vehicle is a reusable booster system concept originally designed by Northrop Grumman Corporation for the United States Air Force under a contract with the University of Dayton Research Institute. This vehicle is designed as the first stage of a multi-stage vehicle and is intended to return to earth. Figure 5-6 is a CAD rendering of the outer mold line of the vehicle.

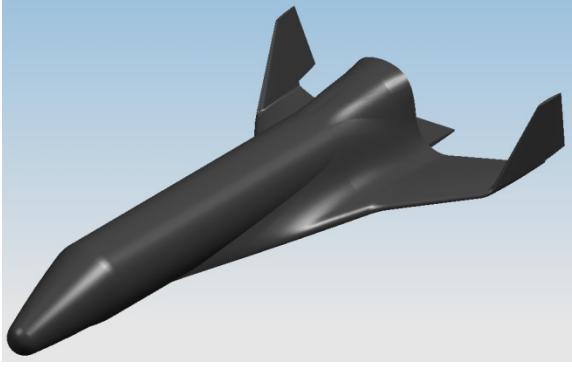


**Figure 5-6** – Outer mold line of the reusable booster system concept.

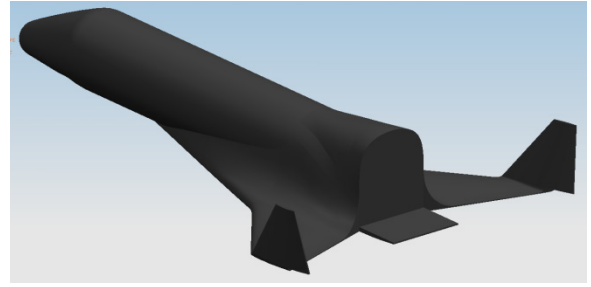


**Figure 5-7** – Rear shot of the outer mold line of the reusable booster system. No engines are modeled.

The vehicle is not modeled with an upper stage or with engines. Figure 5-7 shows the rear of the vehicle with no engine nozzles.

### The Universal Mesh

The Navier-Stokes equations are solved for the volume of the flow-field. As such, for proper capturing of the boundary layer, an inflation layer is utilized. This inflation layer is sized to capture the boundary layer in the entire trajectory that the CFD calculations occur. Prandtl's laminar boundary layer equation for a flat plate serves as an estimate for the boundary layer thickness along the vehicle's surface (Thompson 505):

$$\delta = \sqrt{\frac{\mu x}{\rho u_0}} \quad (5-1)$$

where  $\delta$  is the boundary layer thickness,  $\mu$  is the viscosity,  $x$  is the distance from the leading edge,  $\rho$  is the density, and  $u_0$  is the free stream velocity.

The boundary layer is found to be extremely large at the high altitudes, due to the low density. Conversely, during the ascent phase, the velocity is high and the density is high, so the boundary layer thickness is fairly small. For instance, at an altitude of 188,000 *ft*, and a Mach number of 5.6, the boundary layer thickness at 5 *ft* from the leading edge of the

nose, which is sufficient enough distance from the spherical part of the nose that this theory can be applied, is calculated to be:

$$\delta = \sqrt{\frac{3.3 \times 10^{-7} \frac{\text{slug}}{\text{ft} \cdot \text{s}} \cdot 5 \text{ ft}}{7.71 \times 10^{-7} \frac{\text{slug}}{\text{ft}^3} \cdot 5,868 \frac{\text{ft}}{\text{s}}}}$$

$$\delta = 0.019 \text{ ft} = 0.23 \text{ in}$$

for a laminar boundary layer. A turbulent boundary layer is thicker. The inflation layer's overall thickness is approximately 6 in, but it expands exponentially from a very small thickness. A cross section of the grid near the wall at the symmetry plane is shown in Figure 5-8 and the inflation layer is shown in more detail in Figure 5-9. The corresponding vector plot for the boundary layer, Figure 5-11, in the region of the above calculation shows sufficient capture of the boundary layer; there are about six cells in the boundary layer.

As discussed previously, the heating at the leading edge is driven by the amount of kinetic energy in the flow. Therefore, capturing the boundary layer is not as critical in this region. In addition, at the leading edge, the steepest velocity gradient is parallel to the direction of flow, not normal to the direction of flow as with when the flow is parallel with the wall. The estimated boundary layer thicknesses at 5 ft and 100 ft from the leading edge as a function of time during the rocket-back maneuver is shown in Figure 5-10.

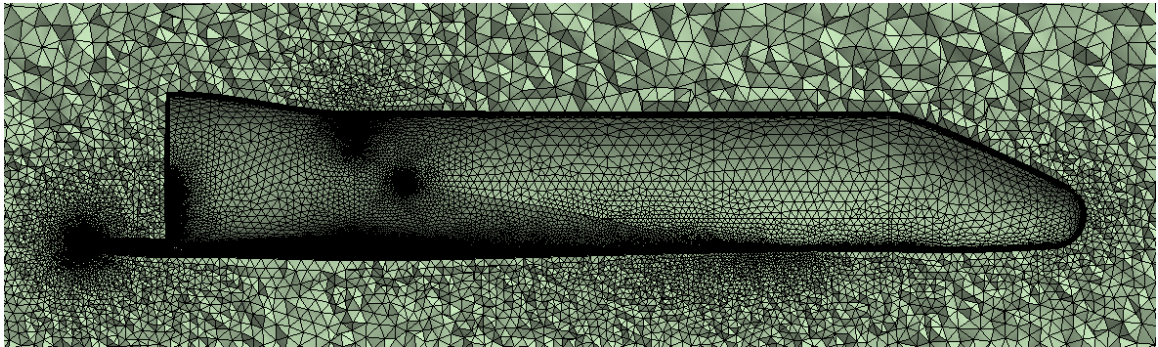


**Figure 5-8** – The computational grid near the wall of the reusable booster system concept.

To create a grid applicable to many angles of attack, the surfaces denoting the vehicle are placed inside a spherical volume. The spherical region that contains the wall boundary is dubbed the dynamic zone. The dynamic zone is rotated based on the angle of attack and bank angle of the supplied trajectory. This sphere exists in a cut-out of the far-field domain; this region is named the stationary zone. The interface of the dynamic and stationary zones is a non-conformal interface, which requires interpolation to pass information between the two regions; the interpolation is a source of some error in the solution. Pictures of the spherical region and the entire computational grid are shown in Figures 5-12 and 5-13, and a view of the non-conformal interface is shown in Figure 5-14.

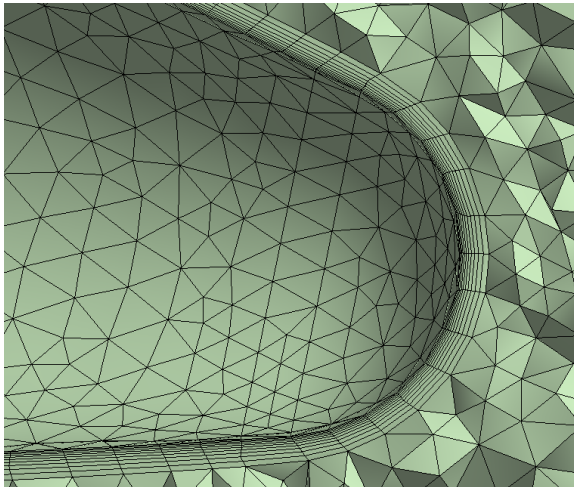


**Figure 5-9** – Detail of the inflation layer.

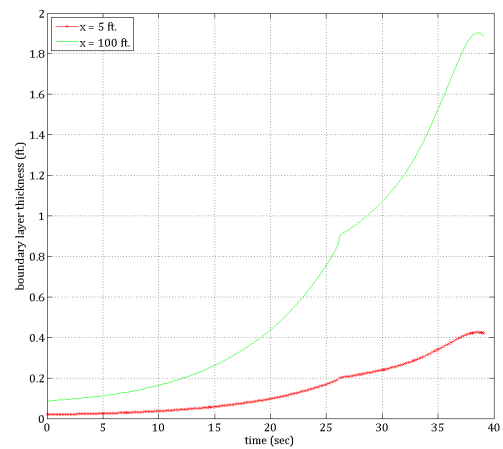


**Figure 5-10** – Estimate of the boundary layer thickness using Prandtl's boundary-layer equation.

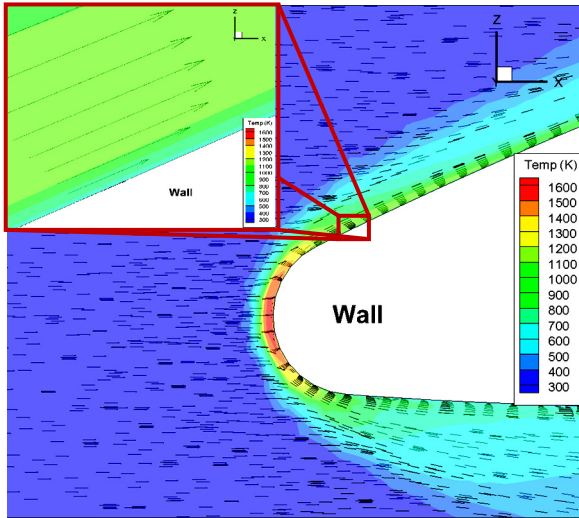


**Figure 5-11** – Vector plot of the boundary layer thickness at Mach 5.6, altitude of 188,000 *ft* and, 5 *ft* distance from the leading edge of the nose.

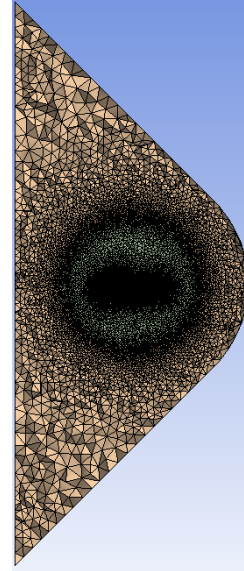


**Figure 5-12** – Cross sectional view of the computational domain showing the dynamic zone (green spherical region) and the stationary zone (beige region).

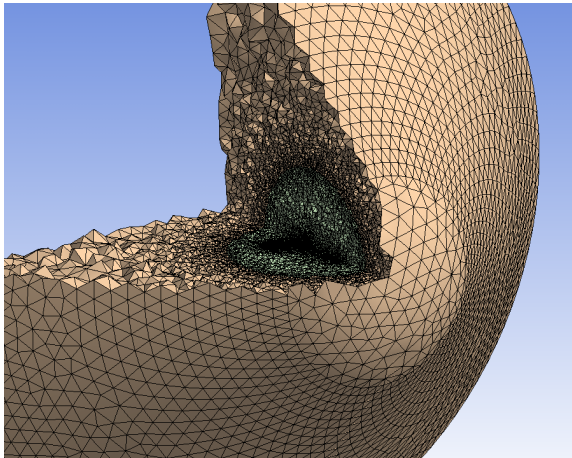


**Figure 5-13** – Three-dimensional sectioned view of the dynamic zone inside the stationary zone.

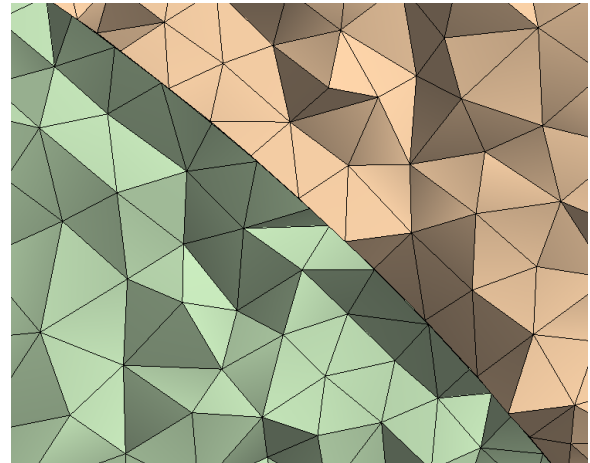


**Figure 5-14** – Non conformal interface.

The mesh metrics are as follows. There are 26,245,437 volume elements, 6,083,498 nodes in the volume, and 469,396 faces on the wall. The maximum cell skewness is 89.98%, well within the limit of Fluent's double precision solver. The maximum aspect ratio is 137.6.

### **Problem Set-up and Solution Procedure**

With the exception of the boundary conditions, the problem is set up identically to the one in Chapter 4. Because the machine used to solve the applied problem has a Linux operating system using a batch scheduling system, there is no graphical user interface or interaction to the solver. Thus, journal files are used to set up the boundary conditions, rotate the mesh, initialize the flow-field, run the calculation, save the case and data files, and export any needed data. These journal files are created in MATLAB, which reference the given trajectory in Excel format. This process does not require setting up unique case and data files for each boundary condition.

### **Computational Resources**

The steady state calculations were performed on AFRL's Raptor, a Cray XE6 with 2.4 GHz core speed and 16 cores per node. The CPUs are AMD Opteron 64-bit processors and have 32 GB of memory per node. It uses a Cray Gemini interconnect type. Each case file, which contains the mesh, boundary conditions, and solver settings, is about 1.7 GB of data. Each data file, which contains the solution data at each element, is about 3.9 GB. Clearly, there is a large amount of computational resource required to solve each steady state analysis. During the initial stages of the computation, there was a scalability study performed, the results of which are presented in Figure 5-15 and 5-16.

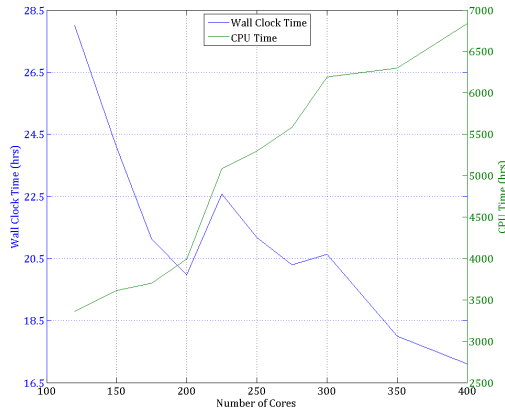


**Figure 5-15** – Wall clock time and CPU time as a function of number of cores in the scalability study.

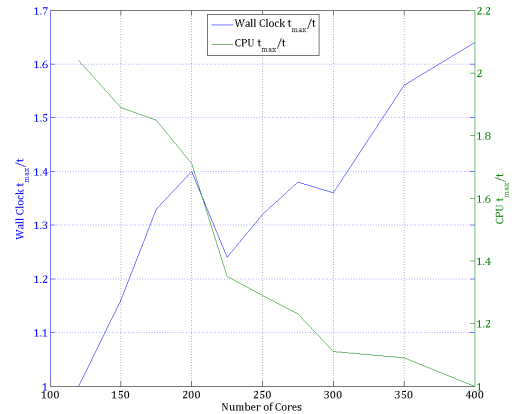


**Figure 5-16** – Wall clock  $\frac{t_{max}}{t}$  and CPU  $\frac{t_{max}}{t}$  as a function of number of cores in the scalability study.

The scalability study resulted in the choice of 200 cores as the optimum number of processors. Although the 200 core choice is not as computationally efficient as the lower number of cores, it is completed in approximately 20 hours. With file transfer time, this results in about 24 hours per job. This is a convenient time, as it was fast enough that down time with the system did not become much of an issue, yet still computationally efficient.

In total, the total amount of CPU time for the steady state analyses is 230,924 hours, or 26 years, and the total amount of wall clock time is 34 days.

## Energy Balance

Before setting up the transient TPS model, it must be ensured that the heat transfer coefficients obey conservation of energy. The field of recovery temperature based heat transfer coefficients for one flight condition is chosen. This field is then applied to a surface grid of the wall boundary only. This should yield the same temperature profile as the CFD results for radiation equilibrium wall temperature at the same flight conditions. The energy equation is balanced in the following manner:



$$\sigma \varepsilon (T_w^4 - T_s^4) = h(T_r - T_w) \quad (5-2)$$

where  $\sigma$  is the Stefan-Boltzmann constant,  $\varepsilon$  is the emissivity,  $T_w$  is the wall temperature,  $T_s$  is the radiative sink temperature, and  $T_r$  is the recovery temperature. Indeed, the energy equation is balanced. Figure 5-17 shows the results from the CFD analysis using a radiation equilibrium wall temperature boundary condition, and Figure 5-18 is the result of the field of recovery temperature based heat transfer coefficients. These pictures are identical, which proves the energy equation is balanced.

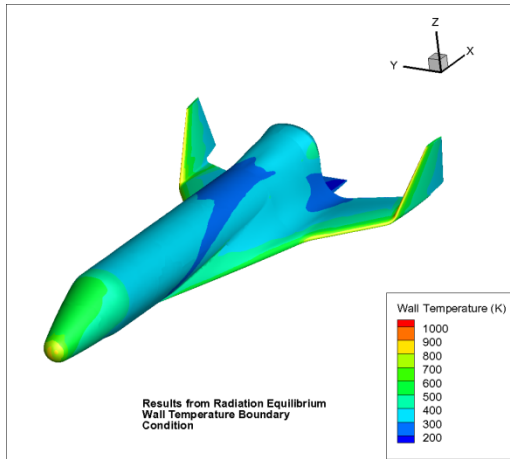


**Figure 5-17** – CFD results from the radiation equilibrium wall temperature boundary condition.

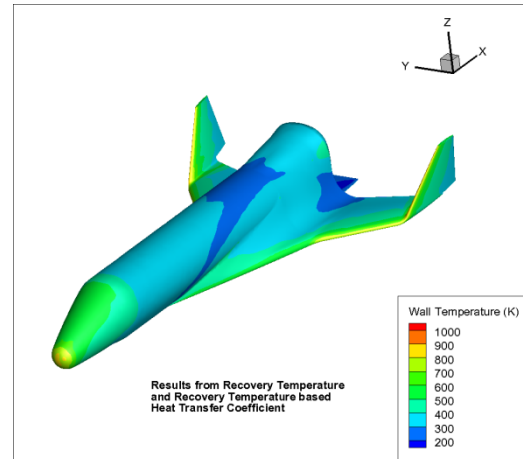


**Figure 5-18** – Temperature field based on the balance of the energy equation, Equation (5-2).

### FEA TPS Model

Once the steady state CFD results are complete, the heat transfer coefficient is calculated by exporting the heat flux, wall temperature, and effective Prandtl number to a tab delimited Tecplot format, which is easily read into MATLAB. The data is then exported to a comma-delimited format which is easily read into the Finite Element Analysis (FEA) software.

The FEA model of the thermal protection system was performed in ABAQUS. This software is a very comprehensive FEA modeler. This software is chosen for its ability to solve a conduction heat transfer problem in three dimensions with a shell-stack model and



a convective boundary condition. This shell stack uses shell elements, which are essentially surface elements of the geometry. Then, it applies integration points to the elements, and allows for composite layering, thus creating a shell stack.

The grid is extremely coarse, as there are not regions of high gradient on the same order of magnitude as a CFD problem, such as in the boundary layer, or a stress problem, such as the area of a stress riser. Figure 5-19 shows the FEA grid, which can be compared to Figure 5-20, which is the wall boundary of the CFD grid. Note that the CFD grid is especially fine around the leading edges and wing tips.

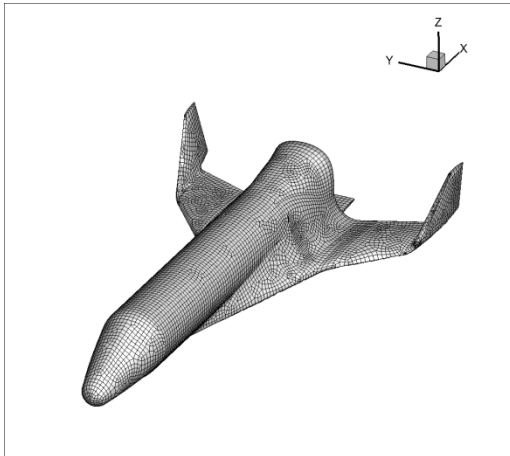


**Figure 5-19** – FEA grid used in the transient heat transfer analysis, which has 11,912 shell elements.

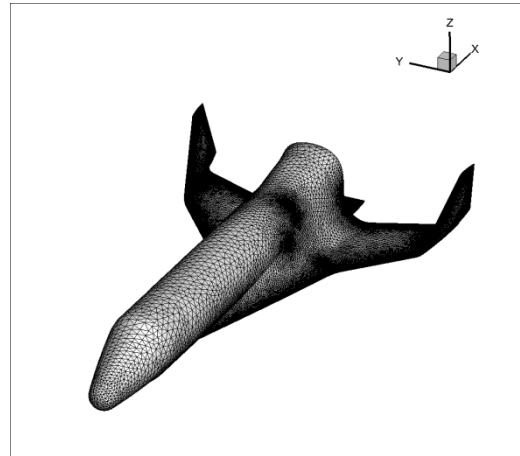


**Figure 5-20** – CFD grid at the wall boundary, which has 469,396 faces at the wall.

The material model is a metallic thermal protection system concept. The material thicknesses are summarized in Table 5-1, and the Material Properties are summarized in Table 5-2. The materials are modeled as constant density and thermal conductivity and specific heat capacity as a function of temperature in order to more realistically model the transient thermal temperature profile.

**Table 5-1** – Material thickness for the thermal protection system model.

<b>Material</b>	<b>Thickness (in)</b>	<b>Integration Points</b>
Inconel-617	0.006	3
PM-1000	0.01	3
Inconel-617	0.0015	3
PM-1000	0.01	3
Inconel-617	0.016	3
Q-Fiber	0.5	3

**Table 5-2** – Material thermal properties for the thermal protection system model.

<b>Inconel 617</b>			<b>PM-1000</b>			<b>Q-Fiber</b>		
$T (K)$	$k \left( \frac{W}{m \cdot K} \right)$	$C_p \left( \frac{J}{kg \cdot K} \right)$	$T (K)$	$k \left( \frac{W}{m \cdot K} \right)$	$C_p \left( \frac{J}{kg \cdot K} \right)$	$T (K)$	$k \left( \frac{W}{m \cdot K} \right)$	$C_p \left( \frac{J}{kg \cdot K} \right)$
144	10.52	385	294	12.01	439	144	0.0298	209
366	16.03	435	473	17.01	502	311	0.0298	643
478	18.88	464	773	23.06	619	366	0.0389	787
589	21.12	490	1022	29.98	720	422	0.0476	932
700	23.39	519	1272	37.04	820	478	0.0562	1025
811	25.84	548	1472	41.94	891	589	0.0760	1079
922	28.64	573				700	0.0971	1111
1033	31.41	602				811	0.1195	1141
1144	34.24	628				922	0.1438	1166
1366	39.68	682				1033	0.1731	1178
						1089	0.1887	1182
						1144	0.2073	1187
						1255	0.2422	1195

The model of the thermal protection system is initialized at 300 K and the heat transfer coefficient is held constant through the entire time-step. The results are reported at the end of each time-step.

## Results

The results of the FEA are consistent with expectations. During the ascent phase, the steady state temperature field over-predicts temperatures when compared to the transient

temperature field, as seen in Figure 5-21. This figure shows the temperature profile for 133 seconds into the flight, at Mach 4, a  $4.87^\circ$  angle of attack, and an altitude of 130,000 *ft* along the symmetry plane,  $y = 0$  *m*. The temperature profile has the same characteristic as the steady state temperature profile, but has obviously not reached equilibrium. The peak temperature lies in the region of the nose, which corresponds to a path length of 0 – 5 *m* and 55 – 60 *m*. In Figures 5-21 through 5-23, a path length range of 0 – 30 *m* is the upper surface, starting at the nose, and a path length range of 31 – 60 *m* is the lower surface, ending at the nose.

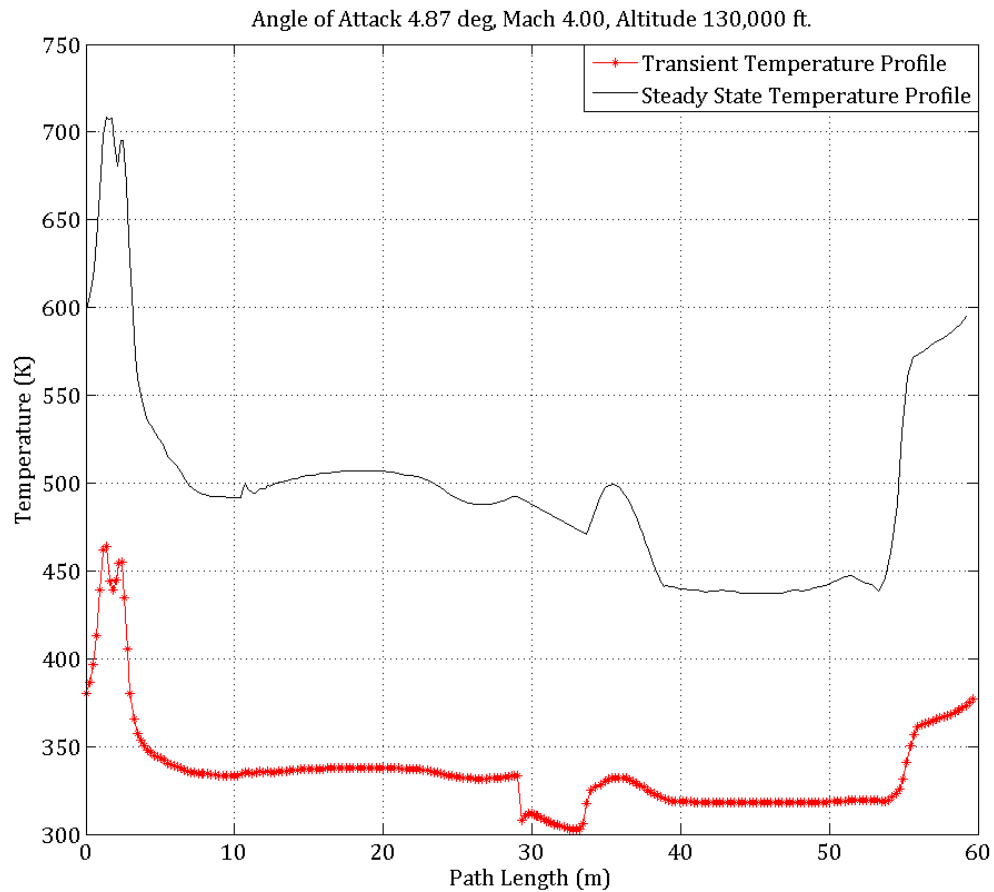


**Figure 5-21** – Temperature profile comparison of steady state CFD and transient TPS analysis for  $M = 4$ ,  $\alpha = 4.87^\circ$ , and  $z = 130,000$  *ft* at the symmetry plane  $y = 0$  *ft*.

At a mission time of 159.5 seconds, the vehicle is at a  $82.9^\circ$  angle of attack. The steady state CFD results reflect this high angle of attack in its temperature profile, which peaks near the nose, an area of very low cross sectional area and also still the leading most point. The temperature drops towards the rear of the vehicle at a path length of 30 m, as seen in Figure 5-22. The transient temperature profile is much different here. It still displays thermal effects from previous flight conditions, most evidenced by the high temperature at the nose tip and the low temperature everywhere else. Because the vehicle spends very little time at these flight conditions, there is not enough heat transfer to substantially raise the temperature of the thermal protection system.

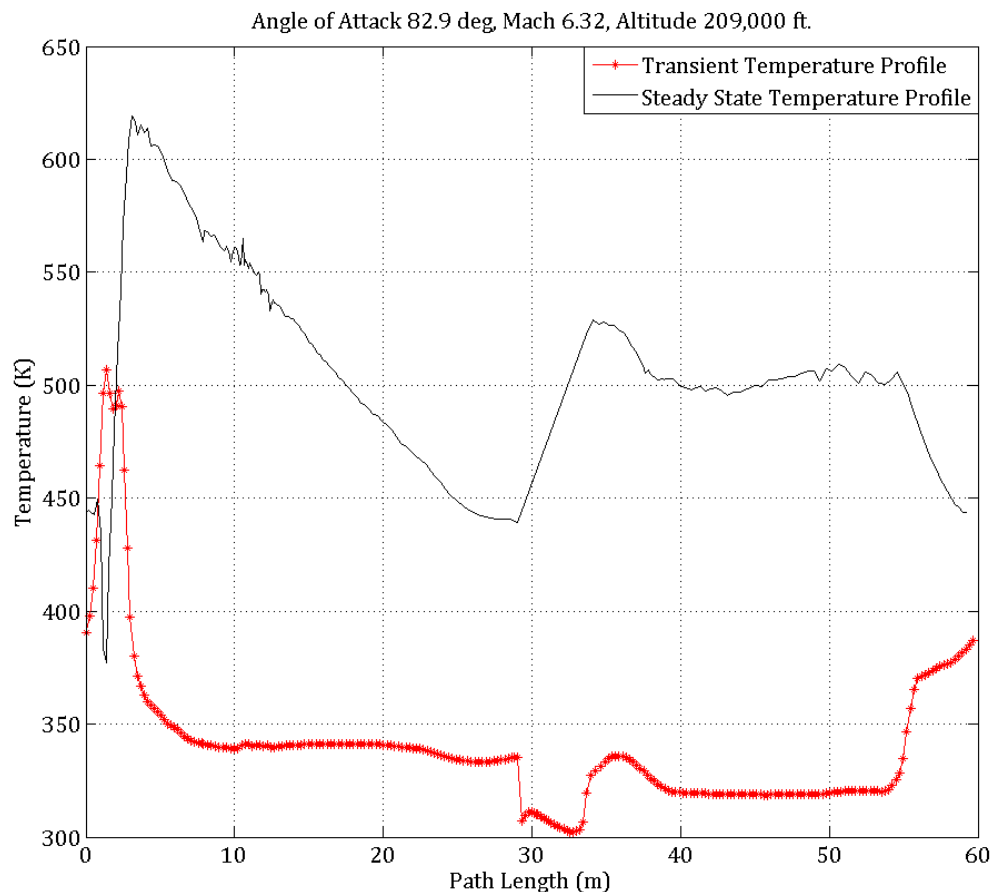


**Figure 5-22** – Temperature profile comparison of steady state CFD and transient TPS analysis for  $M = 6.32$ ,  $\alpha = 82.1^\circ$ , and  $z = 209,000\text{ ft}$  at the symmetry plane  $y = 0\text{ ft}$ .

By the time the vehicle has traveled for 180.7 seconds, it has reached an angle of attack of  $151.3^\circ$ , an altitude of 285,000 *ft*, and has slowed to a Mach number of 3.28. This is the peak angle of attack during the rocket-back maneuver. Because the vehicle is now going relatively slowly, especially at such a high altitude, the steady state results under-predict the temperature profile of the surface because the thermal protection has acted like a thermal battery, storing the energy from previous flight conditions. This result follows intuition.

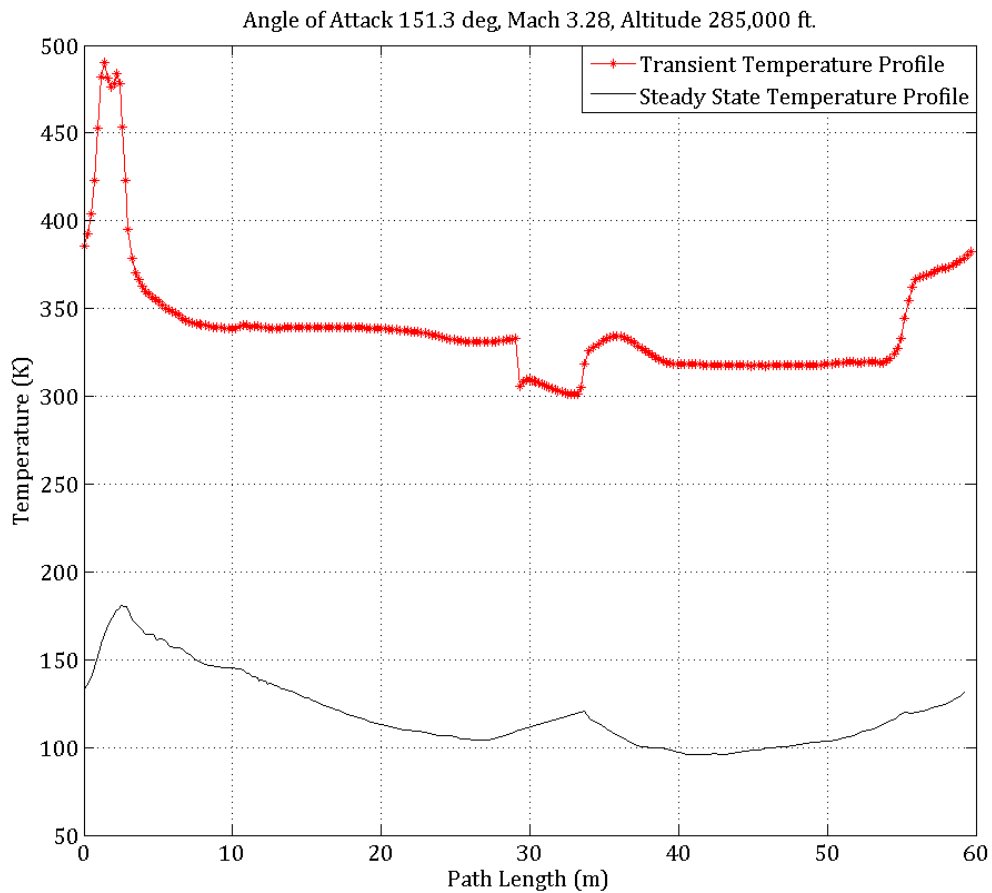


**Figure 5-23** – Temperature profile comparison of steady state CFD and transient TPS analysis for  $M = 3.28$ ,  $\alpha = 151.3^\circ$ , and  $z = 285,000$  *ft* at the symmetry plane  $y = 0$  *ft*.

Figures 5-24 through 5-29 show the temperature contours of the cases examined in Figures 5-21 through 5-23. Note that the temperature scales are not the same in each case;

this difference in scaling is to allow for the visibility of the temperature distribution in each case.

Appendix B summarizes the job name, mission time, integrated total surface heat flux, dynamic pressure, angle of attack, and Mach number for the CFD cases that were run, which provided the heat transfer coefficients that are boundary conditions for the transient model.

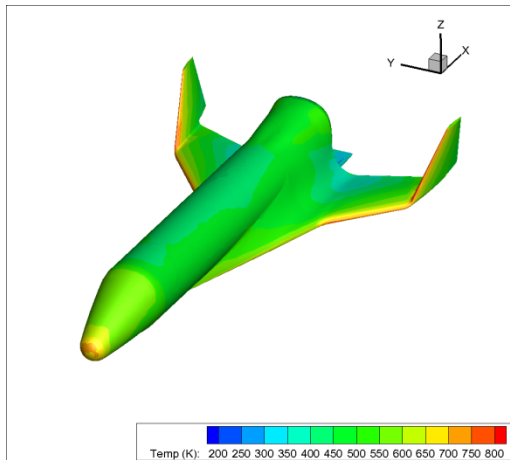


**Figure 5-24** – Steady state temperature contour for  $M = 4$ ,  $\alpha = 4.87^\circ$ , and  $z = 130,000 \text{ ft}$ .

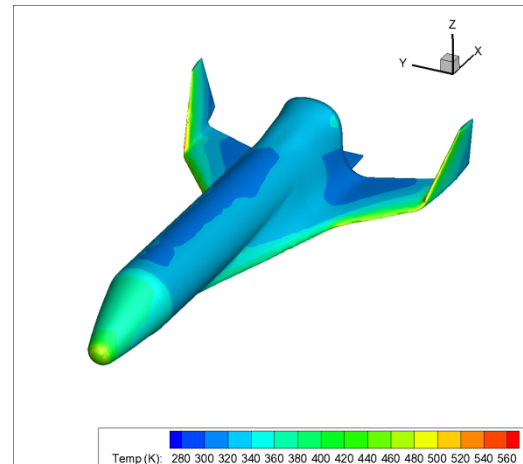


**Figure 5-25** – Transient temperature contour for  $M = 4$ ,  $\alpha = 4.87^\circ$ , and  $z = 130,000 \text{ ft}$ .

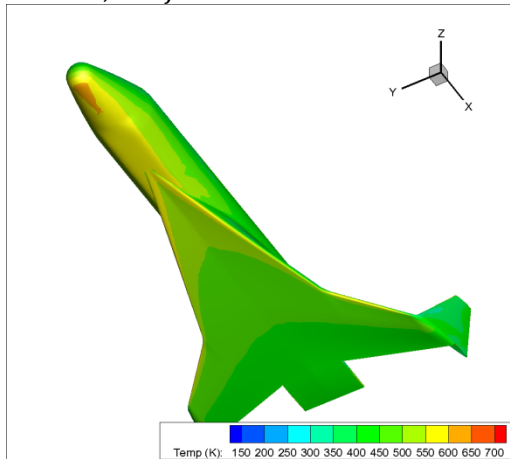


**Figure 5-26** – Steady state temperature contour for  $M = 6.32$ ,  $\alpha = 82.1^\circ$ , and  $z = 209,000 \text{ ft}$ .

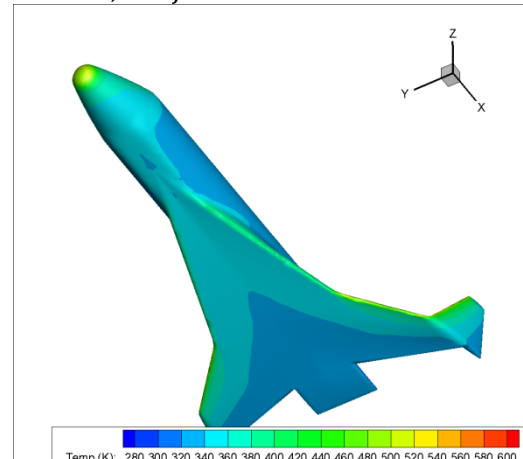


**Figure 5-27** – Transient temperature contour for  $M = 6.32$ ,  $\alpha = 82.1^\circ$ , and  $z = 209,000 \text{ ft}$ .

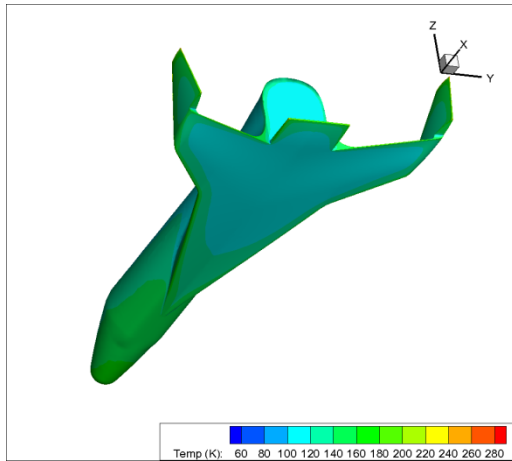


**Figure 5-28** – Steady state temperature contour for  $M = 3.28$ ,  $\alpha = 151.3^\circ$ , and  $z = 285,000$  ft.

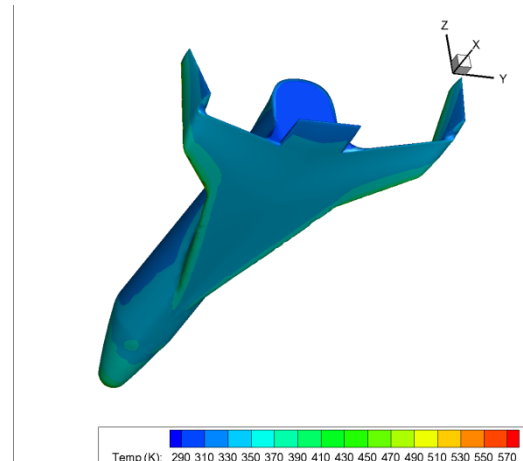


**Figure 5-29** – Transient temperature contour for  $M = 3.28$ ,  $\alpha = 151.3^\circ$ , and  $z = 285,000$  ft.

An important point that needs to be expressed is that the transient analysis accounts for the residence time of the vehicle at specific boundary conditions as well as the characteristic heat transfer rate. For example, the “thermal mass” can be witnessed in Figure 5-23, where the transient temperature profile is much larger than the steady state, REWT temperature profile. This example shows that the process follows reason.

The transient temperature profile will be affected by the material selection, trajectory, and geometry. In Chapter 4, there were examinations of an Inconel 617 wall, a Ti-6Al-4V wall, a radiation-adiabatic wall, and three isothermal walls. We saw that the same analysis can be performed on walls that have different temperature profiles; these different temperature profiles will result from the different material selections, different geometries, and different trajectories. Thus, this process can be used on more than the geometry, thermal protection system material choices, and trajectory used in Chapter 5. Improvements to this method and an expansion on the significance of the results are presented in Chapter 6.

## CHAPTER 6

### CONCLUSIONS AND RECOMMENDATIONS

#### Conclusions

The results presented in Chapter 4 allowed us to proceed with an applied problem, which is presented in Chapter 5. A transient temperature profile is generated in Chapter 5; this transient temperature profile can be used to size the thermal protection system. Sizing the thermal protection system means that the materials can be selected, and thicknesses scaled. The process of sizing the TPS is an iterative one; we would take the generated heat transfer coefficients from the steady state analyses and run numerous transient TPS analyses until we have settled on a material and thickness that satisfies our design criteria.

The numerous heat transfer coefficients from Chapter 5 can also be used in a transient temperature profile of a structure coupled with a thermal protection system. The heat transfer coefficients serve as an outer mold line boundary condition, and the thermal response of the system can be analyzed, given the heat generation rates of the internal components that generate heat, such as avionics, actuators, batteries, and computers.

Clearly, we see that the results from this thesis mean that there is a large applicability of the process used here, and that the transient temperature profile can be generated and used instead of using steady state results. Again, in Chapter 5, we saw that the steady state CFD results have a large over-prediction in peak temperature. For example, in Figure 5-21, there is approximately a  $250\text{ K}$  over-prediction of wall temperature at the nose of the vehicle, a path length of  $2\text{ m}$ . This large over-prediction is the difference



between a more expensive material and a cheaper one, or perhaps using a thinner TPS, which results in weight and cost savings.

Of more importance is the speed at which this analysis can be carried out. In today's rapid design environment, the use of high fidelity tools such as CFD and FEA needs to take place earlier in the design phase, at the conceptual level. The use of steady state analyses to create a series of heat transfer coefficient fields coupled with a universal mesh allows this rapid design to take place. Here, we have been able to demonstrate that a first pass design at a thermal protection system can be had in slightly over a month's time, as seen in Chapter 5. This allows the thermal problems to be attacked early in the design phase instead of pushing the problem back to the final design phases, a typical practice in current high speed vehicle design. Thus, the thermal management can be integrated into the entire design at the conceptual level. The result is a more accurate understanding of weight, propellant mass fractions, cost, and material selection at the conceptual level.

### **Further Research**

Although the recovery temperature based heat transfer coefficient has a large wall temperature dependency in low heat flux regions of the wall, the method presented is extremely useful to the TPS engineer. The method is reasonably quick to execute and allows a much greater level of analysis fidelity than previously available during the early stages of a hypersonic vehicle design program. The recovery-temperature based heat transfer coefficient more weakly dependent on wall temperature than free stream temperature based heat transfer coefficient. Owing to this fact, the use of steady state CFD simulations can be used in place of the much more time consuming transient CFD with conjugate heat transfer analyses. The free stream temperature based heat transfer coefficient can be up to

300 times different depending on the thermal boundary condition used at the wall. Clearly, accounting for the kinetic and thermal energies in the flow is necessary.

In an earlier discussion, it was noted that the isothermal walls have less variability in heat transfer coefficient than the radiation equilibrium wall temperature walls. It is hypothesized that this variability is due to the presence of a thermal gradient along the wall. This hypothesis is based on the fact that the flow-field is not greatly affected by the wall temperature in high speed flow: the flow-field is dominated by the momentum of the flow rather than the temperature of the wall, which does not hold for lower speed cases. The energy is being picked up near the stagnation point then deposited down-stream; this energy transfer is not being accounted for in the heat transfer coefficient when thermal gradients are not present.

One possibility of improving this predictive capability is to use a local recovery temperature; that is, use the velocity and temperature at the edge of the boundary layer. This task is much more difficult because an algorithm must be developed to extract edge of boundary layer data. Additionally, this algorithm must handle zones with high recirculation, such as the one depicted in Figure 6-1, which is the leeward side of the wing at a 90° angle of attack. Using CFD generated streamlines in two-dimensions or path lines in three-dimensions could serve as the method for extraction of the local recovery temperature.

The use of CFD generated streamlines at the boundary layer's edge would allow for extraction of pertinent data, such as the velocity and temperature of the flow along the line of interest. Additionally, the angle the streamline takes with the solid boundary may also be calculated, which could be used to calculate an effective velocity, or velocity projected to the coordinates of the wall. This method could more accurately predict the amount of kinetic and thermal energy in the flow-field near that specific point at the wall. Another approach

that might be available in the foreseeable future, although not cost effective today, is to use a Navier-Stokes flow solution coupled to a FEA TPS solution.

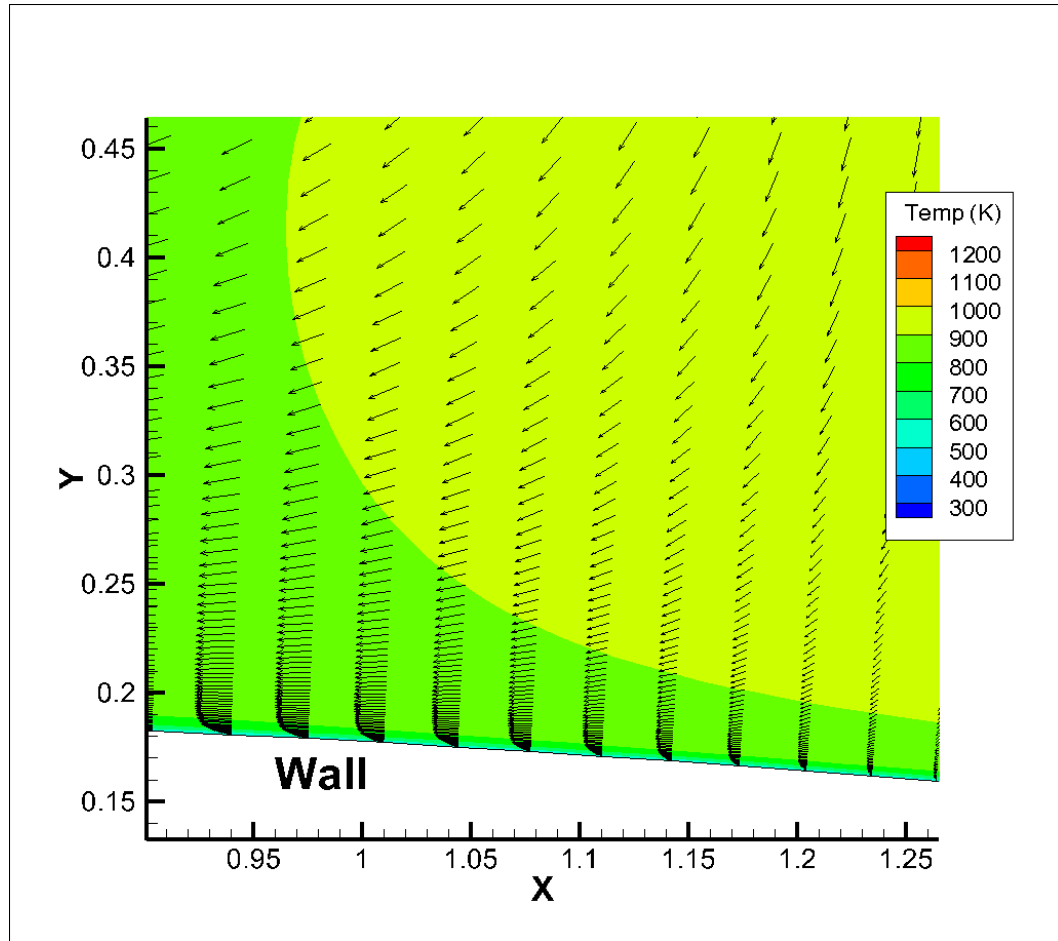


**Figure 6-1** – Turbulent recirculation zone behind an airfoil at a 90° angle of attack.

Another flow regime that the recovery temperature based heat transfer coefficient could be expanded to is chemically reacting hypersonic flows. The recovery temperature is developed using the ideal gas assumption; an alternate method of formulation of the recovery temperature for chemical dissociation is given by the following equation:

$$\frac{T_r}{T_\infty} = 1 + \frac{\gamma - 1}{2} \left( \text{Pr} M_\infty^2 - \frac{2\theta_D}{\gamma T_\infty} \right) \quad (6-1)$$

where  $\gamma$  refers to the ratio of specific heats for the undissociated gas and  $\theta_D$  is the characteristic temperature of air (Liepmann and Roshko 351). This formulation of recovery temperature holds for extremely high Mach numbers because it accounts for the heat consumed by the chemical reaction.

If the above suggestions are considered, we can see a larger applicability of the method employed in this study, which could, perhaps, alleviate the need for transient CFD in re-entry and high speed flows for many years. This will result in more rapid solutions to thermal problems, which can result in faster design turn-around.

## BIBLIOGRAPHY

- Anderson, Jr., John D. Fundamentals of Aerodynamics. 5th Edition. New York: McGraw-Hill, 2011.
- Ansys, Inc. Ansys Fluent 12.0 Theory Guide. 2009.
- Blazek, J. Computational Fluid Dynamics: Principals and Applications. 2nd Edition. Elsevier, 2008.
- Fricker, Darren, John Mendoza and Ivan Catton. "A Summary of the Computational Fluid Dynamics Analysis of the Hypersonic Flights of Pegasus." AIAA Technical Report. 1992.
- Hirschel, E. H. Basics of Aerothermodynamics. Zorneding: Springer, 2005.
- Liepmann, H. W. and A. Roshko. Elements of Gasdynamics. New York City: Dover Publications, 1985.
- Matweb, LLC. Special Metals INCONEL(R) Alloy 617. 2011. 22 September 2011  
<<http://www.matweb.com/search/DataSheet.aspx?MatGUID=adf2123d8e494e75aef7417989ffea92>>.
- Matweb, LLC. Titanium Ti-6Al-4V (Grade 5), Annealed. 2011. 23 September 2011  
<<http://www.matweb.com/search/DataSheet.aspx?MatGUID=a0655d261898456b958e5f825ae85390&ckck=1>>.
- Roy, Christopher J. and Frederick G. Blottner. "Methodology for Turbulence Model Validation: Application to Hypersonic Flows." Journal of Spacecraft and Rockets 40.3 (2003): 313-325.

- Schlichting, Hermann. Boundary-Layer Theory. 7th Edition. McGraw-Hill, 1979.
- Sonntag, Richard E., Claus Borgnakke and Gordon J. Van Wylen. Fundamentals of Thermodynamics. 6th Edition. John Wiley & Sons, 2003.
- Strobel, Forrest, Todd Tillman and Belinda King. "User's Manual for the Aeroheating and Thermal Analysis Code (ATAC07)." Hunstville: ITT Corporation, Advanced Engineering & Sciences Division, August 2007.
- Thompson, Phillip A. Compressible-Fluid Dynamics. 1988.
- White, Frank M. Viscous Fluid Flow. 3rd Edition. New York: McGraw-Hill, 2006.
- Wilcox, David C. Turbulence Modeling for CFD. 3rd Edition. DCW Industries, 2010.

## APPENDIX A

### HEAT TRANSFER COEFFICIENT VARIABILITY PLOTS AND WALL TEMPERATURE PLOTS

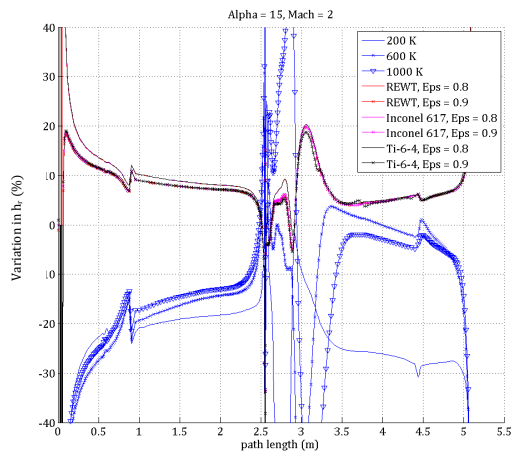


**Figure A-1** – Comparison of % variation in recovery temperature based heat transfer coefficient as a function of path length along the surface of the wing for each 9 variations in wall boundary conditions at Mach 2 and  $\alpha = 15^\circ$ .

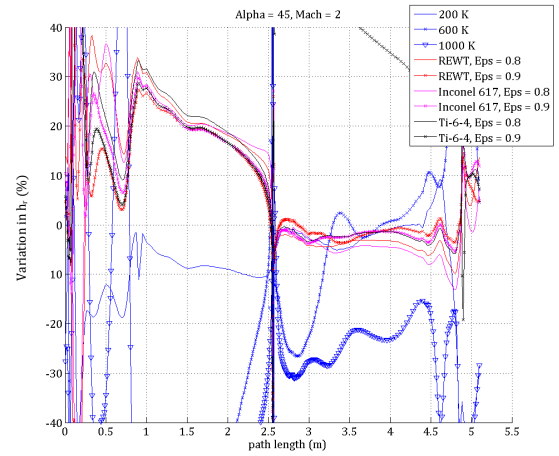


**Figure A-2** – Comparison of % variation in recovery temperature based heat transfer coefficient as a function of path length along the surface of the wing for each 9 variations in wall boundary conditions at Mach 2 and  $\alpha = 45^\circ$ .

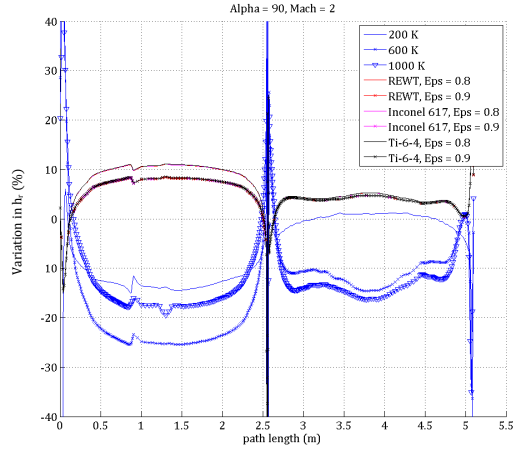


**Figure A-3** – Comparison of % variation in recovery temperature based heat transfer coefficient as a function of path length along the surface of the wing for each 9 variations in wall boundary conditions at Mach 2 and  $\alpha = 90^\circ$ .

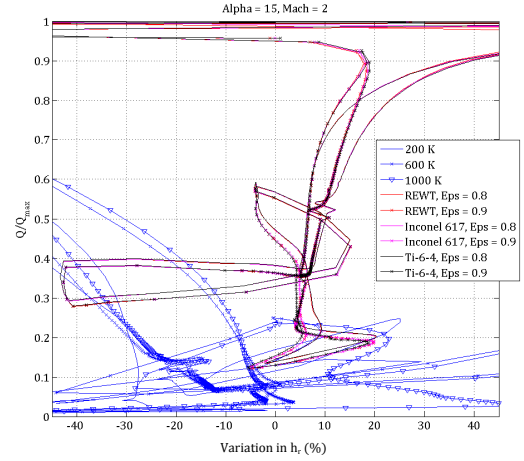


**Figure A-4** –  $Q/Q_{max}$  as a function of % variation in recovery temperature based heat transfer coefficient at Mach 2 and  $\alpha = 15^\circ$ .

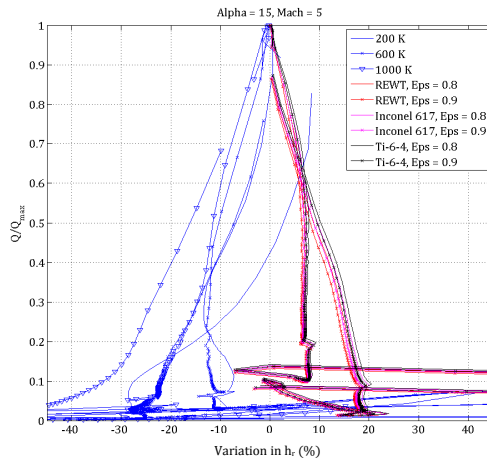


**Figure A-5** –  $Q/Q_{max}$  as a function of % variation in recovery temperature based heat transfer coefficient at Mach 5 and  $\alpha = 15^\circ$ .

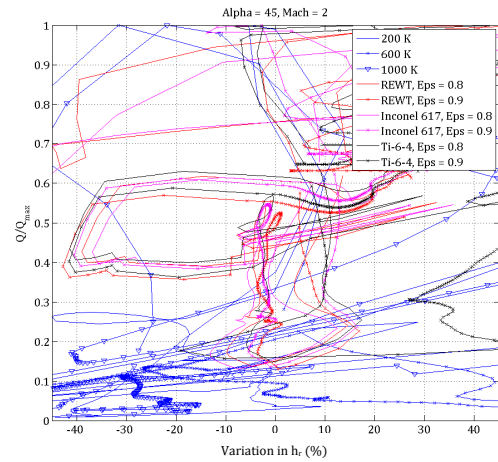


**Figure A-6** –  $Q/Q_{max}$  as a function of % variation in recovery temperature based heat transfer coefficient at Mach 2 and  $\alpha = 45^\circ$ .



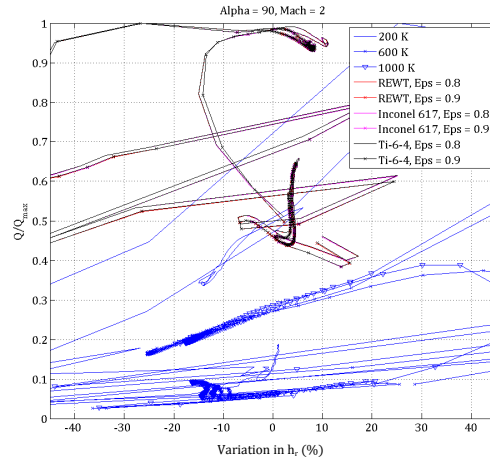


**Figure A-7** –  $Q/Q_{max}$  as a function of % variation in recovery temperature based heat transfer coefficient at Mach 2 and  $\alpha = 90^\circ$ .

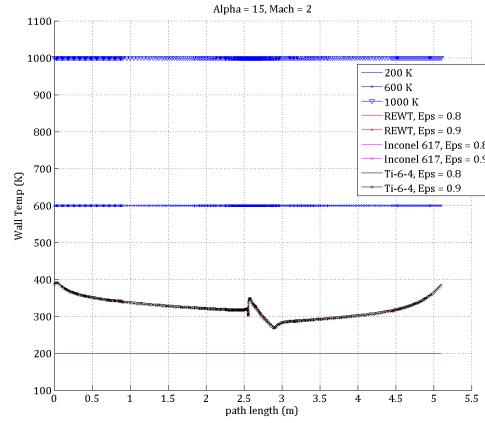


**Figure A-8** – Wall temperature as a function of path length for Mach 2 and  $\alpha = 15^\circ$ .

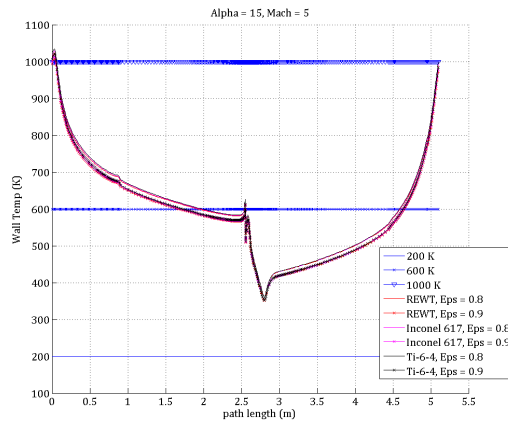


**Figure A-9** – Wall temperature as a function of path length for Mach 5 and  $\alpha = 15^\circ$ .

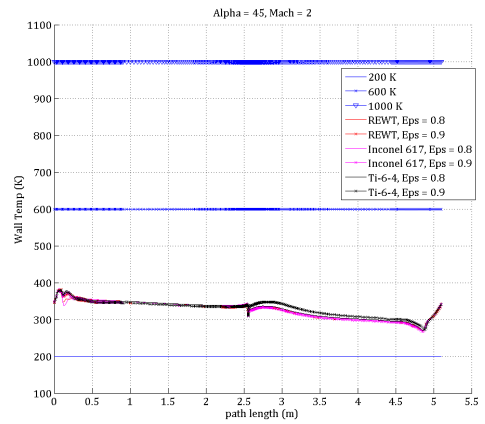


**Figure A-10** – Wall temperature as a function of path length for Mach 2 and  $\alpha = 45^\circ$ .

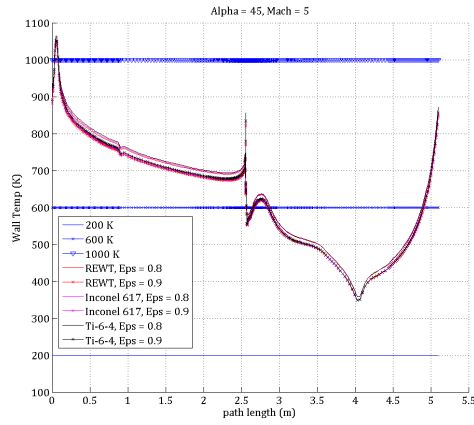


**Figure A-11** – Wall temperature as a function of path length for Mach 5 and  $\alpha = 45^\circ$ .

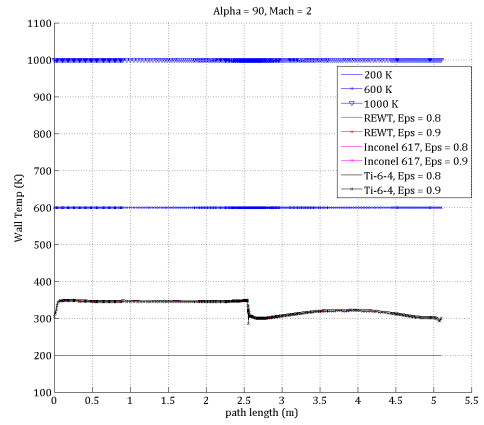


**Figure A-12**– Wall temperature as a function of path length for Mach 2 and  $\alpha = 90^\circ$ .

## APPENDIX B

### WEAK DEPENDENCE QUANTIFICATION STUDY JOB CODE AND BOUNDARY CONDITION

#### LIST

**Table B-1** – Job code for the weak dependence assumption quantification study and the corresponding boundary conditions.

BOUNDARY CONDITIONS				
Job Code	Wall	Angle of Attack	Mach Number	Emissivity
lim-1-1-1-1	200 K Isothermal	AoA = 0 deg	Mach = 2	No Emissivity, Isothermal Wall
lim-1-1-2-1	200 K Isothermal	AoA = 0 deg	Mach = 5	No Emissivity, Isothermal Wall
lim-1-2-1-1	200 K Isothermal	AoA = 15 deg	Mach = 2	No Emissivity, Isothermal Wall
lim-1-2-2-1	200 K Isothermal	AoA = 15 deg	Mach = 5	No Emissivity, Isothermal Wall
lim-1-3-1-1	200 K Isothermal	AoA = 45 deg	Mach = 2	No Emissivity, Isothermal Wall
lim-1-3-2-1	200 K Isothermal	AoA = 45 deg	Mach = 5	No Emissivity, Isothermal Wall
lim-1-4-1-1	200 K Isothermal	AoA = 90 deg	Mach = 2	No Emissivity, Isothermal Wall
lim-1-4-2-1	200 K Isothermal	AoA = 90 deg	Mach = 5	No Emissivity, Isothermal Wall
lim-2-1-1-1	600 K Isothermal	AoA = 0 deg	Mach = 2	No Emissivity, Isothermal Wall
lim-2-1-2-1	600 K Isothermal	AoA = 0 deg	Mach = 5	No Emissivity, Isothermal Wall
lim-2-2-1-1	600 K Isothermal	AoA = 15 deg	Mach = 2	No Emissivity, Isothermal Wall
lim-2-2-2-1	600 K Isothermal	AoA = 15 deg	Mach = 5	No Emissivity, Isothermal Wall
lim-2-3-1-1	600 K Isothermal	AoA = 45 deg	Mach = 2	No Emissivity, Isothermal Wall
lim-2-3-2-1	600 K Isothermal	AoA = 45 deg	Mach = 5	No Emissivity, Isothermal Wall
lim-2-4-1-1	600 K Isothermal	AoA = 90 deg	Mach = 2	No Emissivity, Isothermal Wall
lim-2-4-2-1	600 K Isothermal	AoA = 90 deg	Mach = 5	No Emissivity, Isothermal Wall
lim-3-1-1-1	1000 K Isothermal	AoA = 0 deg	Mach = 2	No Emissivity, Isothermal Wall

lim-3-1-2-1	1000 K Isothermal	AoA = 0 deg	Mach = 5	No Emissivity, Isothermal Wall
lim-3-2-1-1	1000 K Isothermal	AoA = 15 deg	Mach = 2	No Emissivity, Isothermal Wall
lim-3-2-2-1	1000 K Isothermal	AoA = 15 deg	Mach = 5	No Emissivity, Isothermal Wall
lim-3-3-1-1	1000 K Isothermal	AoA = 45 deg	Mach = 2	No Emissivity, Isothermal Wall
lim-3-3-2-1	1000 K Isothermal	AoA = 45 deg	Mach = 5	No Emissivity, Isothermal Wall
lim-3-4-1-1	1000 K Isothermal	AoA = 90 deg	Mach = 2	No Emissivity, Isothermal Wall
lim-3-4-2-1	1000 K Isothermal	AoA = 90 deg	Mach = 5	No Emissivity, Isothermal Wall
lim-4-1-1-1	REWT	AoA = 0 deg	Mach = 2	Emissivity = 0.8
lim-4-1-1-2	REWT	AoA = 0 deg	Mach = 2	Emissivity = 0.9
lim-4-1-2-1	REWT	AoA = 0 deg	Mach = 5	Emissivity = 0.8
lim-4-1-2-2	REWT	AoA = 0 deg	Mach = 5	Emissivity = 0.9
lim-4-2-1-1	REWT	AoA = 15 deg	Mach = 2	Emissivity = 0.8
lim-4-2-1-2	REWT	AoA = 15 deg	Mach = 2	Emissivity = 0.9
lim-4-2-2-1	REWT	AoA = 15 deg	Mach = 5	Emissivity = 0.8
lim-4-2-2-2	REWT	AoA = 15 deg	Mach = 5	Emissivity = 0.9
lim-4-3-1-1	REWT	AoA = 45 deg	Mach = 2	Emissivity = 0.8
lim-4-3-1-2	REWT	AoA = 45 deg	Mach = 2	Emissivity = 0.9
lim-4-3-2-1	REWT	AoA = 45 deg	Mach = 5	Emissivity = 0.8
lim-4-3-2-2	REWT	AoA = 45 deg	Mach = 5	Emissivity = 0.9
lim-4-4-1-1	REWT	AoA = 90 deg	Mach = 2	Emissivity = 0.8
lim-4-4-1-2	REWT	AoA = 90 deg	Mach = 2	Emissivity = 0.9
lim-4-4-2-1	REWT	AoA = 90 deg	Mach = 5	Emissivity = 0.8
lim-4-4-2-2	REWT	AoA = 90 deg	Mach = 5	Emissivity = 0.9
lim-5-1-1-1	Radiation Adiabatic Ti-6-4	AoA = 0 deg	Mach = 2	Emissivity = 0.8
lim-5-1-1-2	Radiation Adiabatic Ti-6-4	AoA = 0 deg	Mach = 2	Emissivity = 0.9
lim-5-1-2-1	Radiation Adiabatic Ti-6-4	AoA = 0 deg	Mach = 5	Emissivity = 0.8
lim-5-1-2-2	Radiation Adiabatic Ti-6-4	AoA = 0 deg	Mach = 5	Emissivity = 0.9
lim-5-2-1-1	Radiation Adiabatic Ti-6-4	AoA = 15 deg	Mach = 2	Emissivity = 0.8
lim-5-2-1-2	Radiation Adiabatic Ti-6-4	AoA = 15 deg	Mach = 2	Emissivity = 0.9
lim-5-2-2-1	Radiation Adiabatic Ti-6-4	AoA = 15 deg	Mach = 5	Emissivity = 0.8

lim-5-2-2-2	Radiation Adiabatic Ti-6-4	AoA = 15 deg	Mach = 5	Emissivity = 0.9
lim-5-3-1-1	Radiation Adiabatic Ti-6-4	AoA = 45 deg	Mach = 2	Emissivity = 0.8
lim-5-3-1-2	Radiation Adiabatic Ti-6-4	AoA = 45 deg	Mach = 2	Emissivity = 0.9
lim-5-3-2-1	Radiation Adiabatic Ti-6-4	AoA = 45 deg	Mach = 5	Emissivity = 0.8
lim-5-3-2-2	Radiation Adiabatic Ti-6-4	AoA = 45 deg	Mach = 5	Emissivity = 0.9
lim-5-4-1-1	Radiation Adiabatic Ti-6-4	AoA = 90 deg	Mach = 2	Emissivity = 0.8
lim-5-4-1-2	Radiation Adiabatic Ti-6-4	AoA = 90 deg	Mach = 2	Emissivity = 0.9
lim-5-4-2-1	Radiation Adiabatic Ti-6-4	AoA = 90 deg	Mach = 5	Emissivity = 0.8
lim-5-4-2-2	Radiation Adiabatic Ti-6-4	AoA = 90 deg	Mach = 5	Emissivity = 0.9
lim-6-1-1-1	Radiation Adiabatic Inconel-617	AoA = 0 deg	Mach = 2	Emissivity = 0.8
lim-6-1-1-2	Radiation Adiabatic Inconel-617	AoA = 0 deg	Mach = 2	Emissivity = 0.9
lim-6-1-2-1	Radiation Adiabatic Inconel-617	AoA = 0 deg	Mach = 5	Emissivity = 0.8
lim-6-1-2-2	Radiation Adiabatic Inconel-617	AoA = 0 deg	Mach = 5	Emissivity = 0.9
lim-6-2-1-1	Radiation Adiabatic Inconel-617	AoA = 15 deg	Mach = 2	Emissivity = 0.8
lim-6-2-1-2	Radiation Adiabatic Inconel-617	AoA = 15 deg	Mach = 2	Emissivity = 0.9
lim-6-2-2-1	Radiation Adiabatic Inconel-617	AoA = 15 deg	Mach = 5	Emissivity = 0.8
lim-6-2-2-2	Radiation Adiabatic Inconel-617	AoA = 15 deg	Mach = 5	Emissivity = 0.9
lim-6-3-1-1	Radiation Adiabatic Inconel-617	AoA = 45 deg	Mach = 2	Emissivity = 0.8
lim-6-3-1-2	Radiation Adiabatic Inconel-617	AoA = 45 deg	Mach = 2	Emissivity = 0.9
lim-6-3-2-1	Radiation Adiabatic Inconel-617	AoA = 45 deg	Mach = 5	Emissivity = 0.8
lim-6-3-2-2	Radiation Adiabatic Inconel-617	AoA = 45 deg	Mach = 5	Emissivity = 0.9
lim-6-4-1-1	Radiation Adiabatic Inconel-617	AoA = 90 deg	Mach = 2	Emissivity = 0.8
lim-6-4-1-2	Radiation Adiabatic Inconel-617	AoA = 90 deg	Mach = 2	Emissivity = 0.9
lim-6-4-2-1	Radiation Adiabatic Inconel-617	AoA = 90 deg	Mach = 5	Emissivity = 0.8
lim-6-4-2-2	Radiation Adiabatic Inconel-617	AoA = 90 deg	Mach = 5	Emissivity = 0.9

## APPENDIX C

### SUMMARY OF STEADY STATE 3-D CFD RUNS AND FLIGHT CONDITIONS

Table C-1 – Job name, mission time, integrated total surface heat flux, Mach number, dynamic pressure, and angle of attack for each CFD analysis performed in the applied problem.

<b>Job Name</b>	<b>Mission Time (sec)</b>	<b>Integral Total Surface Heat Flux (Watts)</b>	<b>Mach Number</b>	<b>Dynamic Pressure <math>\left(\frac{kg}{m \cdot s^2}\right)</math></b>
ast9500	95	448,477	2.02	666.5622
ast11507	115	1,322,735	3.00	303.7527
ast13300	133	1,680,203	4.00	92.46446
ast14800	148	969,928	5.02	28.39055
rbt0	153.45	727,450	5.61	17.98969
rbt100	154.45	692,997	5.72	16.32025
rbt150	154.95	684,755	5.77	15.53316
rbt200	155.45	672,964	5.82	14.76631
rbt250	155.95	657,104	5.88	14.03809
rbt300	156.45	738,241	5.95	13.43225
rbt350	156.95	892,313	6.03	12.82584
rbt400	157.45	1,462,405	6.10	12.19808
rbt450	157.95	1,586,430	6.17	11.58524
rbt500	158.45	985,463	6.23	10.94391
rbt600	159.45	1,153,802	6.32	9.588986
rbt700	160.45	693,953	6.34	8.180549
rbt775	161.2	551,604	6.33	7.157326
rbt875	162.2	451,393	6.30	5.944341
rbt975	163.2	369,867	6.26	4.894708
rbt1075	164.2	302,757	6.20	3.997932
rbt1175	165.2	247,187	6.14	3.239218
rbt1275	166.2	197,916	6.06	2.604986

rbt1375	167.2	160,608	5.97	2.079738
rbt1455	168	134,293	5.88	1.730871
rbt1550	168.95	111,646	5.77	1.383836
rbt1650	169.95	91,349	5.65	1.090427
rbt1750	170.95	74,741	5.51	0.855574
rbt1850	171.95	60,597	5.36	0.669147
rbt1950	172.95	49,001	5.21	0.5211
rbt2050	173.95	38,823	5.01	0.399251
rbt2150	174.95	29,988	4.77	0.301348
rbt2249	175.94	23,330	4.53	0.227264
rbt2325	176.7	19,086	4.34	0.18234
rbt2425	177.7	14,657	4.08	0.135936
rbt2525	178.7	11,276	3.82	0.100795
rbt2625	179.7	8,697	3.55	0.069149
rbt2725	180.7	6,716	3.28	0.059024
rbt2813	181.58	5,334	3.04	0.050707
rbt3525	188.7	549	1.20	0.00792
rbt3610	189.55	486	1.05	0.006006
rbt3700	190.45	429	0.91	0.004565
rbt3775	191.2	388	0.84	0.003838
rbt3850	191.95	465	0.81	0.003561
rbt3907	192.52	596	0.82	0.003665
rbt5007	203.52	1,056	0.77	0.003043
rbt6207	215.52	1,369	0.76	0.003545
rbt9407	247.52	7,179	1.39	0.02052
rbt15807	311.52	1,124,225	2.81	47.25952
rbt16707	320.52	1,319,919	2.86	228.2062
rbt19207	345.52	499,918	2.07	1029.841
rbt24407	397.52	75,540	0.70	179.0888
rbt41207	565.52	129,367	0.49	275.2841